



THE HONG KONG
POLYTECHNIC UNIVERSITY

香港理工大學

Pao Yue-kong Library

包玉剛圖書館

Copyright Undertaking

This thesis is protected by copyright, with all rights reserved.

By reading and using the thesis, the reader understands and agrees to the following terms:

1. The reader will abide by the rules and legal ordinances governing copyright regarding the use of the thesis.
2. The reader will use the thesis for the purpose of research or private study only and not for distribution or further reproduction or any other purpose.
3. The reader agrees to indemnify and hold the University harmless from and against any loss, damage, cost, liability or expenses arising from copyright infringement or unauthorized usage.

IMPORTANT

If you have reasons to believe that any materials in this thesis are deemed not suitable to be distributed in this form, or a copyright owner having difficulty with the material being included in our database, please contact lbsys@polyu.edu.hk providing details. The Library will look into your claim and consider taking remedial action upon receipt of the written requests.

**NUMERICAL SIMULATION OF AEROSOL
DYNAMICS IN MULTI-SCALE SYSTEMS**

LIU SHUYUAN

Ph.D

The Hong Kong Polytechnic University

2017



The Hong Kong Polytechnic University
Department of Mechanical Engineering

**NUMERICAL SIMULATION OF AEROSOL
DYNAMICS IN MULTI-SCALE SYSTEMS**

Liu Shuyuan

A thesis submitted in partial fulfillment of the requirements
for the Degree of Doctor of Philosophy

August 2016

Certificate of Originality

Certificate of Originality

I hereby declare that this thesis is my own work and that, to the best of my knowledge and belief, it reproduces no material previously published or written, nor material that has been accepted for the award of any other degree or diploma in any other University or Institute, except where due acknowledgement and reference have been made in the text of the thesis.

_____ (Signed)

LIU Shuyuan _____ (Name of student)

Abstract

The study of aerosol dynamics is of great importance to a variety of scientific fields including air pollution, vehicle emissions, combustion and chemical engineering science. A new stochastically weighted operator splitting Monte Carlo (SWOSMC) method is first proposed and developed in the present study in which weighted numerical particles and operator splitting technique are coupled in order to reduce statistical error and accelerate the simulation of particle-fluid systems undergoing simultaneous complex aerosol dynamic processes.

This new SWOSMC method is first validated by comparing its simulation results with the corresponding analytical solution for the selected cases. Some cases involving the evolution and formation of complex particle processes in fluid-particle systems are studied using this SWOSMC method. The obtained results are compared with those obtained by the sectional method and good agreement is obtained. Computational analysis indicates that this new SWOSMC method has high computational efficiency and accuracy in solving complex particle-fluid system problems, particularly simultaneous aerosol dynamic processes.

In order to solve multi-dimensional aerosols dynamics interacting with continuous fluid phase, this validated SWOSMC method for population balance equation (PBE) is coupled with computational fluid dynamics (CFD) under the Eulerian-Lagrangian reference frame. The formulated CFD-Monte Carlo (CFD-MC) method is used to study complex aerosol dynamics in turbulent flows. Several typical cases of aerosol dynamic processes including turbulent coagulation,

nucleation and growth are studied and compared to the population balance sectional method (PBSM) with excellent agreement. The effects of different jet Reynolds (Re_j) numbers on aerosol dynamics in turbulent flows are fully investigated for each of the studied cases in an aerosol reactor. The results demonstrate that Re_j has significant impact on a single aerosol dynamic process (e.g. coagulation) as well as the competition between simultaneous aerosol dynamic processes in turbulent flows. This newly proposed and developed CFD-Monte Carlo/probability density function (CFD-MC/PDF) method renders an efficient method for simulating complex aerosol dynamics in turbulent flows and provides a better insight into the interaction between turbulence and the full particle size distribution (PSD) of aerosol particles.

Finally, aerosol dynamics in turbulent reactive flows i.e., soot dynamics in turbulent reactive flows, is investigated and validated with corresponding experimental results available in literature. Excellent numerical results in temperature, mixture fraction and soot volume fraction as well as PSD of soot particles are obtained when compared with the experimental results, which validates the capability of this new CFD-MC/PDF method with the soot and radiation models for solving aerosol dynamics in turbulent reactive flows.

In summary, this newly proposed and developed CFD-MC/PDF method in the present study has demonstrated high capability, and computational efficiency and accuracy in the numerical simulation of complex aerosol dynamics in multi-scale systems.

List of Publications

1. **Liu S.Y.**, Chan T.L., Zhou K., 2015. A new stochastically weighted operator splitting Monte Carlo method for particle-fluid systems. *ASME-ATI-UIT 2015 Conference on Thermal Energy Systems: Production, Storage, Utilization and the Environment* (In Session: Computational Thermal-fluid Dynamics), May 17-20, Naples, Italy.
2. **Liu S.Y.**, Chan T.L., 2016. A coupled CFD-Monte Carlo method for aerosol dynamics in turbulent flows. *Aerosol Science and Technology*. In Press. (DOI: 10.1080/02786826.2016.1260087).
3. **Liu S.Y.**, Chan T.L., 2017. A stochastically weighted operator splitting Monte Carlo (SWOSMC) method for the numerical simulation of complex aerosol dynamic processes. *International Journal of Numerical Methods for Heat and Fluid Flow*. Vol. 27, pp. 263-278.

Acknowledgements

I would like to express my sincerest gratitude and respect to my Supervisor, Prof. Tat Leung Chan for his comprehensive support, encouragement, inspiring guidance, fruitful discussions, understanding and patience throughout my study at the Department of Mechanical Engineering, The Hong Kong Polytechnic University (PolyU). I appreciate his extensive knowledge and respectable attitude towards academic research as well as his kind and generous support to me. I would like also to extend my thanks to Prof. Zhou Kun (Wuhan University of Science and Technology, China) for his kind guidance and selfless help.

I am grateful to the Scientific Officer, Mr. Raymond Chan and Technical Officer, Mr. Chris Tsang for their invaluable technical support. My appreciations also go to the administrative supporting staff, Ms. Lily Tam and Ms. Michelle Lai who provided kind administrative support. I would also like to express my thanks to the financial support from the research studentship granted by The Hong Kong Polytechnic University for accomplishing this research work.

I am also grateful to Dr. Zhenlong Xiao, Dr. Jianhao Zhou, Mr. Di Wu, Mr. Keming Wu, and Mr. Yehai Li for their friendship and help during my three-year study at PolyU.

Finally, I wish to give my deep thanks to my family members for their love, support, understanding and encouragement during my study at PolyU.

Table of Contents

Abstract	i
List of Publications	iii
Acknowledgements	iv
Table of Contents	v
List of Figures	xii
List of Tables	xix
Nomenclature	xx
Greek Symbols	xxvi
Abbreviations	xxvii
Chapter 1 Introduction	1
1.1 Research Background and Scope	1
1.2 Research Motivation and Objectives	12
1.3 Outline of the Thesis	13
Chapter 2 Literature Review	15
2.1 Aerosol Dynamics in Multi-scale Systems	15
2.1.1 Atmospheric Aerosols	15
2.1.2 Multi-scale Fluid-particle Systems in Chemical Reactors	18
2.1.3 Multi-scale Flows and Particle Issues	22

Table of Contents

2.2	Experimental investigation of aerosol dynamics	25
2.2.1	Collection of Aerosol Particles	25
2.2.2	Examination and Characterization of Aerosol Particles	26
2.3	Numerical Methods for the Simulation of Aerosol Dynamics	26
2.3.1	Sectional Method	27
2.3.2	Method of Moments	28
2.3.3	Stochastic Method	29
2.4	Direct Simulation Monte Carlo Method	30
2.4.1	Overview	30
2.4.2	Particle Representation	31
2.4.3	Algorithm and Numerical Simulation Parameters	32
2.5	Operator Splitting Monte Carlo Method	37
2.5.1	Overview	37
2.5.2	Operator Splitting Schemes	39
2.5.3	Implementation of Operator Splitting	41
2.6	Weighted Monte Carlo Methods	42
2.6.1	Overview	42
2.6.2	Different Weighting Numerical particles Schemes	43
2.7	CFD-Population Balance Modelling of Aerosol Dynamics	44
2.8	Transported PDF Methods for Turbulent Reactive Flows	46
2.8.1	Overview	46
2.8.2	Eulerian PDF methods	49
2.8.3	Lagrangian PDF Methods	52
2.8.4	Improvements of the PDF Methods	55

Table of Contents

2.9 Summary of Literature Review	55
Chapter 3 Theoretical Fundamentals of the Present Study	58
3.1 Introduction	58
3.2 Population Balance Equation	58
3.2.1 Overview	58
3.2.2 The Self-preserving Behavior of PBE	60
3.2.3 The Solution of PBE	62
3.3 Monte Carlo Methods	64
3.3.1 Overview	64
3.3.2 Implementation Procedures	64
3.4 Eulerian-Lagrangian Models	65
3.4.1 Overview	65
3.4.2 Interphase Coupling	66
3.5 Transported PDF Methods for Turbulent Reactive Flows	67
3.5.1 Overview	67
3.5.2 Transport Equations for Turbulent Reactive Flows	68
3.5.3 Transported PDF Methods	68
3.6 Summary	69
Chapter 4 Zero-dimensional Monte Carlo Simulation of Aerosol Dynamics	70
4.1 Introduction	70
4.2 Numerical Methodology	71
4.2.1 General Dynamics Equation	71
4.2.2 Operator Splitting	72

Table of Contents

4.2.3	Aerosol Dynamics Kernels	72
4.2.4	Non-dimensionalization	74
4.3	Numerical Setup	76
4.3.1	Time Step Determination	76
4.3.2	Integration Details	77
4.3.3	Initial Conditions and Cases with Analytical Solutions	79
4.3.3.1	Initial Conditions	79
4.3.3.2	Constant Rate Coagulation and Linear Rate Condensation	80
4.3.3.4	Simultaneous Coagulation, Nucleation and Condensation	81
4.3.4	Calculation of Maximum Relative Error	82
4.4	Results and discussion	82
4.4.1	Initial Validation	82
4.4.2	Constant Rate Coagulation and Nucleation	85
4.4.3	Free Molecular Regime Coagulation and Constant Rate Nucleation	87
4.4.4	Simultaneous coagulation, nucleation and condensation processes	90
4.4.5	Parametric analysis of the studied cases	92
4.5	Summary	94
Chapter 5	CFD-PBM Simulation of Aerosol Dynamics in Turbulent Flows	95
5.1	Introduction	95
5.2	Numerical Methodology	96
5.2.1	Governing Equations of Aerosol Dynamics in Turbulent Flows	96
5.2.2	PDF Transport Equation Formulation	99
5.2.2.1	Discretization of the Continuous PBE	99

Table of Contents

5.2.2.2 Final PDF Transport Equation	101
5.2.3 Monte Carlo Simulation of the PDF Transport Equation	102
5.2.4 Simulation Analysis	106
5.3 Simulation Setup	107
5.4 Results and Discussion	111
5.4.1 Comparison of Coagulation in Both Laminar and Turbulent Flows	111
5.4.2 The Effect of Re_j Number on Coagulation in Turbulent Flows	114
5.4.3 The Effect of Re_j Number on Coagulation and Nucleation in Turbulent Flows	119
5.4.4 Simultaneous Coagulation, Nucleation and Growth Processes in Turbulent Flows	126
5.4.5 Computational Accuracy and Efficiency	131
5.4.6 Numerical Stability Analysis	133
5.5 Summary	134
Chapter 6 Simulation of Aerosol Dynamics in Turbulent Reactive flows..	136
6.1 Introduction	136
6.2 Numerical Methodology	138
6.2.1 The CFD Code	138
6.2.2 The Lagrangian PDF Method	139
6.2.3 Particle Tracking Algorithm	141
6.2.4 Estimation of Mean Field	142
6.2.5 Soot Model	142
6.2.6 Radiation Model	143
6.3 Numerical Simulation Setup	144

Table of Contents

6.4 Results and Discussion	147
6.4.1 Axial and Radial Jet Temperature Variations of the Studied Combustor	147
6.4.2 Axial and Radial Jet Mixture Fraction Variations of the Studied Combustor	150
6.4.3 Axial and Radial Jet Soot Volume Fraction Variations of the Studied Combustor	153
6.4.4 Soot Size Distribution	156
6.4.5 Relative Error Analysis	158
6.5 Summary	159
Chapter 7 Conclusions and Recommendations for Future Work	161
7.1 Review of the Present Research	161
7.2 Main Conclusions of the Thesis	163
7.2.1 Conclusions of the Zero-Dimensional Monte Carlo Simulation of Aerosol Dynamics	163
7.2.2 Conclusions of the CFD-PBM Simulation of Aerosol Dynamics in Turbulent Flows	164
7.2.3 Conclusions of Simulation of Aerosol Dynamics in Turbulent Reactive Flows	165
7.3 Recommendations for Future Work	166
7.3.1 Limitations of the Current Research	166
7.3.2 Recommendations for Future Work	167
Appendices	169
A.1 Coagulation Process	169
A.2 Nucleation Process	170
A.3 Surface Reactions in Soot Formation	170

Table of Contents

A.4 Soot Formation Models	171
A.4.1 The One-Step Soot Formation Model	171
A.4.2 The Two-Step Soot Formation Model	172
A.4.2.1 Net Rate of Soot Generation	172
A.4.2.2 Net Rate of Nuclei Generation	173
A.4.3 The Moss-Brookes Model	174
A.4.4 The Moss-Brookes-Hall Model	175
References	177

List of Figures

Figure 1.1	Modelling and simulation of multi-scale aerosol dynamics (Kulmala et al., 2009).	2
Figure 1.2	Schematic diagram of the model to predict aerosol formation in lower troposphere (MALTE) model (Boy et al., 2006).	3
Figure 1.3	Schematic diagram of the aerosol dynamics, gas and particle phase chemistry (ADCHEM) model (Roldin et al., 2011).	4
Figure 1.4	A typical flow chart of Monte Carlo algorithm (Efendiev, 2004).	6
Figure 1.5	A typical flow chart of direct simulation Monte Carlo (DSMC) method (left) and Parallel DSMC method (right) (Roohi and Darbandi, 2012).	8
Figure 2.1	Various mechanisms with cloud effects of atmospheric aerosols (Valsaraj and Kommalapati, 2009).	17
Figure 2.2	Scatterplot of daily average PM _{2.5} concentrations from continental U.S. monitoring stations for the period of June 15–July 16, 1999 versus comparable CMAQ model estimates (Byun and Schere, 2006).	17
Figure 2.3	Calculated distribution of a passive tracer released from a surface point source using a fifth-order scheme in the horizontal advection (Robertson et al., 1999).	18
Figure 2.4	Velocity vector profiles inside a fluidized bed reactor obtained with computational fluid dynamics-discrete element method (CFD-DEM) method (Zhuang et al., 2014).	19
Figure 2.5	Main reaction parameter distribution profiles in the methanol to olefins (MTO) fluidized bed reactor (FBR) at $t = 0.052$ s: (a) gas-phase temperature; (b) particle temperature; (c) coke content; (d) ethane mole concentration; (e) propene mole concentration; and (f) butene mole concentration; space (velocity = 2.8 m/s, inlet feed temperature = 723 K, feed ratio of water to methanol = 0, adopted from Zhuang et al.(2014)).	20

List of Figures

Figure 2.6	Parallel Lattice Boltzmann simulation results for flow within a fixed bed packed with the binary mixture of two types of spheres: (a) velocity vector; and (b) velocity contour and vector on the mid-plane (Rong et al., 2014).	21
Figure 2.7	Parallel Lattice Boltzmann simulation results for flow within a fixed bed packed with the binary mixture of two types of spheres: spatial distribution of the drag forces on individual particle across the mid-plane (Rong et al., 2014).	21
Figure 2.8	(a) Computational domain using a purely atomistic description; (b) Hybrid atomistic/continuum computational domain; (c) Velocity field for the reference solution averaged over 4 ns; and (d) Velocity field of the hybrid solution after 50 iterations (Koumoutsakos, 2005).	22
Figure 2.9	The velocity profiles of flowing platelets in blood plasma with a multi-scale method of dissipative particle dynamics and coarse grained molecular dynamics(Zhang et al., 2014).	23
Figure 2.10	A schematic diagram of nano particles synthesis (Balgis et al., 2014).	24
Figure 2.11	A schematic diagram of gas diffusion in nano structures (Dreyer et al., 2014).	24
Figure 2.12	A schematic diagram of an online sampling system (Zhao et al., 2003).	25
Figure 2.13	Comparison between sectional and analytic methods: normalized number and volume concentrations under constant coagulation and linear condensation (Mitrakos et al., 2007).	27
Figure 2.14	The second order moment and the relative error for various methods in the free molecular regime (Yu et al., 2008).	28
Figure 2.15	Regimes of validity of molecular dynamics, direct simulation Monte Carlo, and Navier-Stokes, as a function of the characteristic length scale and mean molecular spacing of a system (Oran et al., 1998).	29
Figure 2.16	Operator splitting schemes: (a) first-order Lie scheme; and (b) second-order Strang scheme (Zhou et al., 2014).	40

List of Figures

Figure 2.17	Flowchart of the operator splitting steps. (X_d and X_s have the same meaning with those in Equation (2.9) (Zhou et al., 2014).	41
Figure 2.18	Flow variables for the l th grid cell and four neighboring cells in Eulerian PDF methods (Fox, 2003).	50
Figure 2.19	Flow diagram of Lagrangian PDF methods (Fox, 2003).	54
Figure 3.1	Computations of average population behavior via Monte Carlo simulation (left) and PBE (right) (Ramkrishna, 2000).	63
Figure 3.2	Eulerian-Eulerian and Eulerian-Lagrangian multi-phase models under different representations of the discrete phase (Subramaniam, 2013).	65
Figure 4.1	Zeroth order moment, M_0 under coagulation and condensation processes for SWOSMC (Liu and Chan, 2017) versus the analytical solution (Ramabhadran et al., 1976) where N is the number of numerical particles used in each simulation run.	83
Figure 4.2	First order moment, M_1 under coagulation and condensation processes for SWOSMC (Liu and Chan, 2017) versus the analytical solution (Ramabhadran et al., 1976) where N is the number of numerical particles used in each simulation run.	84
Figure 4.3	Particle number density under free molecular regime coagulation for SWOSMC (Liu and Chan, 2017) versus the sectional method (Prakash et al., 2003) where the number of numerical particles, N used in each simulation run is 1000.	85
Figure 4.4	Relative particle number density, N/N_0 under constant rate coagulation and nucleation processes for SWOSMC (Liu and Chan, 2017) versus the analytical solution (Maisels et al., 2004) where N is the number of numerical particles used in each simulation run.	86
Figure 4.5	Relative particle volume concentration, V/V_0 under constant rate coagulation and nucleation processes for SWOSMC (Liu and Chan, 2017) versus the analytical solution (Maisels et al., 2004) where N is the number of numerical particles used in each simulation run.	87

List of Figures

Figure 4.6	Particle number density under free molecular regime coagulation and constant rate nucleation for SWOSMC (Liu and Chan, 2017) versus the sectional method (Prakash et al., 2003) where N is the number of numerical particles used in each simulation run.	88
Figure 4.7	Average diameter of the numerical particles, d_{ave} under free molecular regime coagulation and constant rate nucleation via SWOSMC (Liu and Chan, 2017) versus the sectional method (Prakash et al., 2003) where N is the number of numerical particles used in each simulation run.	89
Figure 4.8	Second order moment, M_2 of the particles under free molecular regime coagulation and constant rate nucleation processes for SWOSMC (Liu and Chan, 2017) versus the sectional method (Prakash et al., 2003) where N is the number of numerical particles used in each simulation run.	90
Figure 4.9	Particle volume concentration, V/V_0 under simultaneous aerosol dynamic processes for SWOSMC (Liu and Chan, 2017) versus the analytical solution (Maisels et al., 2004) where the number of numerical particles, N used in each simulation run is 4000.	91
Figure 4.10	Particle number concentration, N/N_0 under simultaneous aerosol dynamic processes for SWOSMC (Liu and Chan, 2017) versus the analytical solution (Maisels et al., 2004) where the number of numerical particles, N used in each simulation run is 4000.	92
Figure 5.1	Flow chart of the coupled CFD-Monte Carlo/PDF method (Liu and Chan, 2016).	105
Figure 5.2	Three-dimensional schematic configuration of a cylindrical aerosol reactor (Two-dimensional axisymmetric grid is generated in the rectangular domain ABCD, not in scale) (Liu and Chan, 2016).	109
Figure 5.3	Two-dimensional axisymmetric unstructured computational grid of a cylindrical aerosol reactor (Liu and Chan, 2016).	110
Figure 5.4	Initial PSD of particles before entering the aerosol reactor (Liu and Chan, 2016).	112
Figure 5.5	PSD in laminar and turbulent coagulation (Liu and Chan, 2016).	112

List of Figures

Figure 5.6	Particle number density (m^{-3}) contour in laminar and turbulent coagulation (Liu and Chan, 2016).	113
Figure 5.7	PSD in turbulent coagulation: Case A, $Re_j=3200$; Case B, $Re_j=4800$; Case C, $Re_j=6400$; Case D, $Re_j=12800$ (The PBSM results are obtained based on the method proposed by Hounslow (1988)) (Liu and Chan, 2016).	114
Figure 5.8	Average diameter of particles in turbulent coagulation (Liu and Chan, 2016).	115
Figure 5.9	Turbulent kinetic energy (m^2/s^2) contour in turbulent coagulation (Liu and Chan, 2016).	117
Figure 5.10	Particle number density (m^{-3}) contour in turbulent coagulation (Liu and Chan, 2016).	118
Figure 5.11	Normalized particle number density of turbulent coagulation (Liu and Chan, 2016).	119
Figure 5.12	PSD of simultaneous coagulation and nucleation in turbulent flows: Case A, $Re_j=3200$; Case B, $Re_j=4800$; Case C, $Re_j=6400$; Case D, $Re_j=12800$ (The PBSM results are obtained based on the method proposed by Hounslow (1988)) (Liu and Chan, 2016).	120
Figure 5.13	Average diameter of particles for coagulation and nucleation in turbulent flows (Liu and Chan, 2016).	122
Figure 5.14	Turbulent kinetic energy (m^2/s^2) contour for simultaneous coagulation and nucleation in turbulent flows (Liu and Chan, 2016).	123
Figure 5.15	Particle number density (m^{-3}) contour for simultaneous coagulation and nucleation in turbulent flows (Liu and Chan, 2016).	124
Figure 5.16	Normalized particle number density for simultaneous coagulation and nucleation in turbulent flows (Liu and Chan, 2016).	125
Figure 5.17	PSD for simultaneous coagulation, nucleation and growth in turbulent flows: Case A, $Re_j=3200$; Case B, $Re_j=4800$; Case C, $Re_j=6400$; Case D, $Re_j=12800$ (The PBSM results are obtained based on the method proposed by Hounslow (1988)) (Liu and Chan, 2016).	127

List of Figures

Figure 5.18	Average diameter of particles for simultaneous coagulation, nucleation and growth in turbulent flows (Liu and Chan, 2016).	128
Figure 5.19	Particle number density (m^{-3}) contour for simultaneous coagulation, nucleation and growth in turbulent flows (Liu and Chan, 2016).	129
Figure 5.20	Normalized particle number density for simultaneous coagulation, nucleation and growth in turbulent flows (Liu and Chan, 2016).	130
Figure 6.1	Jet burner configuration of the combustor (Brookes and Moss, 1999).	145
Figure 6.2	The computational grid used in the numerical simulation of an axisymmetric combustor.	146
Figure 6.3	Axial jet temperature variation at the centerline of the studied combustor for $Re_j=5000$ (The experimental results are obtained from Brookes and Moss (1999)).	148
Figure 6.4	Radial jet temperature variation at the axial distance of 250 mm for the studied combustor at $Re_j=5000$ (The experimental results are obtained from Brookes and Moss (1999)).	149
Figure 6.5	Radial jet temperature variation at the axial distance of 350 mm for the studied combustor at $Re_j=5000$ (The experimental results are obtained from Brookes and Moss (1999)).	150
Figure 6.6	Axial jet mixture fraction variation at the centerline of the studied combustor for $Re_j=5000$ (The experimental results are obtained from Brookes and Moss (1999)).	151
Figure 6.7	Radial jet mixture fraction variation at the axial distance of 250 mm for the studied combustor at $Re_j=5000$ (The experimental results are obtained from Brookes and Moss (1999)).	152
Figure 6.8	Radial jet mixture fraction variation at the axial distance of 350 mm for the studied combustor at $Re_j=5000$ (The experimental results are obtained from Brookes and Moss (1999)).	153

List of Figures

Figure 6.9	Axial jet soot volume fraction variation at the centerline of the studied combustor for $Re_j= 5000$ (The experimental results are obtained from Brookes and Moss (1999)).	154
Figure 6.10	Radial jet soot volume fraction variation at the axial distance of 350 mm for the studied combustor at $Re_j= 5000$ (The experimental results are obtained from Brookes and Moss (1999)).	155
Figure 6.11	Radial jet soot volume fraction variation at the axial distance of 425 mm for the studied combustor at $Re_j= 5000$ (The experimental results are obtained from Brookes and Moss (1999)).	156
Figure 6.12	PSD of jet soot particles at the axial distances of 138 mm and 308 mm (The benchmark results are from Akridis and Rigopoulos (2015)).	157

List of Tables

Table 2.1	Typical physical properties of atmospheric aerosols (Valsaraj and Kommalapati, 2009).	16
Table 2.2	Mass concentrations and diameters of atmospheric aerosols (Valsaraj and Kommalapati, 2009).	16
Table 4.1	A comparison between the developed SWOSMC method and analytical solutions.	71
Table 4.2	Summary of the studied cases (Liu and Chan, 2017).	80
Table 4.3	Analysis of main simulation parameters (Liu and Chan, 2017).	93
Table 5.1	Simulation parameters for aerosol dynamics in turbulent flows (Liu and Chan, 2016).	110
Table 5.2	Maximum relative error and normalized convergence time for different studied cases (Liu and Chan, 2016).	132
Table 5.3	Typical grid cell independence analysis.	133
Table 5.4	Typical analysis of the number of simulation particles per grid cell.	134
Table 6.1	Model constants for the k - ϵ turbulence model.	139
Table 6.2	Jet burner parameters and conditions for the studied combustor.	145
Table 6.3	Relative error analysis between the present numerical and experimental results (Brookes and Moss, 1999).	159

Nomenclature

a	subscript of ordering
a_0^*	pre-exponential rate constant
a_p	Planck mean absorption coefficient, s^2/kg
A	unspecified operator
A_s	area of soot particle, m^2
A_{soot}	constant in the Magnussen model
b^*	normalized radical nuclei concentration, $particle \times 10^{-15}/kg$
B	dimensionless parameter
B_n	nucleation kernel, m^3/s
c	the constant factor used to adjust time step
c_{fuel}	fuel concentration, kg/m^3
c_{nuc}	radical nuclei concentration, $\#/m^3$
c^*_{nuc}	normalized nuclei concentration
C	dimensionless model constant
C_I	dimensionless nucleation constant related to diffusion and temperature
C_{min}	minimum number of carbon atoms for the incipient soot
c_p	specific heat capacity, $J/(kg \cdot K)$
d_{ave}	average diameter of particles, m
d_p	particle diameter, m
D_p	diffusion coefficients of particles, m^2/s

Nomenclature

E	dimensionless parameter
E_a	activation energy, kJ/mol
f	unspecified function
$(f-g)_{\text{soot}}$	linear branching-termination coefficient, 1/s
f_v	volume fraction of soot particles
$f_{U,\psi}$	joint composition and velocity PDF
f_U	joint velocity PDF
f_ψ	joint composition PDF
F	fine-grained density function
g_0	linear termination on soot particles, $\text{m}^3/(\text{particle}\cdot\text{s})$.
G	particle growth kernel, m/s
G_0	the reduction rate of the smallest size particles by coagulation, #/s
G_{O_2}	particle oxidation rate of oxygen (O_2), $\#/(\text{m}^2\cdot\text{s})$
G_{OH}	particle oxidation rate of hydroxide (OH), $\#/(\text{m}^2\cdot\text{s})$
G_{SG}	particle growth rate, m/s
G_t	generation rate of turbulent kinetic energy, m^2/s^3
H	source of energy, J
h	small time interval, s
i	subscript of ordering
I	particle condensation kernel, $1/(\text{m}^3\cdot\text{s})$
j	subscript of ordering
k	turbulent kinetic energy, m^2/s^2

Nomenclature

k_B	Boltzmann constant, J/K
k_e	heat conductivity, m^2/s
k_n	reaction constant of nucleation, $\#/\text{(m}^3\cdot\text{s)}$
k_s	the reaction rate per unit area, $\#/\text{(m}^2\cdot\text{s)}$
k_{HW}	reaction constant of growth, $\#/\text{(m}\cdot\text{s)}$
k_a, k_b	reaction constant of oxidation, $\#/\text{(m}^2\cdot\text{s)}$
K	coagulation kernel
Kn	Knudsen number
l	model exponent constant
L_j	internal coordinate in the physical and scalar space
m_p	mass of the particle, p , kg
M	a vector space
M_j	rate of certain aerosol dynamic process, j
M_p	mass of an incipient soot particle, kg
n	number density of aerosol particles, $\#/\text{m}^3$
N	particle number concentration, $\#/\text{m}^3$
N_A	Avogadro constant, 1/mol
N_{CFL}	local CFL number in the computational domain
N_{g0}	the number density of newly generated smallest size particles
N_l	local concentration of particles, $\#/\text{m}^3$
N_n	normalized particle number density
N_{norm}	reference number density of soot particles, $\text{particle}\times 10^{-15}/\text{m}^3$

Nomenclature

N_0	initial particle number concentration, $\#/m^3$
N_∞	total number of particles in the system
NU_0	nucleation rate, $\#/(m^3 \cdot s)$
p	particle phase
P	pressure, $kg/(m \cdot s^2)$
p_{fuel}	fuel partial pressure, Pa
q	mass density of aerosol particles, kg/m^3
\tilde{q}	relative mass density of aerosol particles, kg/kg
Q	total mass of aerosol particles, kg
Q_c	physical quantity in a cell, c
Q_p	physical quantity carried by particle, p
Q_{rad}	the source term due to radiation
\dot{Q}_{laminar}	the volumetric flow rate of laminar flow
$\dot{Q}_{\text{turbulent}}$	the volumetric flow rate of turbulent flow
r	equivalence ratio exponent
R	universal gas constant, $J/(mol \cdot K)$
R_{nuc}^*	normalized net rate of nuclei generation, $\text{particle} \times 10^{-15}/(m^3 \cdot s)$
R_0	reduction rate that creates the smallest size particles, $\#/s$
R_{soot}	net rate of soot generation, $kg/(m^3 \cdot s)$
$R_{\text{soot,form}}$	soot formation rate, $kg/(m^3 \cdot s)$
$R_{\text{soot,combst}}$	soot combustion rate, $kg/(m^3 \cdot s)$

Nomenclature

Re_j	Reynolds number of the jet based on the nozzle diameter
s	molecular ratio of fuel to oxidizer
S_0	the surface area of the smallest size particles, m^2
S_a	the source term due to chemical reaction
t	time, s
rms	root mean square
T	endpoint of a time interval, s
T_α	activation temperature for nucleation reaction, K
T_γ	activation temperature for surface growth reaction, K
T_ω	activation temperature for oxidation reaction, K
T_{temp}	temperature, K
u	particle volume, m^3
\vec{u}	velocity of carrier fluid phase, m/s
v	particle volume, m^3
v_{soot}, v_{fuel}	mass stoichiometries for soot and fuel combustion, respectively
\bar{v}	average particle volume, m^3
\vec{V}	velocity space in PDF
V	total volume of the aerosol system in simulation, m^3
V_0	initial volume of the aerosol system in simulation, m^3
V_s	volume of a subsystem of aerosol particles, m^3
w	particle mass weight, kg/kg

Nomenclature

W	Wiener process
W_d	operator of deterministic process
W_{H_2}	molecular weight of hydrogen, g/mol
$W_{C_2H_2}$	molecular weight of acetylene, g/mol
$W_{C_6H_5}$	molecular weight of benzene radical, g/mol
$W_{C_6H_6}$	molecular weight of benzene, g/mol
W_P	particle weight
W_s	operator of stochastic process
X	the position of notional particles
X_d	deterministic process
X_{prec}	mole fraction of soot precursor, mol/mol
X_s	stochastic process
X_{sgs}	the mole fraction of the participating surface growth species, mol/mol
y	size of aerosol particles, m^3
Y	mass fraction of aerosol particles, kg/kg
Y_O, Y_F	molecular fraction of oxidizer and fuel, respectively.
Y_{ox}, Y_{fuel}	mass fractions of oxidiser and fuel, respectively, kg/kg
Y_{soot}	soot mass fraction, kg/kg
Z	mixture fraction in the jet flame

Greek Symbols

α	empirical constant
β	coagulation kernel, m^3/s
Γ	turbulent diffusivity, m^2/s
Δm	mass change during a single reaction event, kg
δ	Kronecker delta function
ε	turbulent dissipation rate, m^2/s^3
ε_{\max}	maximum relative error
η_{coll}	collision efficiency
η_v	dimensionless particle volume, m^3/m^3
η_d	dimensionless particle diameter
μ	molecular viscosity, $\text{kg}/(\text{m}\cdot\text{s})$
μ_t	turbulent viscosity
ν_k	kinematic viscosity, m^2/s
ρ	mass density, kg/m^3
$\sigma_k, \sigma_\varepsilon$	turbulent Prandtl number
σ_{nuc}	turbulent Prandtl number for nuclei transport
σ_s	the Stefan-Boltzmann constant, $\text{kg}/(\text{s}^3\cdot\text{K}^4)$
σ_{soot}	turbulent Prandtl number for soot transport
τ	dimensionless time

Nomenclature

ϕ	total volume of particles in the system
ϕ_α	unspecified reacting scalar
ϕ_{combst}	equivalence ratio for combustion process
Φ	micro-mixing term
ψ	composition space in PDF
ψ_v	dimensionless function of particle volume
ψ_d	dimensionless function of particle diameter
ω	weight of numerical particles

Abbreviations

ADCHEM	aerosol dynamics, gas and particle phase chemistry
CFD	computational fluid dynamics
CFL	Courant–Friedrichs–Lewy condition
CMAQ	community multi-scale air quality modeling systems
3D-CTM	three-dimensional chemical transport model
DEM	discrete element method
DGM	dusty gas model
DSMC	direct simulation Monte Carlo
DPD	dissipative particle dynamics
EMST	Euclidean minimum spanning tree
FBR	fluidized bed reactor
GCM	multi-scale global aerosol-climate model

Nomenclature

GDE	general dynamics equation
GHS	generalized variable hard sphere model
HS	hard sphere model
IC	internal combustor
LBM	Lattice Boltzmann method
LMC-PDF	Lagrangian Monte Carlo-probability density function
LPDA	linear process deferment algorithm
MALTE	model to predict aerosol formation in lower troposphere
MATCH	multi-scale atmospheric transport and chemistry model
MC	Monte Carlo method
MCMC	Markov chain Monte Carlo method
MD	molecular dynamics
MFA	mass flow algorithm
MP-PIC	multi-phase particle in cell
MTO	methanol to olefins
ODE	ordinary differential equations
OSMC	operator splitting Monte Carlo method
PBE	population balance equation
PDE	partial differential equation
PBM	population balance method
PBSM	population balance sectional method
PDF	probability density function
PSD	particle size distribution

Nomenclature

PSI-Cell	particle source in cell
DQMOM	direct quadrature method of moments
RANS	Reynolds averaged Navier-Stokes equation
SDE	stochastic differential equation
SEF	stochastic Eulerian field method
SEM	scanning electron microscopy
SWOSMC	stochastically weighted operator splitting Monte Carlo method
SWPM	stochastically weighted particle method
TCI	turbulence chemistry interaction
TRI	turbulence radiation interaction
TEM	transmission electron microscopy
TEMOM	Taylor-series expansion method of moments

Chapter 1 Introduction

1.1 Research Background and Scope

The study of aerosol dynamics is of great importance to a variety of scientific fields including air pollution, vehicle emissions, combustion and chemical engineering science. It is essential to improve the numerical simulation on efficient aerosol dynamics processes in order to have a deeper understanding of the behavior of complex multi-scale aerosol systems. Such numerical simulation makes it possible to reconcile the theoretical description of the physical principles of aerosol dynamic systems with the experimental results of these systems. There are various physical processes involved in aerosol dynamics including coagulation, nucleation, condensation/surface growth processes etc. (Zhang et al., 1999). A lot of mathematical models as well as algorithms have been developed to simulate these complex and simultaneous aerosol dynamic processes (Efendiev, 2004; Chan et al., 2009; Yu et al., 2009; Chan et al., 2010; Zhou and Chan, 2011; Geng et al., 2013, Zhou and Chan, 2014; Fede et al., 2015; Liu and Chan, 2016 and 2017). Thus, it is of significance to identify the key aerosol dynamic processes in multi-scale systems in order to reduce the difficulty in obtaining closures for aerosol dynamic models.

Most current research on aerosol dynamics focuses on monodispersed homogeneous particle system. However, it is well known that phase segregation will take place within the aerosol system under proper conditions. So it is essentially required to extend the existing aerosol dynamics modelling to multi-component and heterogeneous case in order to achieve the desired accuracy of modelling

(Efendiev, 2004). A large number of studies concerning complex aerosol dynamics and applications have been reported (Efendiev, 2002; Efendiev, 2004; Fu et al., 2012; Gac and Gradoń, 2013; Trump et al., 2015; Feng et al., 2016). However, novel numerical methods are still much needed due to the multi-scale nature of complex aerosol dynamics, some as shown in Figure 1.1 (Kulmala et al., 2009).

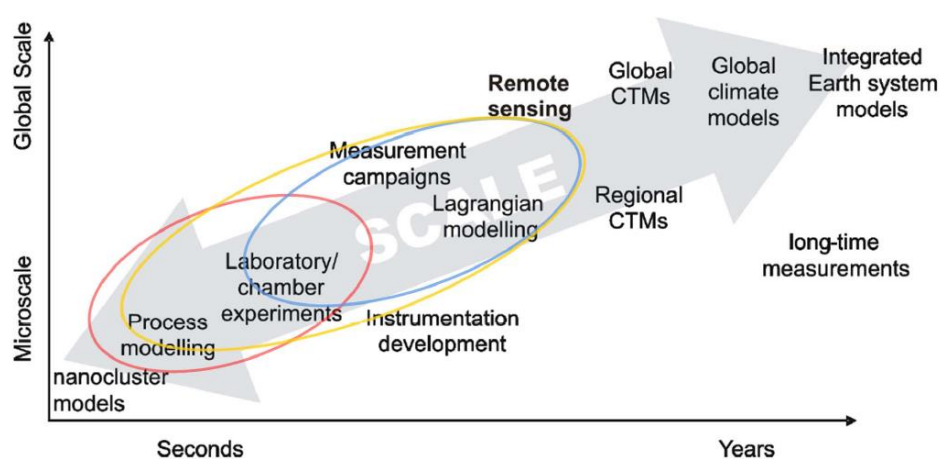


Figure 1.1 Modelling and simulation of multi-scale aerosol dynamics (Kulmala et al., 2009).

On the other hand, it is also necessary to include particle chemistry as well as gas-phase chemistry module in the model of aerosol system in order to simulate aerosol dynamics more accurately. A detailed aerosol dynamics model named University of Helsinki multicomponent aerosol model (UHMA) coupled with a detailed gas-phase chemistry module as well as a meteorological module was proposed by Boy et al., (2006). This UHMA model to predict new aerosol formation in the lower troposphere (MALTE) (Boy et al., 2006) is primarily designed to model new particle formation in the lower troposphere as shown in Figure 1.2.

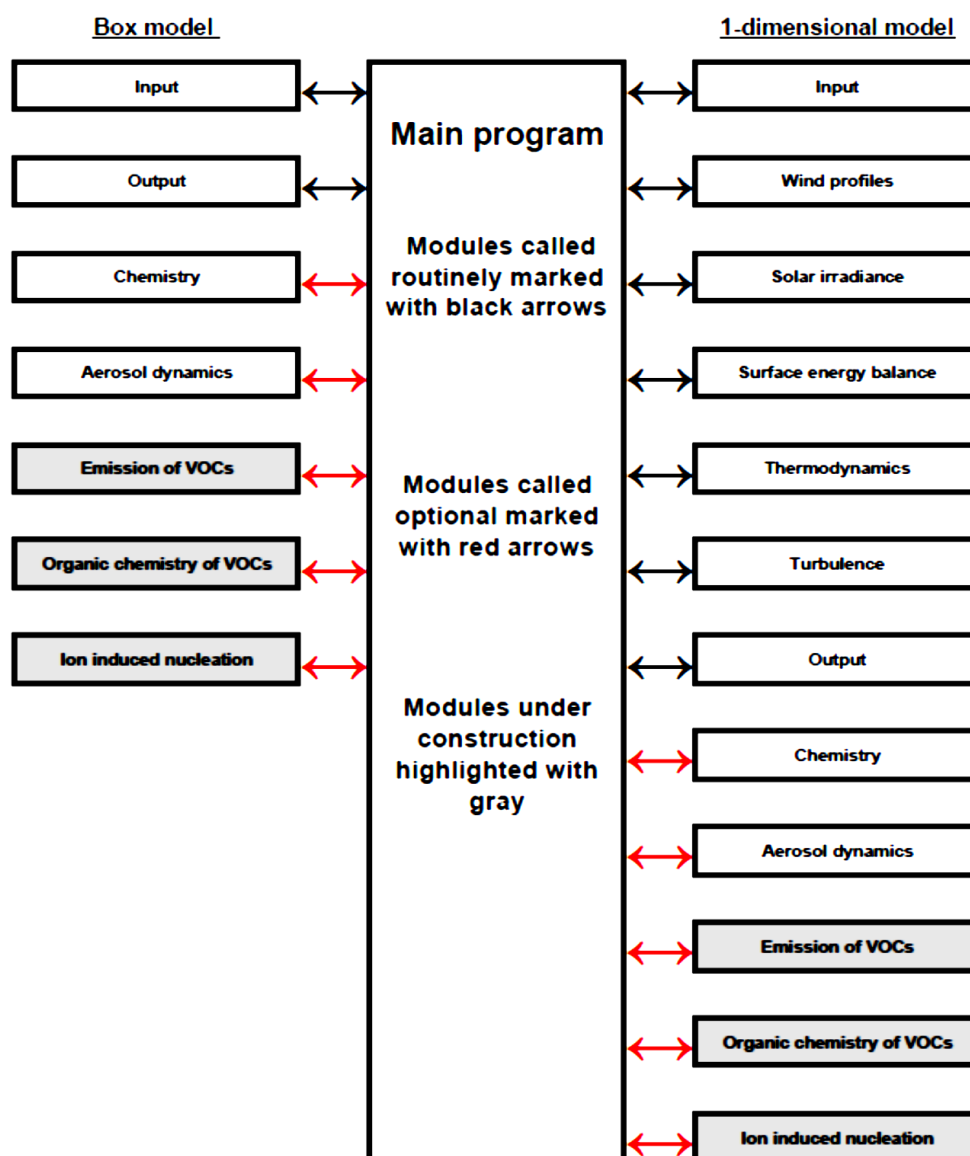


Figure 1.2 Schematic diagram of the model to predict aerosol formation in lower troposphere (MALTE) model (Boy et al., 2011).

A more detailed and comprehensive model including aerosol dynamics, gas and particle phase CHEMistry and radiative transfer (ADCHEM) (Roldin et al., 2011) as shown in Figure 1.3 is then proposed based on the developed MALTE model. The aim of the ADCHEM model was to develop a model suitable for the investigation of multi-scale complex aerosol dynamics coupled with gas and particle chemistry. The ADCHEM model was used to identify the most important

aerosol dynamic process in order to obtain accurate representation of aerosol dynamics coupled with detailed chemistry (Roldin et al., 2011). However, the complexity of the ADCHEM model may affect its wide applicability. Nevertheless, these results are useful when developing more simplified aerosol dynamics, gas and particle phase chemistry modules or parameterizations for global scale models (Roldin et al., 2011). Given the increased complexity caused by including particle chemistry as well as gas phase chemistry, the optimization and improvement of current numerical techniques are greatly needed.

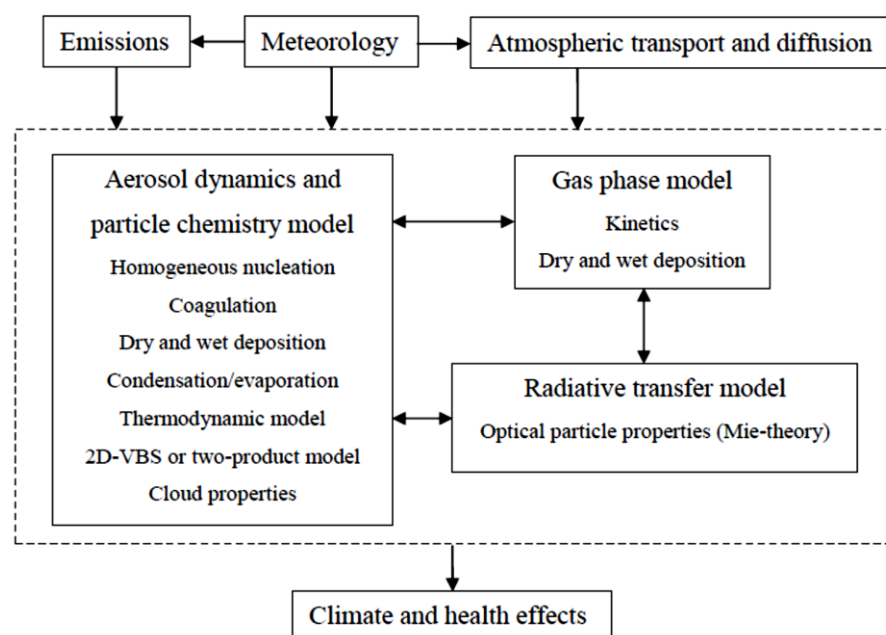


Figure 1.3 Schematic diagram of the aerosol dynamics, gas and particle phase chemistry (ADCHEM) model (Roldin et al., 2011).

The evolution of aerosol system is governed by the PBE (also called general dynamics Equation, GDE) i.e. Equation (1-1), which could include all the typical aerosol dynamic processes accounting for the birth, growth and death of particles (Wei and Kruijs, 2013).

$$\frac{\partial n(v,t)}{\partial t} = 1/2 \int_0^v \beta(v-u,u)n(u,t)n(v-u,t)du - n(v,t) \int_0^\infty \beta(v,u)n(u,t)du \quad (1-1)$$

where $n(v,t)$ is the particle size distribution (PSD) at time t and $\beta(v,u)$ is the coagulation rate for two particles with the volumes u and v , respectively. The first term on the right-hand side of Equation (1-1) represents the formation of particles with volume v due to the coagulation events between particles of volume u and particles of volume $(v-u)$; the factor $1/2$ is introduced because the collisions are counted twice for a single collision event. The second term on the right-hand side of Equation (1-1) represents the loss of particles with volume v because of collisions with particles of other sizes.

There are different numerical methods to solve the Equation (1-1), including sectional methods (Jeong and Choi, 2001; Mitrakos et al., 2007; Agarwal and Girshick, 2012), methods of moments (Lin and Chen, 2013; Yu et al., 2008; Park et al., 2013; Chen et al., 2014; Yu and Chan, 2015; Pollack et al., 2016), and Monte Carlo methods (Zhao et al., 2009; Zhao and Zheng, 2012; Wei, 2013; Zhou et al., 2014; Liu et al., 2015; Liu and Chan, 2016). The computational time of sectional methods is moderate, but the algorithms for the sectional representations could be quite complicated (Wei and Kruis, 2013). Methods of moments have relatively high computational efficiency, but require input of the initial PSD, which is variable during the numerical simulation, particularly when another aerosol dynamic process like nucleation takes place (Wei and Kruis, 2013). The methods of moment perform best only when the size distribution is lognormal. Besides these two deterministic methods, the Monte Carlo method with a stochastic nature is considered feasible to deal with the multi-scale

nature of complex aerosol dynamics (Kruis et al., 2000; Hao et al., 2013). Figure 1.4 shows a typical flow chart of Monte Carlo algorithm.

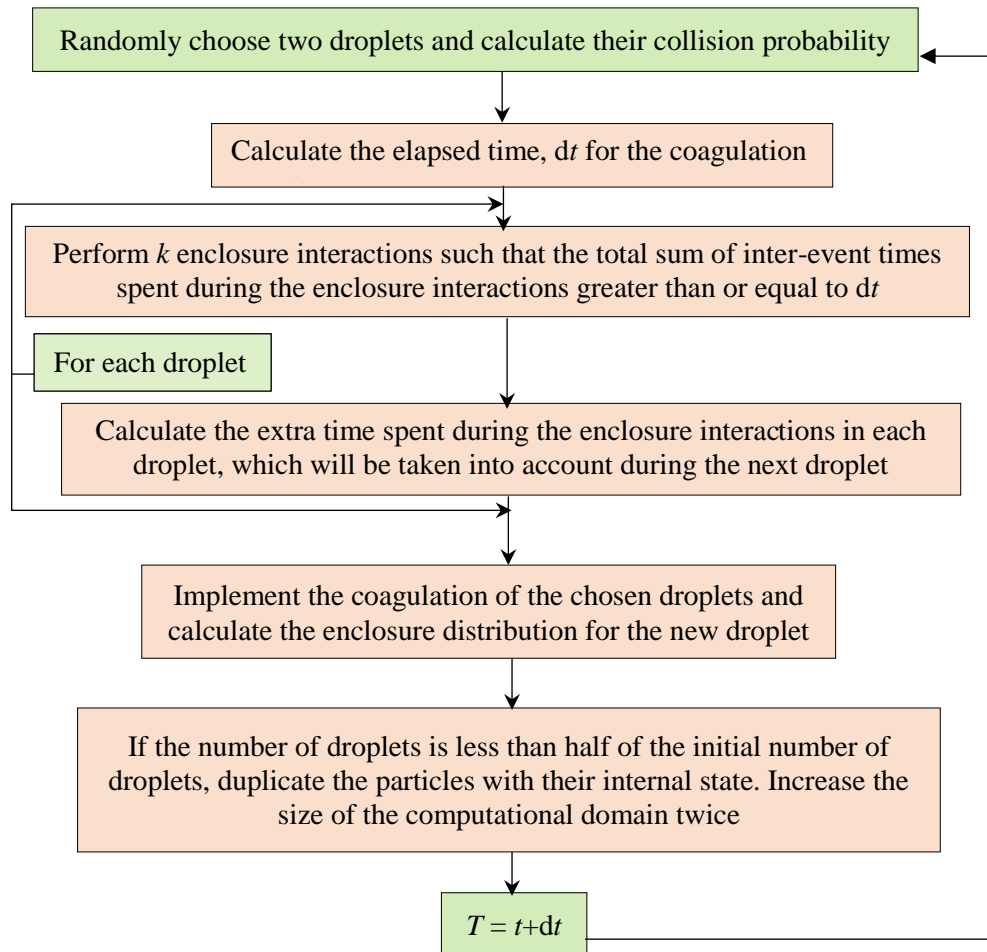


Figure 1.4 A typical flow chart of Monte Carlo algorithm (Efendiev, 2004).

Compared with Monte Carlo method, both the sectional methods and methods of moments have the following drawbacks:

1. There is no information about the history of each particle since the particles are described by means of their volume, so the information about the internal structure is lost (Kruis et al., 2000).
2. When multi-dimensional system is encountered, the sectional representation results in very complex algorithms (Kruis et al., 2000).

Monte Carlo simulation is a classical method to be used to overcome the above drawbacks. The major shortcomings of the Monte Carlo methods are the high computational cost (i.e., computational time, computer memory etc.) required in order to obtain satisfactory accuracy. This is because Monte Carlo methods are essentially stochastic methods and the computational error is inversely proportional to the square root of the total number of the numerical particles (Oran et al., 1998).

High performance computing (HPC) clusters are thus used in order to reduce the high computational cost (i.e., computational time, computer memory etc.) at high expense. Moreover, the development of parallel computing technique makes it possible to use many-core processors for Monte Carlo simulation, in which parallel computing is applied to stochastic processes (Wei and Kruis, 2013).

Since the Direct Simulation Monte Carlo (DSMC) method is a stochastic particle method, the movement of particles is independent of each other except for the inter-particle collisions (Wu and Lian, 2003). Thus, it is inherently justified to execute the DSMC method using the parallel processors in order to reduce computational time (Wu and Lian, 2003; Mohammadzadeh et al., 2013). A typical flow chart of parallel DSMC algorithm is shown in Figure 1.5 (Roohi and Darbandi, 2012).

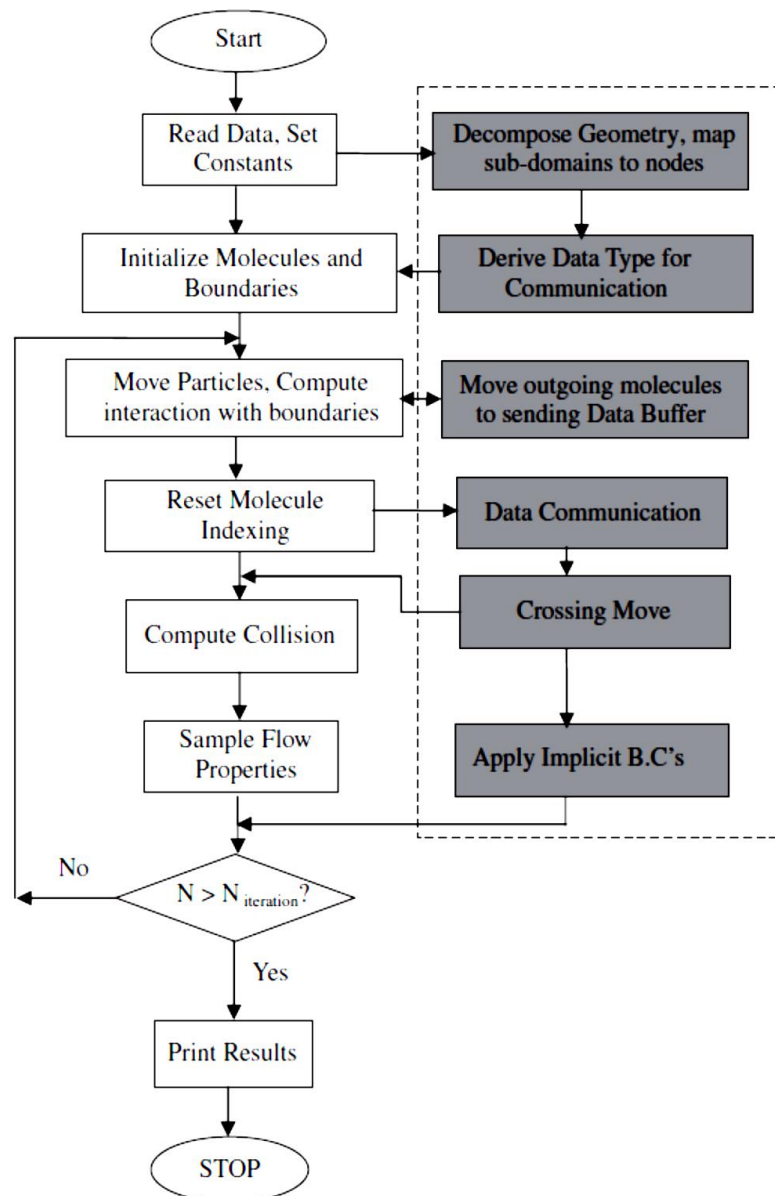


Figure 1.5 A typical flow chart of direct simulation Monte Carlo (DSMC) method (left) and parallel DSMC method (right) (Roohi and Darbandi, 2012).

Another method to accelerate the conventional Monte Carlo simulation which selects all processes (i.e., nucleation, surface growth and coagulation) randomly at a time, the new methods of Linear Process Deferment (LPDA) and Operator Splitting Monte Carlo (OSMC) are proposed by Patterson et al. (2006) and Zhou et al. (2014), respectively, which separates coagulation from other nucleation

and surface growth processes. In most of the conventional Monte Carlo methods, every simulation particle is associated with the uniform number of real particles. The accuracy of the simulation thus depends on the number of numerical particles used. Hence, it decreases the applicability of Monte Carlo method to the spatially resolved gas simulations, and regions with few physical particles cannot be modeled accurately. A stochastically weighted particle method (SWPM) is thus introduced by Rjasanow and Wagner (1996) to deal with this problem of simulation accuracy. A new stochastically weighted operator splitting Monte Carlo (SWOSMC) method based on the idea of operator splitting and a stochastic weight for every simulation particle is newly proposed in the present study. The purpose of this new method aims to solve complex aerosol dynamic problems with high accuracy and efficiency, which will provide a better knowledge of the evolution of aerosol system and a better deal with the multi-scale, multi-component and heterogeneous aerosol dynamics with high performance computing. In fact, parallel DSMC method has been studied and implemented in many fields such as multiphase flow, aerosol coagulation phenomena; molecular dynamics etc. (Kruis et al., 2000; Liffman, 1992; Mohammadzadeh et al., 2013). In the present study, further research development of implementing this new SWOSMC method to multi-scale aerosol systems will be presented.

However, in actual industrial and engineering applications, an inhomogeneous flow field is generally encountered which has a profound impact on aerosol dynamic processes. Those processes are dependent on local flow field variables (e.g., temperature and concentration). Thus, the solution for multidimensional PBE including convection and diffusion terms becomes

significant for aerosol dynamics in turbulent flow. Coupling the PBE of aerosol dynamics with CFD method provides a very promising approach to deal with the spatially inhomogeneous problems of aerosol dynamics (Kruis et al., 2012; Zhao and Zheng, 2013; Zhou and Chan, 2014; Zhou and He, 2014; Akridis and Rigopoulos, 2015; Amokrane et al., 2016). In laminar flow, the coupling of CFD to PBE can be easily accomplished via proper transformation of PBE. However, in turbulent flow, the closure problems arise due to the effect of turbulence on aerosol dynamic processes (e.g. coagulation, nucleation and growth) as such physical processes are highly dependent on the local field variables. Moreover, the relationship between turbulence, particle properties and collision kernels of aerosol dynamics is not well understood and is rarely reported due to their theoretical and experimental limitations (Lesniewski and Friedlander, 1995; Reade and Collins, 2000; Rigopoulos, 2007; Balachadar and Eaton, 2010; Minier, 2015). Thus, particular attention is paid to examine the effect of turbulence on aerosol dynamics and the evolution of PSD of aerosol dynamics in the present study.

Probability density function (PDF) methods based on a PDF transport equation of the full PSD have been proposed and used to overcome the closure problems due to interaction between turbulence and particle evolution in turbulent reactive flows (Pope, 1981; Pope, 1985; Valino, 1998; Sabel'nikov and Soulard, 2005; Meyer, 2010; Pope and Tirunagari, 2014; Consalvi and Nmira, 2016). Both PSD and particle number density distribution are treated without additional assumptions for closure via the transported PDF methods. The full PSD can thus be obtained directly without reconstructing it from moments. Moreover, complex and

arbitrary kernels of aerosol dynamics are allowed since no closure is required for the PBE. These PDF methods can be divided into three categories i.e., Eulerian particle method (Pope, 1981), Lagrangian particle method (Pope, 1985) and Eulerian field method (Sabel'nikov and Soulard, 2005). Both the advantages and disadvantages of the methods and possible improvements can easily be identified in the comparison between Eulerian and Lagrangian Monte Carlo PDF methods (Möbus et al., 2001; Zhang and Chen, 2007; Haworth, 2010; Jaishree and Haworth, 2012).

Lagrangian particle Monte Carlo algorithms (Pope, 1985; Jaishree and Haworth, 2012) have been regarded as the mainstream approach for solving PDF transport equations in most applications of PDF methods to date (Haworth, 2010; Haworth and Pope, 2011). A great number of notional particles that evolve according to the prescribed stochastic differential equations (SDE) (Celis and Silva, 2015) represents the PDF, and weighted averages over the particles in a small amount of neighboring grids are used to approximate the local mean quantities. As the mean velocity and turbulence scales are required before advancing in every time step, it is necessary to couple the Lagrangian particle method with a conventional CFD solver to formulate a consistent hybrid Lagrangian particle/Eulerian mesh PDF method (Jaishree and Haworth, 2012; Jangi et al., 2015). The main advantage of Lagrangian particle method relative to Eulerian PDF method is that the spatial-transport algorithm has much higher accuracy. The number of grid cells required for equivalent accuracy is thus considerably smaller and the total computational cost (i.e., computational time, computer memory etc.) of Lagrangian PDF is only proportional to the number of notional particles despite the special care required for

reducing statistical error. A consistent hybrid Lagrangian particle /Eulerian mesh PDF method (Jaishree and Haworth, 2012; Jangi et al., 2015) based on the work of Pope (1985) is proposed for the coupled CFD-Monte Carlo simulation of aerosol dynamics in turbulent flow in the present study. Further application of the coupled CFD-Monte Carlo method to turbulent reactive flows is also studied in the following content.

1.2 Research Motivation and Objectives

In the present study, a stochastically weighted operator splitting Monte Carlo (SWOSMC) method is first formulated based on the improvement of Monte Carlo (MC) method with the coupling of operator splitting technique and stochastic weight method. Then the SWOSMC method is coupled to computational fluid dynamics (CFD) in terms of Lagrangian probability density function (PDF) representation approximating the discretized population balance equation (PBE).

The objectives of the present study are as follows:

1. To gain a better understanding of the aerosol dynamic processes such as coagulation, nucleation, condensation etc. in aerosol dynamics in turbulent flows by the development of the stochastically weighted operator splitting Monte Carlo (SWOSMC) method;
2. To develop a novel coupled CFD-Monte Carlo/PDF method for spatially inhomogeneous aerosol dynamic system in turbulent flows with wide applicability by combining with a CFD method to formulate a CFD-based

aerosol dynamics method with applications to complex particle-fluid systems; and

3. To extend the CFD-Monte Carlo/PDF method for the application to turbulent reactive flows by including a chemical reactions module in this method.
4. This newly proposed CFD-Monte Carlo/PDF method is expected to render an efficient method for simulating complex aerosol dynamics in turbulent reactive flows and provides a better insight into the interaction between turbulence and the full PSD of aerosol particles.

1.3 Outline of the Thesis

Chapter 1 introduces an overview of the background and scope related to the present study, indicating that the knowledge gap of the numerical simulation of multi-scale interaction of complex aerosol dynamics in polydispersed turbulent reactive flows. The objectives of the present study are intended to fill this knowledge gap.

Chapter 2 provides a more detailed literature review of aerosol dynamics including the knowledge of aerosol dynamics obtained via the experimental and numerical studies, indicating the development and state-of-the-art that the researchers have acquired, and the shortcomings of these research areas and where the knowledge gap lies.

Chapter 3 provides theoretical fundamentals of the present study, which contains necessary mathematical and numerical models that will be used in Chapters 4 to 6.

Chapter 4 provides this newly proposed SWOSMC method with its validation and applications to simultaneous complex aerosol dynamics.

Chapter 5 presents this newly proposed CFD-Monte Carlo/PDF method with applications to the study of interaction between turbulence and aerosol dynamics in turbulent flows.

Chapter 6 provides the extension of this proposed and developed CFD-Monte Carlo method to turbulent reactive flows by including a chemical reaction module. This method is then used to study the soot formation in non-premixed turbulent reactive flows.

Chapter 7 provides the conclusions and major scientific findings revealed by the present study, and some recommendations for future work.

Chapter 2 Literature Review

2.1 Aerosol Dynamics in Multi-scale Systems

There are miscellaneous multi-scale systems concerning aerosol dynamics in nature as well as in human activities. Some typical examples regarding the aerosol dynamics in multi-scale systems will be reviewed briefly in the following sections.

2.1.1 Atmospheric Aerosols

A variety of liquids and solids existing as poly-dispersed phases in the atmosphere can be generally called atmospheric aerosols, which can be regarded as a two-phase system comprised of solid particles and fluid (air) (Valsaraj and Kommalapati, 2009). The typical physical properties of atmospheric aerosols including diameter, specific surface area, liquid water content as well as lifetime are shown in Table 2.1 (Valsaraj and Kommalapati, 2009). The mass concentrations and diameters of aerosols in different areas are shown in Table 2.2 (Valsaraj and Kommalapati, 2009). According to Table 2.1 and 2.2, the atmospheric aerosols can be regarded as a multi-scale system ranging from 10 nm to 10^6 nm or even larger.

Table 2.1 Typical physical properties of atmospheric aerosols (Valsaraj and Kommalapati, 2009).

Nature of droplet	Size (μm)	Specific surface area (m^2/m^3)	Liquid water content (m^3/m^3 air)	Typical lifetime
Aerosols	10^{-2} – 10	10^{-3}	10^{-11} – 10^{-10}	4–7 days
Fog droplets	1– 10	8×10^{-4}	5×10^{-8} – 5×10^{-7}	3 hours
Cloud drops	10 – 10^2	2×10^{-1}	10^{-7} – 10^{-6}	7 hours
Raindrops	10^2 – 10^3	5×10^{-4}	10^{-7} – 10^{-6}	3–15 minutes
Snowflakes	10^3 – 10^5	3×10^{-1}	–	15–50 minutes

Table 2.2 Mass concentrations and diameters of atmospheric aerosols (Valsaraj and Kommalapati, 2009).

Area	Concentration ($\mu\text{g}/\text{m}^3$)	Diameter (μm)
Urban	>100	0.03
Rural	30-50	0.07
Marine	>10	0.16

Many aerosol species are not generated directly, but are originated from complex reactions between gaseous precursors and aerosol species in the atmosphere and have complex physical properties and lifetimes (Valsaraj and Kommalapati, 2009), which forms complicated multi-scale problems. Hence, it is necessary to develop multi-scale numerical simulation methods. The various radiative mechanisms with cloud effects of atmospheric aerosols are shown in Figure 2.1 (Valsaraj and Kommalapati, 2009).

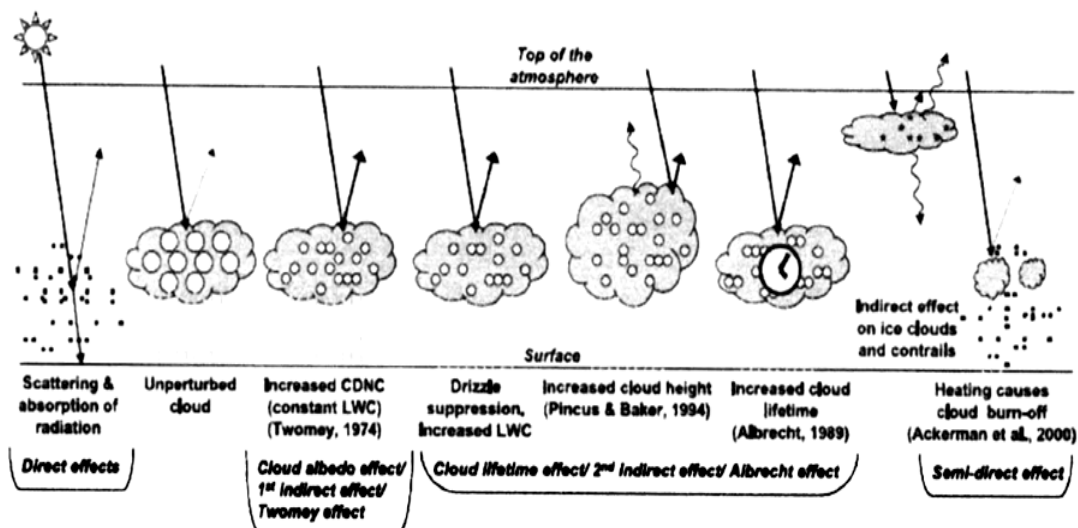


Figure 2.1 Various mechanisms with cloud effects of atmospheric aerosols (Valsaraj and Kommalapati, 2009).

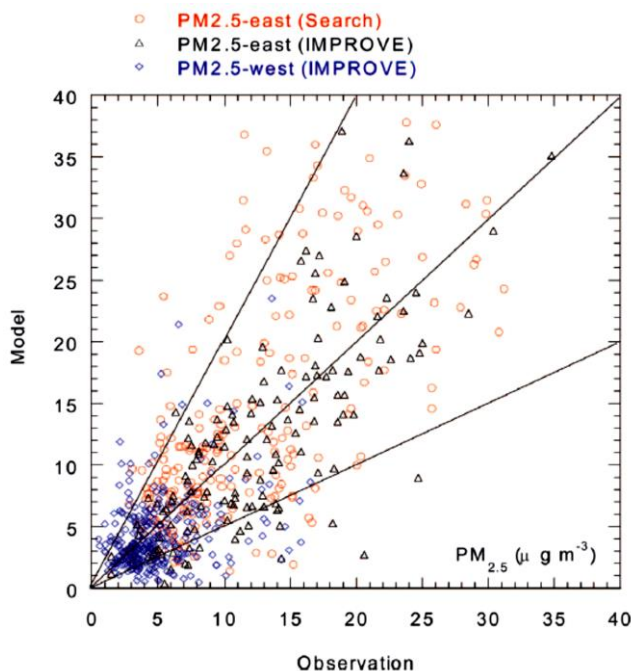


Figure 2.2 Scatterplot of daily average $\text{PM}_{2.5}$ concentrations from continental U.S. monitoring stations for the period of June 15-July 16, 1999 versus comparable CMAQ model estimates (Byun and Schere, 2006).

Many multi-scale models relating to atmospheric aerosols have been developed such as Community Multi-scale Air Quality (CMAQ) Modeling System (Byun and Schere, 2006), Multi-scale Global Aerosol-climate Model (GCM)

(Wang et al., 2014) and Multi-scale Atmospheric Transport and Chemistry Model (MATCH) (Robertson et al., 1999). However, more robust and versatile models are still needed to simulate atmospheric aerosols in multiple scales. The simulation results of $PM_{2.5}$ obtained by the GCM model were compared with that from observation in Figure 2.2 (Byun and Schere, 2006). A similar numerical simulation results of tracer transport obtained from MATCH model is shown in Figure 2.3 (Robertson et al., 1999).

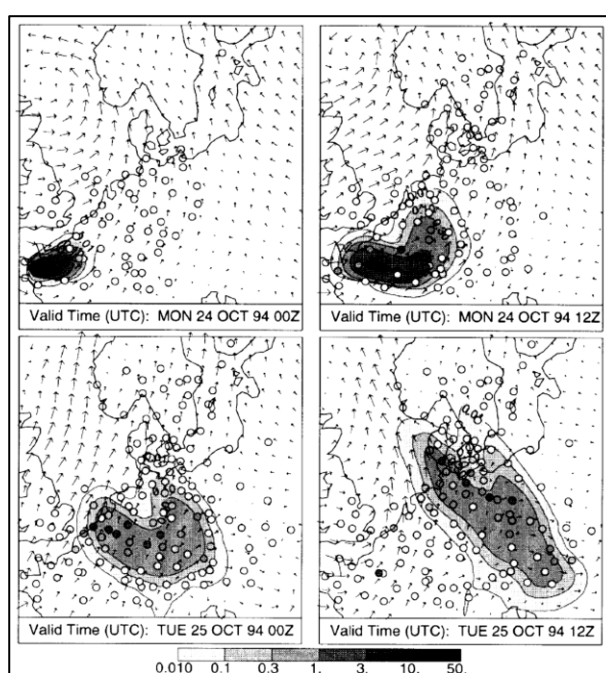


Figure 2.3 Calculated distribution of a passive tracer released from a surface point source using a fifth-order scheme in the horizontal advection (Robertson et al., 1999).

2.1.2 Multi-scale Fluid-particle Systems in Chemical Reactors

Multi-scale structure originates generally from the multi-phases occurring in fluid-particle industrial chemical reactors. Different numerical simulation methods, mainly Computational Fluid Dynamics (CFD) methods and other methods have been developed and applied to modeling the multi-scale behaviors of fluid-particle systems.

Fluidized Bed Reactor

Computational fluid dynamics (CFD) method is often used for the modeling of multi-scale reaction inside a fluidized bed reactor (FBR) (Zhuang et al., 2014; Wang et al., 2014; Deen and Kuipers, 2014; Klimanek et al., 2015; Lu et al., 2016). CFD approaches for the simulation of gas-solid flows in FBRs can be divided into two categories: Eulerian-Lagrangian and constant Eulerian–Eulerian methods (Zhuang et al., 2014). Compared with the Eulerian–Lagrangian method, in which the movement of particles is tracked individually, the Eulerian–Eulerian method treats particulate phase as a continuous phase (Zhuang et al., 2014).

The velocity vector profiles of both particle and gas phases of a fluidized bed reactor (Zhuang et al., 2014) is shown in Figure 2.4, which is obtained with a combined computational fluid dynamics (CFD) method and discrete element method (DEM) (Zhang et al., 2008). The main reaction parameter distribution profiles in the MTO FBR are shown in Figure 2.5.

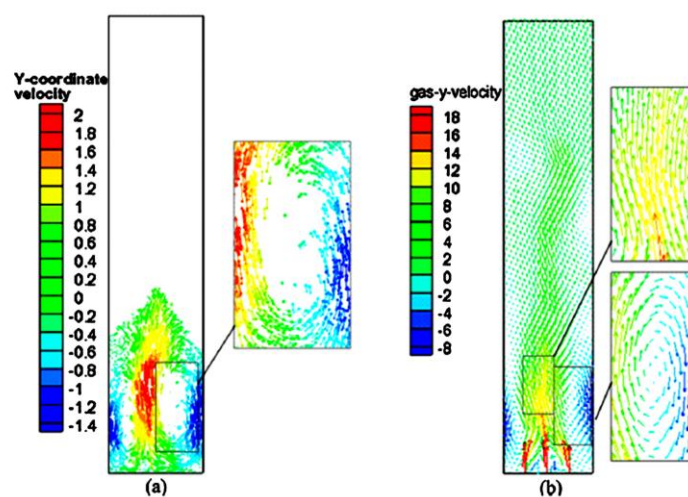


Figure 2.4 Velocity vector profiles inside a fluidized bed reactor obtained with computational fluid dynamics-discrete element method (CFD-DEM) method: (a) particle phase; and (b) gas phase (Zhuang et al., 2014).

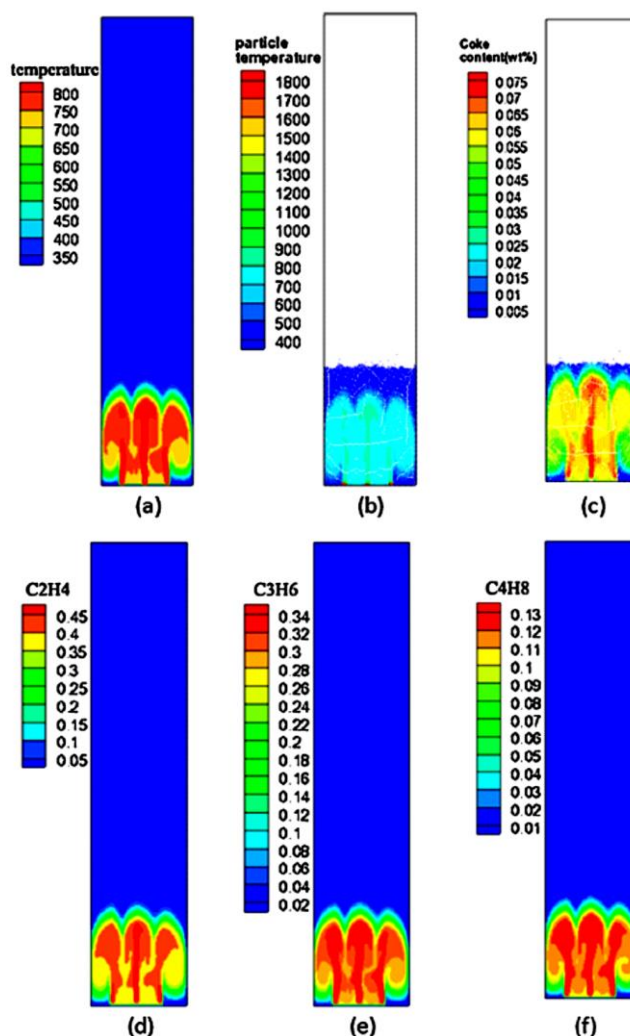


Figure 2.5 Main reaction parameter distribution profiles in the methanol to olefins (MTO) fluidized bed reactor (FBR) at $t = 0.052$ s: (a) gas-phase temperature; (b) particle temperature; (c) coke content; (d) ethane mole concentration; (e) propene mole concentration; and (f) butene mole concentration; space (velocity= 2.8 m/s, inlet feed temperature=723K, feed ratio of water to methanol=0(Zhuang et al., 2014).

Fixed Bed Reactor

Fluid flow through fixed bed of spheres is often accompanied by complex phenomena such as heat and mass transfer (Rong et al., 2014). Methods such as CFD method and DEM method together with stochastic methods such as Lattice Boltzmann Method (LBM) (Rong et al., 2014; Asensio et al., 2014; Mahmoudi et al., 2014; Brumby et al., 2015; Kruggel-Emden et al., 2016) are often used to simulate multi-scale particle-fluid systems in a fixed bed reactor.

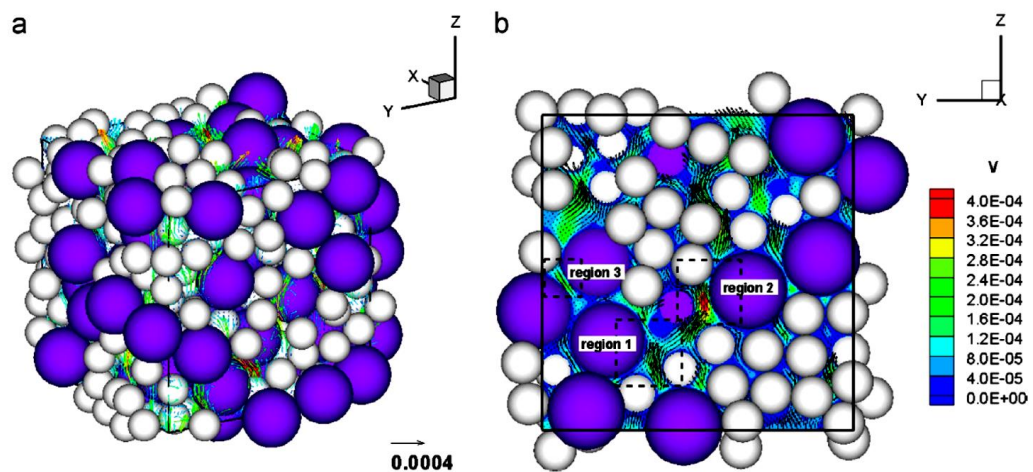


Figure 2.6 Parallel Lattice Boltzmann simulation results for flow within a fixed bed packed with the binary mixture of two types of spheres: (a) velocity vector; and (b) velocity contour and vector on the mid-plane (Rong et al., 2014).

Simulation results of velocity profiles and the spatial distribution of drag forces on particles for flow within a fixed bed packed with the binary mixture of two types of spheres obtained with parallel Lattice Boltzmann method (LBM) are shown in Figures 2.6 and 2.7, respectively. LBM shows its applicability to multi-scale modeling for a fixed bed reactor and offers an alternative to traditional CFD methods.

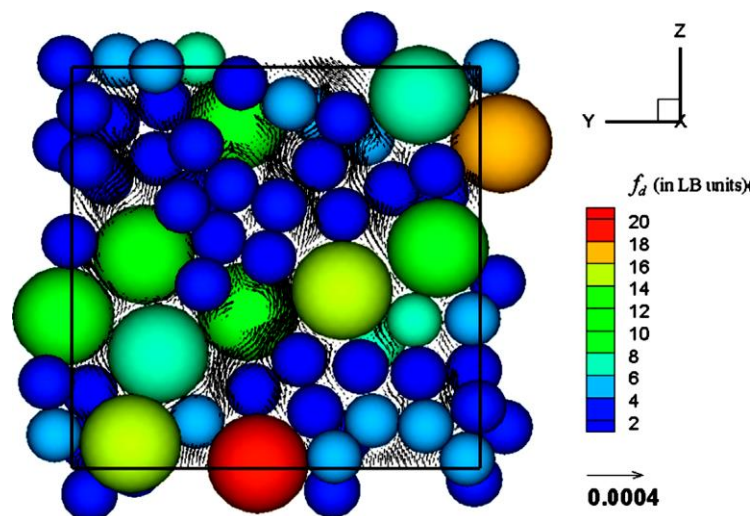


Figure 2.7 Parallel Lattice Boltzmann simulation results for flow within a fixed bed packed with the binary mixture of two types of spheres: spatial distribution of the drag forces on individual particle across the mid-plane (Rong et al., 2014).

2.1.3 Multi-scale Flows and Particle Issues

Another important application of multi-scale particle-fluid systems is the study of multi-scale flows (Nie et al., 2004; Koumoutsakos, 2005; Bergdorf and Koumoutsakos, 2006; Oñate et al., 2014; Zhang et al., 2014; He et al., 2014; Giannakopoulos et al., 2014; Li et al., 2015; Lee and Engquist, 2016). Multi-scale flow simulations using particles is a widely used method and considered to be an efficient one.

An example of coupling an atomistic method with continuous method for the reference solution of the flow of argon around a carbon nanotube is shown in Figure 2.8 (Koumoutsakos, 2005). It can be seen that the multi-scale method yields more reasonable numerical simulation results.

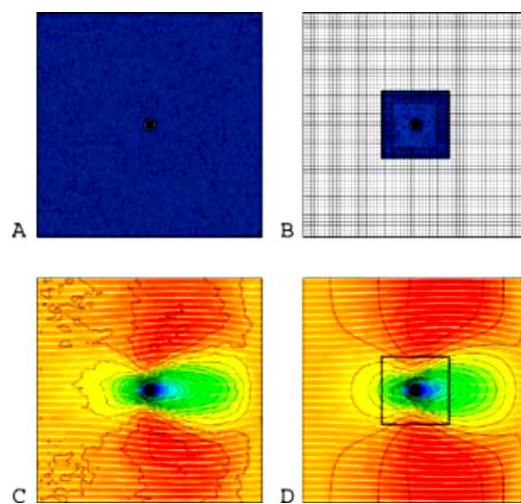


Figure 2.8 (a) Computational domain using a purely atomistic description; (b) Hybrid atomistic/continuum computational domain; (c) Velocity field for the reference solution averaged over 4 ns; and (d) Velocity field of the hybrid solution after 50 iterations (Koumoutsakos, 2005).

Another example of numerical simulation of multi-scale flow using combined particle method of dissipative particle dynamics and coarse-grained

molecular dynamics is shown in Figure 2.9. It can be seen that with the increase of coarsening parameters in both temporal and spatial directions, the resolution of simulation results increase significantly.

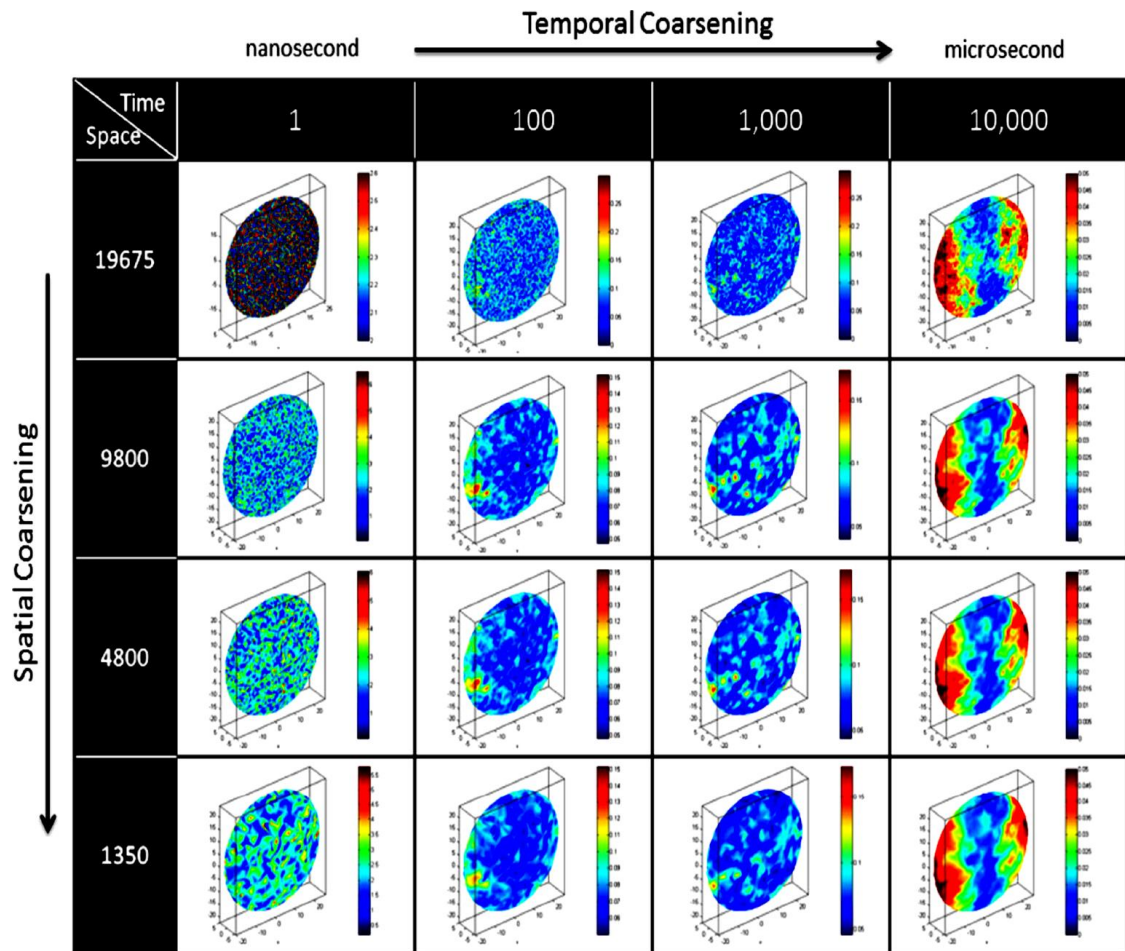


Figure 2.9 The velocity profiles of flowing platelets in blood plasma with a multi-scale method of dissipative particle dynamics and coarse-grained molecular dynamics (Zhang et al., 2014).

Particles issues are used herein to refer the multi-scale problems in relation to the simulation of particles behaviors such as synthesis, evolution, transport etc. A schematic diagram of nano particles synthesis is shown in Figure 2.10 (Balgis et al., 2014). The multi-scale particle methods mentioned above such as VM, DPD and DSMC could be well applied to particles issues herein.

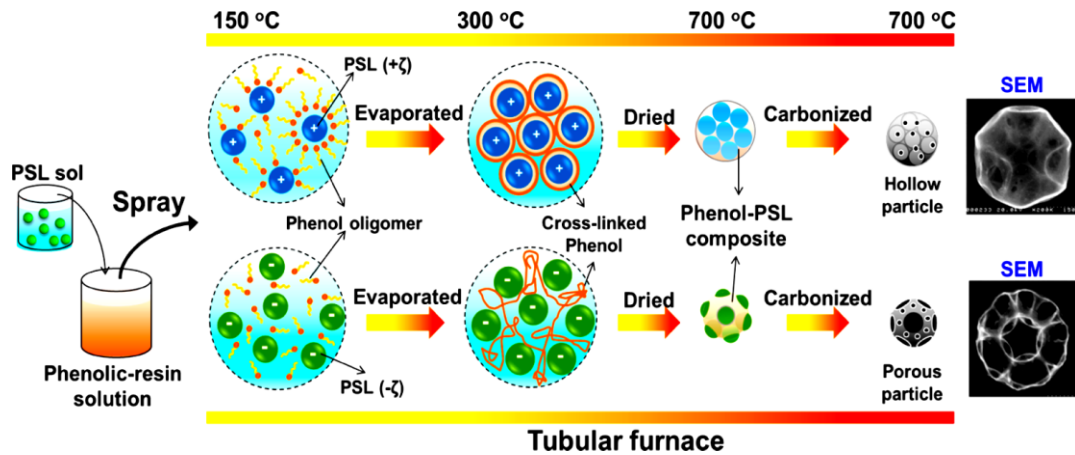


Figure 2.10 A schematic diagram of nano particles synthesis (Balgis et al., 2014).

This DSMC method has been widely used in the simulation of gas diffusion in porous nano structures (Ge and Gutheil, 2008; Dreyer et al., 2014), the prediction of particle behavior in gas-particle two-phase impinging streams (Makinde et al., 2013; Du et al., 2013) and the aerosol evolution (Kruis et al., 2000; Hao et al., 2013; Liffman, 1992; Wu and Lian, 2003; Palaniswaamy and Loyalka, 2008; Roohi and Darbandi, 2012; Du et al., 2013; Dreyer et al., 2014; He et al., 2015; Campbell et al., 2016). The simulation of gas diffusion via DSMC in porous nano structures is shown in Figure 2.11 (Dreyer et al., 2014).

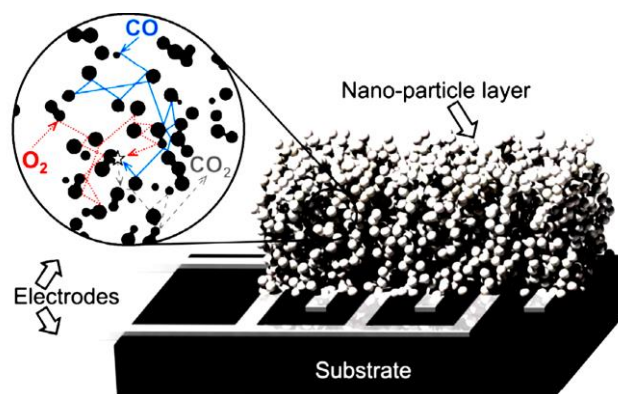


Figure 2.11 A schematic diagram of gas diffusion in nano structures (Dreyer et al., 2014).

2.2 Experimental investigation of aerosol dynamics

The experimental investigation of aerosol dynamics mainly includes the collection, examination and characterization of aerosol particles, which will be introduced respectively in the following sections.

2.2.1 Collection of Aerosol Particles

The collection of aerosol particles can be conducted in a batchwise way or continually such as continuous online sampling. Some online sampling methods have been developed particularly for the online sampling of aerosol particles originating from combustion (Chen et al., 1998; Maricq et al., 2003; Zhao et al., 2003; Jiménez and Ballester, 2005; Laitinen et al., 2010; Hess et al., 2016) and vehicle emissions (Chan et al., 2004; Alvarez et al., 2008; Ježek et al., 2015). Considering the impact of external electrostatic field, the collection of aerosol particles can be conducted in the presence of external electrostatic fields (Intra et al., 2014) or in the absence of them (Smith and Phillips, 1975). Figure 2.12 shows a typical example of online sampling system (Zhao et al., 2003).

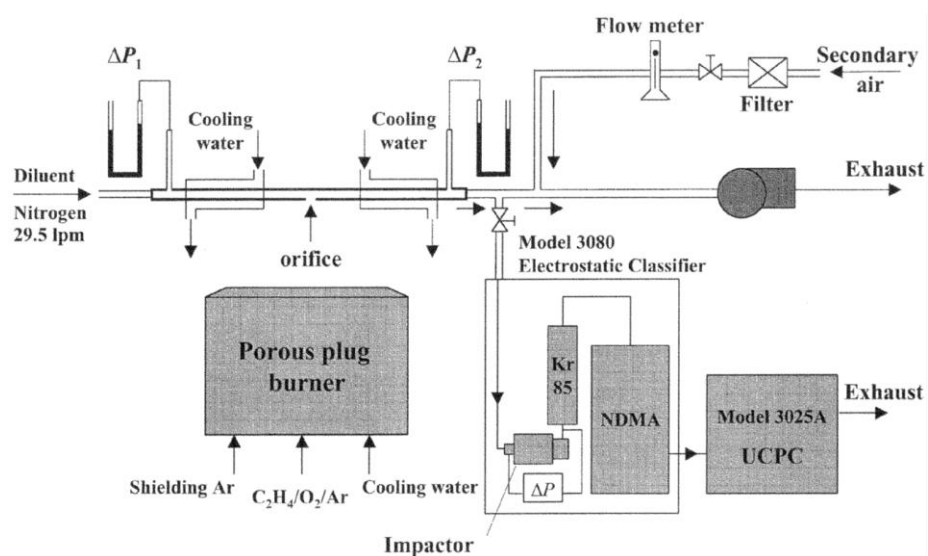


Figure 2.12 A schematic diagram of an online sampling system (Zhao et al., 2003).

2.2.2 Examination and Characterization of Aerosol Particles

Chromatography and mass spectrometry have been widely used for the analysis of small scale of aerosol particles after proper pretreatment. Nuclear magnetic resonance and Raman spectroscopy have also been used to examine more microscopic properties of certain aerosol particles such as soot. Laser desorption has been connected to mass spectrometry (Bouvier et al., 2007; Öktem et al., 2005; Laskin et al., 2010; Ozawa et al., 2016) to measure the relative abundance of organic components on soot particles.

For a larger scale examination of aerosol particles, optical methods such as transmission electron microscopy (TEM) and scanning electron microscopy (SEM) can be used. For a sample with large number of aerosol particles, light scattering and absorption measurements can be used to estimate particle diameters and obtain a multi-modal PSD (Erickson et al., 1964).

2.3 Numerical Methods for the Simulation of Aerosol Dynamics

Various numerical methods have been developed to solve Equation (1-1), the population balance equation (PBE) governing the evolution of particle number density as a function of particle size and time. The main numerical methods for aerosol dynamics include sectional methods (Jeong and Choi, 2001; Mitrakos et al., 2007; Agarwal and Girshick, 2012), method of moments (Lin and Chen, 2013; Yu et al., 2008; Park et al., 2013; Chen et al., 2014; Yu and Chan, 2015; Pollack et al., 2016) as well as stochastic method (Zhao et al., 2009; Zhao et al., 2012; Wei, 2013, Zhou et al., 2014; Liu et al., 2015; Liu and Chan, 2016 and 2017).

2.3.1 Sectional Method

Sectional methods can be classified into fixed sectional methods and moving sectional methods. The fixed sectional methods first proposed by Gelbard and Seinfeld (1980) use a grid placed on the particle type or state space with an a priori assumption of the shape of PSD in every section bin or grid cell (Patterson, 2007). The moving sectional methods proposed by Kumar et al. (1997) adjust the boundaries of section bins to account for the particle size changes due to aerosol dynamic processes.

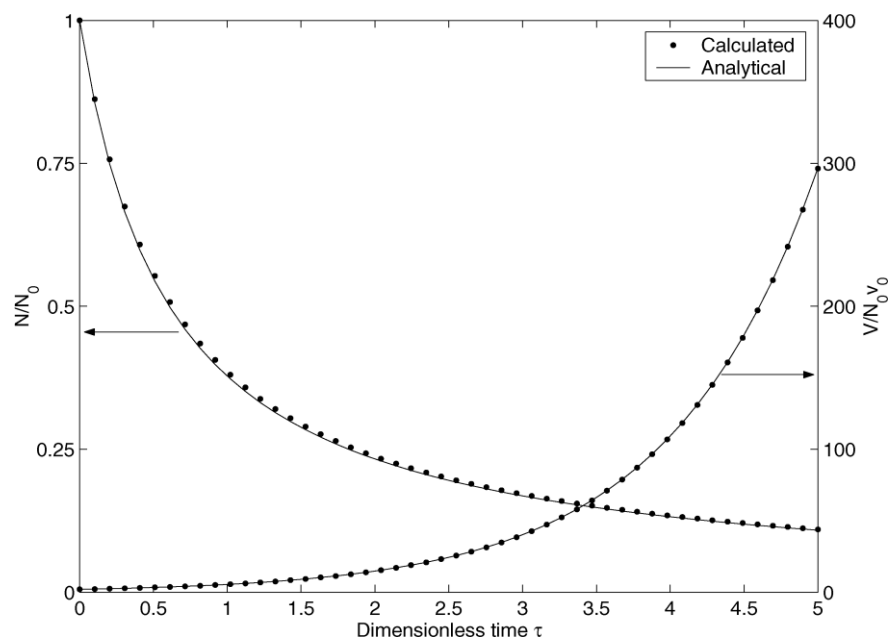


Figure 2.13 Comparison between sectional and analytical methods: normalized number and volume concentrations under constant coagulation and linear condensation (Mitrakos et al., 2007).

Figure 2.13 shows the evolution of the normalized particle number and volume concentrations of the aerosols as a function of the dimensionless time (Mitrakos et al., 2007). The decrease of normalized particle number due to coagulation as well as the increase of particle volume due to condensation are well

captured by numerical simulation compared with the analytical solution (Mitrakos et al., 2007) as is shown in Figure 2.18.

2.3.2 Method of Moments

The main advantage of methods of moments in the simulation for aerosol dynamics is the relatively low computational cost (i.e., computational time, computer memory, etc.) as a small number of additional equations i.e., the moments equations of the PSD are to be solved while the main disadvantage is the requirement of initial PSD in order to obtain the closure of the transport equations (Mitrakos et al., 2007).

However, a new method of moments i.e., Taylor-series expansion method of moments (TEMOM) using the Taylor-series expansion technique to dispose the collision terms and the fractional moments to obtain a new form for the moment equations without prior assumptions for PSD was proposed by Yu et al. (2008). Figure 2.14 shows the comparison of TEMOM method in comparison with other methods. It can be seen that the TEMOM method shows good agreement with other numerical methods.

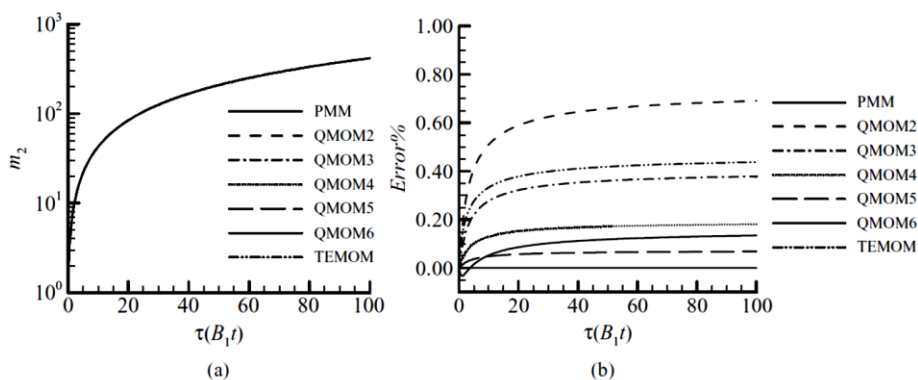


Figure 2.14 The second order moment and the relative error for various methods in the free molecular regime. The relative error denotes the ratio of second order moment from various methods to the QMOM with 6 points (Yu et al., 2008).

2.3.3 Stochastic Method

The direct simulation Monte Carlo (DSMC) method was first proposed by Bird (1994). The basic idea of DSMC is to use a set of numerical particles to represent the real physical particles. However, only the particle properties of interest such as momentum and mass are tracked. The random generation of collisions based on prescribed probability laws is justified by the molecular chaos (Baxter and Olafsen, 2007) in homogeneous grid cells. A review of the DSMC methods and some practical application in solving the Boltzmann equation can be found in Oran et al. (1998). Figure 2.15 shows the regimes of validity of DSMC and other methods.

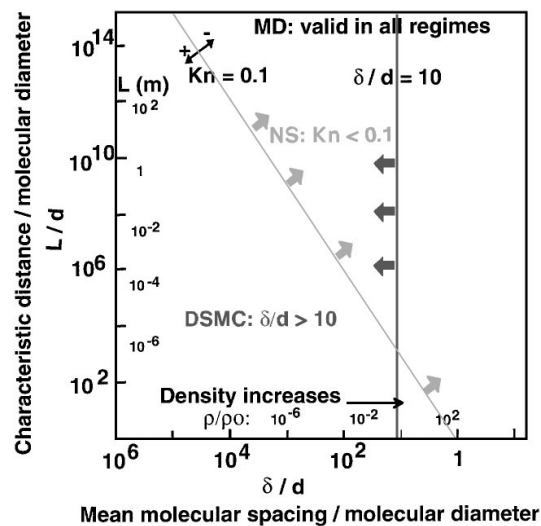


Figure 2.15 Regimes of validity of molecular dynamics, direct simulation Monte Carlo, and Navier-Stokes, as a function of the characteristic length scale and mean molecular spacing of a system (Oran et al., 1998).

2.4 Direct Simulation Monte Carlo Method

2.4.1 Overview

The direct simulation Monte Carlo Method (DSMC) proposed by Bird (1994) uses numerical particles to represent a large number of physical molecules or atoms, which is a well-established method in the simulation of non-equilibrium gas flows. The DSMC method models gas at the microscopic level and the gas physics is thus captured through the motion of particles and collisional interaction between them. The DSMC method is statistical in nature because of the probabilistical and phenomenological treatment of physical process like collision in order to reproduce the macroscopic behavior of particles (Wu and Lian, 2003).

The primary advantage of the DSMC method is that it can capture the non-equilibrium effects which may occur in aerosol dynamics due to the relatively high Knudsen number (denoted by Kn), which is defined as the ratio of the mean free path length of the gas to the characteristic length of interest (the aerosol size). As aerosol particles are of micro- or nano- level, it generally yields a Knudsen number falling into the transitional regime ($10^{-3} < Kn < 10$). By tracking representative particles through space and considering collisions between particles, the DSMC method can directly simulate the physics of aerosol dynamics. Mathematically, the Boltzmann equation can be derived by following DSMC procedures.

2.4.2 Particle Representation

Particles in a DSMC simulation are set to represent a large number of real gas particles (Rieffel, 1999). Each simulation particle can be considered as a representative sample from the physical particulate system or as an average of the real particles according to the mean field theory. Particles are generally considered to be point particles or spheres with associated properties such as species, velocity and internal energy. The actual shape of molecules and the associated three-dimensional force fields are generally neglected for computational simplicity.

Collisions between particles are treated probabilistically using corresponding models. The common collisional models include hard sphere (HS) model, variable hard sphere (VHS) model, generalized hard sphere (GHS) model, variable soft sphere (VSS) model and some other models (Bird, 1994).

The operation of collision and sampling steps requires particles to be grouped into the cells of certain computational cells. The particles thus need to be sorted properly into corresponding groups. Collisions between the particles make it possible for the properties of gas to be transmitted through bulk flow. The exact calculation of collision kinematics involves many physical properties of particles such as the particles' trajectories, angles of incidence and impact parameter which is much costly. So collisions are calculated statistically between particles residing in the same computational cell. After being grouped into certain cells, a list of possible collision pairs is thus formed. A common method to decide whether collision happens is the acceptance-rejection method. Once the collision model and sampling scheme are determined, the collision probability is the function of the relative velocities, collision cross section and the number density of particles in

the cells. However, the collision probability is also related to the time step previously set and the particle weight, which will be introduced in Chapter 4.

A pair of particles is accepted for collision if the collision probability mentioned above is greater than a random number. The average collision rate is equal to that given by the kinetic theory, which guarantees the reliability of the statistical collision models. Several schemes had been proposed to be the criteria of collision occurrence such as the time counter and no time counter methods by Bird (1994).

Once a pair is selected for collision, momentum and energy are exchanged, the actual trajectories and dynamics of the particles are not taken into account in determining the collision mechanics. This is because the distribution function based on mean field theory is applied to the whole cell being considered. Instead, the scattering angle and degree of inelasticity can be selected statistically in order to generate post collision properties. Energy and momentum are obviously conserved in each collision.

2.4.3 Algorithm and Numerical Simulation Parameters

The DSMC method assumes that particle movement can be decoupled from collisional behavior in a small time step. Particles then move along straight line paths with discrete changes in velocity and energy caused by collisions. In order to accomplish this, the simulation is broken up into time steps for the magnitude of which are small compared to the average time between collisions (He and Zhao, 2016). In this small interval of time, these two processes can realistically be treated as independent.

A complete DSMC simulation consists of a series of discrete time steps or iterations. During each iteration, particles are moved and collisional pair is chosen and computed. The typical algorithm of a single iteration in the DSMC method is as follows:

- Step 1: Move particles;
- Step 2: Perform boundary interaction;
- Step 3: Sort particles into cells;
- Step 4: Select collision pairs;
- Step 5: Compute collision mechanics; and
- Step 6: Sample macroscopic properties of interest.

The first five operations are performed in each iteration. The sixth step is performed only when flow properties are desired. In the present study, the common numerical simulation parameters include particle weight, W_P , time step and grid cell size.

Particle Weight

Each simulation particle in DSMC simulation represents a large number of real particles (Guan et al., 2014). The ratio of the number of numerical particles, N_S to the number of physical particles, N_R (or real particles) is defined as the particle weight.

$$W_P = N_R/N_S \quad (2-1)$$

The smaller the particle weight, the larger number of numerical particles and thus better resolution of the flow physics. However, the larger number of numerical

particles means larger computational cost (i.e., computational time, computer memory, etc.). So the particle weight is selected to strike a reasonable balance between resolution of results, and computational cost and efficiency.

In traditional DSMC method, numerical particles are associated with equal weight regardless of the broad PSD, in which the particle number density in different particle size ranges may be quite different. The resulting statistical error and limited particle size spectrum will no doubt restrict the application of the DSMC method (Zhao et al., 2009). One method to deal with this problem is to introduce variable particle weights. For example, varying weights in the radial direction are used in the axisymmetric flows. In this case, the particle weight is increased in cells away from the axis to counteract the increasing volumes of these cells. Moreover, different weighting scales can be used to increase resolution in regions of the flow field with low particle number density or to increase computational efficiency where there is an excessive number of particles. This is why the stochastic weights are associated with numerical particles in the present study.

There is a problem of continuity on the interface concerning the usage of varying weights i.e., cells across the interface are with different weights. A discontinuity in mass flux across the interface is thus created when a particle crosses the interface and suddenly represents a different number of real particles. This discontinuity can be overcome by allowing a probability that the particle is either cloned when moving into a cell with a lower particle weight or destroyed when moving into a cell with a higher particle weight. The scheme can be described as follows:

$$W_P^{\text{old}} > W_P^{\text{new}} : P_{\text{clone}} = W_P^{\text{old}} / W_P^{\text{new}} - 1 \quad (2-2)$$

$$W_P^{\text{old}} < W_P^{\text{new}} : P_{\text{destroy}} = W_P^{\text{old}} / W_P^{\text{new}} \quad (2-3)$$

where W_P^{old} , W_P^{new} , P_{destroy} and P_{clone} represent the particle weights of the old cell, the particle weight of the new cell, the probability of the particle to be destroyed and the probability that the particle to be cloned, respectively. The clone-destroy operation conserves mass flux across the interface when many crossings are averaged. The stochastically weighted Monte Carlo method will be further described in Chapter 4.

Time Step

A certain finite number of time steps are used to decouple the movement of particles from collisions. In order to do this, the time step must be a small fraction of the mean time between collisions. The exact expression is dependent on the collision model employed but is in general a function of density and temperature. For purpose of statistical accuracy, it is also desirable that a particle not remain in a single cell for a large number of time steps. A high residence time tends to bias the sampling of macroscopic properties. The time step should then be set at a large enough value so that the majority of particles moving at the bulk fluid velocity will cross a given cell in a small number of time steps. Residence time and mean collision time provide bounds for the selection of a simulation time step.

Grid Cell Size

Grid cells in computational domain is used in DSMC to group particles for the purposes of calculating collisions and sampling macroscopic properties.

The size of the computational cells is limited by the constraints of physical accuracy and computational efficiency. As previously mentioned, collisions are calculated statistically between pairs of particles residing in the same cell. The two particles participating in a collision may be separated in space by as much as one cell dimension. In a real gas, two particles will not collide if they are separated by more than one mean free path. This provides a limit on the size of the computational cell. Ideally, cell dimensions should be smaller than the local mean free path such as 30 percent of the mean free path at all points as recommended by Bird (1994).

Sampling of Macroscopic Properties

The macroscopic properties can be taken as the average of the local properties of the molecules consisting of the gas. Density, velocity and temperature are the zeroth, first and second order moments of the velocity distribution function. Since the DSMC method directly depicts the distribution function, flow field results can be determined by sampling particles properties and calculating the moments of the distribution function of the sample. The computational grid is used to group particles for the purpose of sampling their properties and calculation is also conducted in every cell.

Calculation of smooth flow properties requires a large sample size in order to accurately describe the distribution function as the statistical noise is generally proportional to the inverse of the square root of the sample size (Darbandi et al., 2010). One of the methods to reduce the statistical noise is to sample over a number of iterations to increase the sample size and thus reduce the simulation fluctuations. In time dependent flows, it is often necessary to perform an ensemble average over many different simulations to obtain acceptable simulation results.

2.5 Operator Splitting Monte Carlo Method

2.5.1 Overview

Differential equations, including partial differential equations (PDE) and ordinary differential equations (ODE) have gained a wide range of engineering and scientific applications in terms of models of various physical phenomena. These differential equations are becoming increasingly complicated as the models to be described are becoming more and more complicated, representing increasingly complicated physical phenomena. It is common that a model contains different terms (operators) reflecting different physical or chemical processes. Consider the general dynamic equation (GDE) (Friedlander, 2000) in Equation (2-4), it contains convection, diffusion, nucleation, growth and coagulation terms. These different terms reflecting different aspects of the model appear in the same equation, making it rather difficult to analyze and solve both analytically and numerically.

$$\frac{\partial n}{\partial t} + \nabla \cdot D \nabla n = \left[\frac{\partial n}{\partial t} \right]_{\text{coag}} + \left[\frac{\partial n}{\partial t} \right]_{\text{grow}} + \left[\frac{\partial n}{\partial t} \right]_{\text{nucl}} \quad (2-4)$$

where the subscripts coag, grow and nucl represent the processes of coagulation, surface growth and nucleation, respectively.

Operator splitting based on the idea of divide and conquer is a very efficient and successful strategy to deal with those complex PDEs (Mclachlan and Quispel, 2002). The idea behind operator splitting is that the overall evolution operator is written as a sum of evolution operators for each operator (term), that is, one just splits the model into a set of sub-equations, where each sub-equation is of

a type for which solution to the equation can be found more easily. The overall numerical method is then formed by picking an appropriate numerical scheme for each sub-equation and piecing the schemes together by operator splitting (Holden et al., 2010).

Splitting methods arise when a vector space can be split into a sum of two or more parts that are each simpler to integrate than the original equation, which are composed to form the integrator once a splitting is constructed (Mclachlan and Quispel, 2002). Consider a simple time dependent differential equation, $dx/dt = X(x)$ with x within phase, M where X is a vector field on phase M , the splitting methods involve the following three important steps (Mclachlan and Quispel, 2002):

1. Choosing a set of vector fields, X_i such that $X = \sum X_i$;
2. Integrating either exactly or approximately for each X_i ; and
3. Combining these solutions to yield an integrator for X .

Consider the following Cauchy problem, the splitting method can be formulated as follows:

$$\frac{dU}{dt} + A(U) = 0, U(0) = U_0 \quad (2-5)$$

where A is some unspecified operator. Consider the following solution: $A = A_1 + A_2$ is assumed and then one can solve the sub-problems more easily (Holden et al., 2010).

$$\frac{dU}{dt} + A_j(U) = 0, U(0) = U_0, j=1, 2, \dots \quad (2-6)$$

with formal solutions as follows:

$$U_j(t) = e^{-tA_j}U_0, j=1, 2, \dots \quad (2-7)$$

In its simplest form, the operator splitting reads as follows: let $t_n = n \cdot \Delta t$ (Δt is small and positive) (Holden et al., 2010). Approximately, it is written as:

$$U(t_{n+1}) = e^{-\Delta t A_1} e^{-\Delta t A_2} U(t_n) \quad (2-8)$$

For commuting operators, $e^{-tA_1} e^{-tA_2} = e^{-tA}$, the method would be exact. Holden et al. (2010) suggested that an operator splitting may be considered as the method of choice if the operators are weakly coupled, that is, if the interaction of the different physical phenomena has a long time scale, an operator-splitting scheme will be efficient over a wide range of sizes for the splitting steps. Furthermore, it may be the only feasible method for higher dimensional problems. On the other hand, if the operators interact significantly over a short time scale, the operator splitting may be subject to severe restrictions on the splitting step.

For nonlinear operators, Holden et al. (2010) pointed out that interaction between elementary operators is often nonlinear, and splitting them into separate steps may result in large and unwanted errors. Operator splitting has been applied widely to many areas such as celestial mechanics, molecular dynamics, accelerator physics and biology diffusion-reaction system.

2.5.2 Operator Splitting Schemes

The Equation (2-4) includes various aerosol dynamic processes. Operator splitting is very efficient in solving such evolution equation. In the implementation

of this method, the time interval $[0, t]$ is discretized into many sections with Δt_i denoting one time step. The solution $n(t)$ can be constructed by a classical Euler method (Zhou et al., 2014). Instead of integrating all the physical processes simultaneously in one timestep (denoted as $\exp(\Delta t X)$), the operator splitting method divides the integration into multiple steps, as follows (Zhou et al., 2014):

$$\exp(\Delta t X) = \exp(\Delta t X_d) \exp(\Delta t X_s) + O(\Delta t^2) \quad (2-9)$$

$$= \exp(1/2 \Delta t X_d) \exp(\Delta t X_s) \exp(1/2 \Delta t X_d) + O(\Delta t^3) \quad (2-10)$$

$$= \exp(1/2 \Delta t X_s) \exp(\Delta t X_d) \exp(1/2 \Delta t X_s) + O(\Delta t^3) \quad (2-11)$$

where X_d denotes nucleation and surface growth processes, which is solved by deterministic integration method, and X_s denotes coagulation, which is solved by stochastic method. Eq. (2-9) is of first-order accuracy while Equations (2-10) and (2-11) are of second-order accuracy. The operator splitting schemes are shown as Figure 2.16 (Zhou et al., 2014):

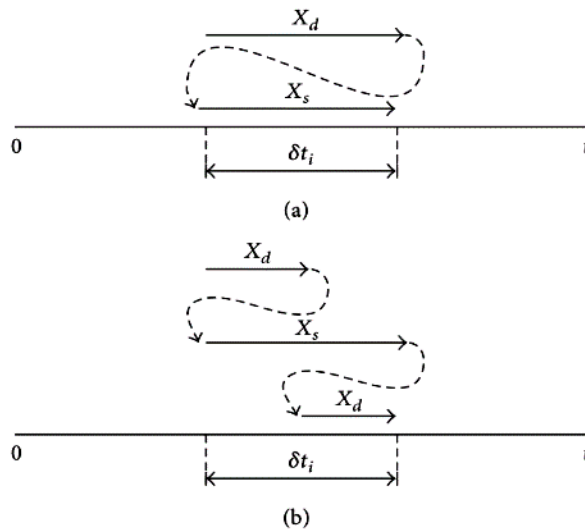


Figure 2.16 Operator splitting schemes: (a) first-order Lie scheme; (b) second-order Strang scheme (Zhou et al., 2014).

2.5.3 Implementation of Operator Splitting

The flowchart of operator splitting for solving GDE is shown in Figure 2.17 (Zhou et al., 2014). The GDE including deterministic processes (nucleation, surface growth) and stochastic process (coagulation) can be solved efficiently through solving the different aerosol processes separately and making further approximations, which neglect the diffusion and convection terms under certain conditions.

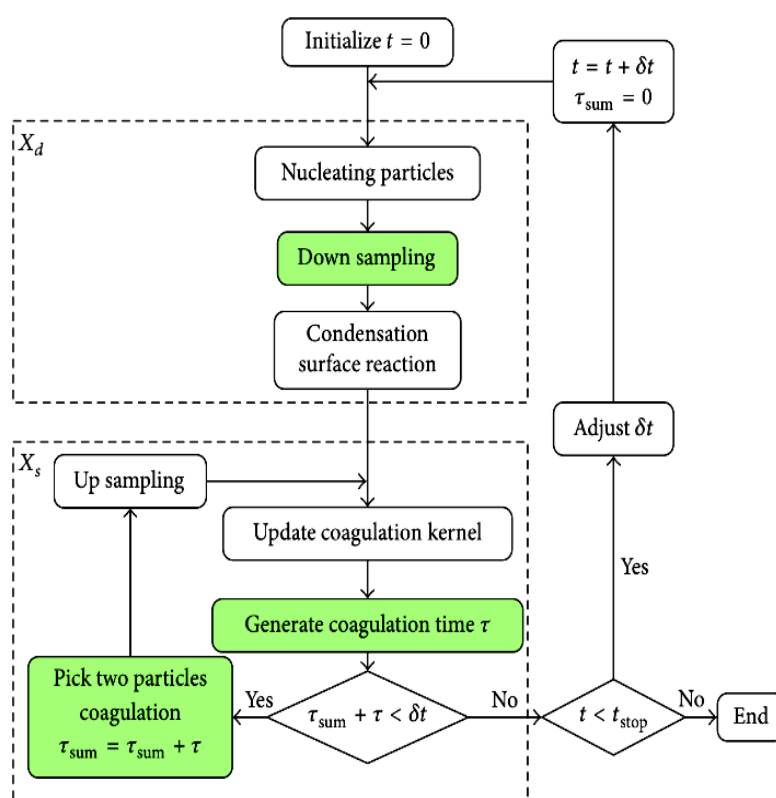


Figure 2.17 Flowchart of the operator splitting steps. (X_d and X_s have the same meaning with those in Equation (2.9) (Zhou et al., 2014).

The specific implementation of the coupling of stochastic soot formation to gas-phase chemistry using operator splitting is presented here. An operator splitting technique is used to solve the two parts of problem with ODE solver (Chemkin codes)

and Monte Carlo (MC) solver, respectively (Celnik et al., 2007). The governing equations are as follows:

$$\frac{df_i}{dt} = W_d(x_1, x_2, x_3) + W_s(x_1, x_2, x_3) \quad (2-12)$$

where f_i is parameter of interest, W_d and W_s are deterministic processes and stochastic processes, respectively. Then Equation (2-12) can be solved as follows:

ODE solver:

$$\frac{df'}{dt} = W_d(x'_1, x'_2, x'_3), f'_i(t_0) = f_i(t_0), t_0 < t < t_0 + h/2 \quad (2-13)$$

MC solver:

$$\frac{df''}{dt} = W_s(x''_1, x''_2, x''_3), f''_i(t_0) = f'_i(t_0 + h/2), t_0 < t < t_1 \quad (2-14)$$

ODE solver:

$$f'''_i(t_0) = f''_i(t_0 + h/2), t_0 + h/2 < t < t_1 \quad (2-15)$$

Finally, the computed values are assigned at the step endpoint.

$$f(t_1) = f''_i(t_1) \quad (2-16)$$

2.6 Weighted Monte Carlo Methods

2.6.1 Overview

In most of the conventional Monte Carlo methods, each simulation particle is associated with the uniform number of particles. The accuracy of the numerical

simulation thus depends on the number of numerical particles used (Zhao et al., 2005). This decreases the applicability of Monte Carlo method alone to the spatially resolved gas simulations, by which regions with few physical particles cannot be modeled accurately. In most Monte Carlo methods, a subsystem out of a total system is simulated. In general, numerical particles are equally weighted with a value of V/V_s , where V and V_s are the volume of the whole system and those of the subsystem, respectively (Zhao et al., 2009). Consider a system with a total particle number concentration of $1 \times 10^{10} \text{ m}^{-3}$ contains 1×10^4 numerical particles, so each simulation particle represents 10^6 real particles and the weight can be defined as the ratio of the number of real particles to that of the numerical particles, which is 1×10^6 . It is obvious by this definition that every numerical particle represents the same number of real particles. However, there is insufficient number of particles at the edges of the size spectrum, which makes it impossible to accurately capture the particle size distribution in this area using Monte Carlo method alone (Zhao et al., 2010). This becomes especially significant when the particle size distribution function is displayed in the usual logarithmic representation (Zhao et al., 2009).

2.6.2 Different Weighting Numerical Particles Schemes

The concept of weighting numerical particles is widely used as described above to overcome the conflict between large number of real particles and limited computational capacity (Zhao et al., 2009). A stochastically weighted particle method (SWPM) was thus introduced by Rjasanow and Wagner (1996) to deal with this problem of simulation accuracy, in which each simulation particle was associated with a stochastic weight, i.e., the number of real particles that they are associated with. With this SWPM, a larger number of numerical particles with

smaller stochastic weights can be applied in regions with lower density than was the case with basic DSMC. A similar problem could occur in zero-dimensional particle coagulation problems, in which the resolution of the upper end of the PSD in the DSMC simulation can be quite low because of the small number of numerical particles over there and thus causes a great statistical error. Different weighted schemes are proposed to deal with these problems (Eibeck and Wagner, 2001; Zhao et al., 2009; DeVille et al., 2011; Liu and Chan, 2017). The particle-weighting scheme proposed by Eibeck and Wagner (2001) can be further generalized into mass flow algorithm (MFA) by the proper derivations.

2.7 CFD-Population Balance Modelling of Aerosol Dynamics

In zero-dimensional simulation of aerosol dynamics, the spatially homogeneous flow field is assumed, neglecting the spatial inhomogeneity and coupling between the dispersed phase (aerosol particles) and continuous phase (fluid). However, the spatial inhomogeneity and inter-phase interaction become significant in most scientific and engineering applications. In order to obtain more accurate simulation results, a better control over particle size distribution and design of the equipment related to particulate processes, the population balance modelling (PBM) coupling with CFD to realize the multi-dimensional simulation of aerosol dynamics is required (Zhao and Zheng, 2013). CFD-PBM methods for aerosol dynamics are thus formulated to account for the spatial inhomogeneity and inter-phase interaction of aerosol dynamics in many practical applications (Kruis et al., 2012; Zhao and Zheng, 2013; Zhou and Chan, 2014; Zhou and He, 2014; Akridis and Rigopoulos, 2015; Amokrane et al., 2016; Liu and Chan, 2016). Taking into the consideration on inter-phase interaction between the particulate

phase and fluid phase, the coupling between the PBM and CFD codes can be divided into one-way coupling, two-way coupling or even four-way coupling. In one-way coupling, only the influence of fluid phase on particulate phase is considered (Zucca et al., 2007; Kruis et al., 2012; He and Zhao, 2016). In two-way coupling, the interaction between particulate phase and fluid phase are taken into account while the inter-particle interaction is neglected (Boivin et al., 2000; Pialat et al., 2006; Zhang and You, 2015). However, due the complexity of implementation, four-way coupling between the PBM and CFD codes is rarely reported (Zhao and Zheng, 2013; He and Zhao, 2016).

According to the simulation methodology for dispersed phase i.e., aerosol particles, the CFD-PBM methods can be classified into Eulerian-Eulerian models and Eulerian-Lagrangian models. In the Eulerian-Eulerian models, the deterministic methods such as method of moments (Settumba and Garrick, 2004; Balthasar and Frenklach, 2005; Zucca et al., 2006; Chen et al., 2011; Basavarajappa and Miskovic, 2016) and sectional methods (Jeong and Choi, 2003; Wen et al., 2005; Nere and Ramkrishna, 2006; Mitrakos et al., 2007; Agarwal and Girshick, 2012) are used to directly solve the PBE (i.e., Equation (1-1)) of aerosol particles. Meanwhile, in the Eulerian-Lagrangian models, stochastic methods such as Monte Carlo methods (Kruis et al., 2012; Zhao and Zheng, 2013; Fede et al., 2015; He et al., 2015; Consalvi and Nmira, 2016) are used to simulate the evolution of PBE of aerosol particles. The deterministic methods, which solve the PBE based on the Eulerian reference frame, are easier and more straightforward to couple with the Eulerian models of hydrodynamics of fluid phase than stochastic methods. However, the deterministic PBM methods for aerosol dynamics exhibit relatively

lower resolution on particle dynamics and are unable to consider polydispersity of particles. Besides these, deterministic PBM methods are unable to capture the history information and are at disadvantage to get more than two physical properties of particles (Zhao and Zheng, 2013). Stochastic PBM methods i.e., Monte Carlo PBM methods avoid all these disadvantages of the deterministic PBM methods except for a relatively higher computational cost (i.e., computational time, computer memory etc.), which can be overcome with the high-speed development of computer hardware and parallel computing techniques (Zhou et al., 2014; Xu et al., 2015).

2.8 Transported PDF Methods for Turbulent Reactive Flows

2.8.1 Overview

Transported PDF methods have been developed to overcome the closure problems due to interaction between turbulence and particle evolution in turbulent reactive flows by many researchers (Pope, 1981; Pope, 1985; Valino, 1998; Sabel'nikov and Soular, 2005; Meyer, 2010; Haworth, 2010; Pope and Tirunagari, 2014; Consalvi and Nmira, 2016). No additional assumptions are made for closure of PSD and particle number density distribution via the transported PDF methods. The work of Di Veroli and Rigopoulos (2010) was the first paper to develop a Lagrangian Monte Carlo method for solving the PDF of the PSD in a reactive precipitation problem and this method was used on an aerosol condensation problem in Di Veroli and Rigopoulos (2011). The concept was applied to LES in Pasmazoglou et al. (2014) and to deal with the aggregation in Pasmazoglou et al. (2016). The theory underlying transported PDF methods was provided in detail by

Fox (2003). Additionally, the complex and arbitrary kernels of aerosol dynamics are allowed since no closure is required for the PBE.

Transported PDF methods can be divided into two categories i.e., Eulerian PDF methods (Pope, 1981; Pope, 1985) and Lagrangian PDF methods (Pope, 1994; Jenny et al., 2001), respectively. Improvements of the PDF methods such as Eulerian field methods (Valiño, 1998; Sabel'nikov and Soulard, 2005; Jaishree and Haworth, 2012; Consalvi and Nmira, 2016) have also been proposed., The transported PDF is approximated by an ensemble of particles that remain fixed on the nodes of a CFD grid for the Eulerian particle method, but is approximated by an ensemble of particles that move along a CFD grid in accordance with the flow field obtained by the CFD codes for the Lagrangian particle method (Rigopoulos, 2007). Eulerian field method has been proposed in recent years, where the transported PDF is approximated by an ensemble of stochastic fields obtained via the CFD codes (Rigopoulos, 2007). Compared to Lagrangian particle methods, the Eulerian field methods are more compatible with conventional CFD codes and is thus possible to have higher computational efficiency (Jaishree and Haworth, 2012). The advantages and disadvantages of different transported PDF methods are available in the comparison between Eulerian and Lagrangian Monte Carlo PDF methods (Möbus et al., 2001; Zhang and Chen, 2007; Haworth, 2010). A modelled composition PDF transport equation is given in Equation (2-17) (Pope, 1985):

$$\begin{aligned} & \frac{\partial \rho f_\phi}{\partial t} + \frac{\partial \rho \tilde{u}_i f_\phi}{\partial x_i} + \frac{\partial \rho S_{\alpha} f_\phi}{\partial \psi_\alpha} = \\ & + \frac{\partial}{\partial x_i} \left[\Gamma_{T\phi} \frac{\partial (\rho f_\phi / \langle \rho \rangle)}{\partial x_i} \right] - \frac{\partial [S_\alpha(\psi) \rho f_\phi]}{\partial \psi_\alpha} \end{aligned} \quad (2-17)$$

where the terms on the left-hand side are the accumulative and the convection transport terms in real space due to the mean velocity and the convection transport terms in composition space. The terms on the right-hand side are the turbulent-diffusivity and the source terms.

Due to the high dimensionality of velocity and composition PDF transport equation, it is computationally intractable to use the traditional finite-difference or finite-volume methods to solve the PDF transport equation. Monte Carlo simulations are thus used to solve the PDF transport equation, which can handle the curse of dimensionality. The disadvantage of Monte Carlo simulation codes is the statistical noise that must be minimized or controlled before the valid comparisons can be made with other methods or experimental data. But the advantages of Monte Carlo simulation codes for PDF methods are as follows:

- Computational cost (i.e., computational time, computer memory, etc.) only increases linearly with the number of independent variables (Pope, 1985);
- Realizability and boundness of all variables are assured. Since the chemical source term is treated exactly, the mass conservation is guaranteed at the notional-particle level (Fox, 2003); and
- Using particle partition, the particle codes exhibit excellent scalability on distributed computing platforms. However, for turbulent reactive flows, additional care must be taken when carrying out chemical lookup tables to avoid scale-up problems (Fox, 2003).

2.8.2 Eulerian PDF methods

In Eulerian PDF methods, the notional particles are associated with certain cell centers. Notional particles are used to represent a set of composition vectors (Fox, 2003). The number of notional particles, N in the l th grid cell is denoted by N_l . The set of composition vectors of notional particles in the l th grid cell can be written as follows (Amani and Nobari, 2010):

$$\{\phi\}_l = \{\phi^{(1)}, \dots, \phi^{(N_l)}\} \quad (2-18)$$

where $\phi^{(n)}$ is the composition vector of the n th notional particle, which represents the composition PDF at a certain location.

The estimation of statistical quantities including mean velocity ($\langle U \rangle$), the turbulent diffusivity (Γ_T) and turbulent frequency (ω) are obtained via a separate finite volume method to the Eulerian PDF codes. The estimated scalar mean in the l th grid cell is given as follows:

$$\{\phi_a\}_{N_l}(x_l, t) = \sum_1^{N_l} \phi_a^{(n)}(x_l, t) \quad (2-19)$$

where (x_l, t) is the position and time of the notional particle in the l th grid cell. The number of notional particles N_l in l th grid cell, N_l can be different in different flow zones (Amani and Nobari, 2010).

Two types of processes can be identified in Eulerian PDF methods, i.e., (1) intra-cell processes such as micro-mixing, chemical reactions and aerosol dynamic processes; and (2) inter-cell processes including convection and diffusion processes. The intra-cell processes are treated the same in both the Eulerian and

Lagrangian PDF methods while the inter-cell processes are treated differently due to the discrete representation of space in terms of x_l (Fox, 2003). The inter-cell flow variables between a rectangular cell and its four neighboring cells in the Eulerian PDF method (Pope, 1981) are shown in Figure 2.18.

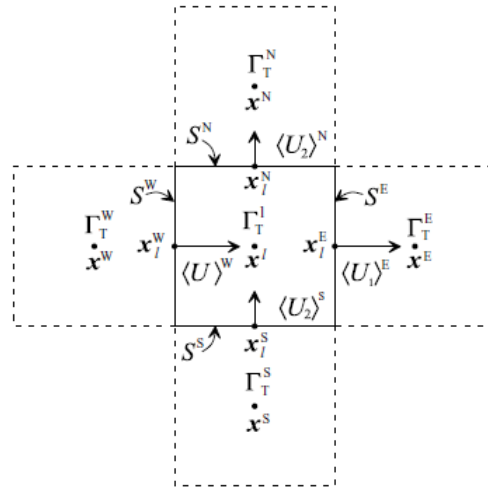


Figure 2.18 Flow variables for the l th grid cell and four neighboring cells in Eulerian PDF methods (Fox, 2003).

The basic procedures of numerical implementation of Eulerian PDF methods are as follows (Fox, 2003):

- Step 1: Computing the effective inflow rates for every cell in the flow domain;
- Step 2: Computing the numbers of notional particles, that flow into the l th grid cell from the neighboring cells; and
- Step 3: Randomly selecting the new set of notional particles at the l th grid cell with replacement from the old sets of notional particles. The random selection is carried out by generating Gaussian random numbers $U \in [0, 1]$. It is noteworthy that for constant-density, statistically stationary flows, the effective flow rates are constant

so that Steps 1 and 2 are completed only once while the Monte Carlo simulation is advanced by repeating *Step 3* and computing intra-cell processes including aerosol dynamics.

The advantages of Eulerian PDF methods are as follows (Fox, 2003):

- The locations of notional particles correspond to the grid cells used in the finite volume code;
- The estimated statistical quantities are found using cell averages since all notional particles have equal weight;
- It is straightforward to implement mixing and chemical reactions and intra-cell processes;
- By combining with finite volume code, it is easy to implement the spatial transport algorithm on orthogonal grids; and
- The computational time expense increases linearly with the total number of notional particles and the algorithm is easy to parallelize.

Although Eulerian PDF methods have these advantages, they also have fatal disadvantages (Fox, 2003):

- The effective flow rates of every cell are highly grid-dependent and computing them for arbitrary non-orthogonal grids; Very fine grids are thus required in order to obtain grid-independent results;
- Numerical diffusion remains the principal shortcoming because the computation of spatial transport is limited to first-order, up-wind schemes,

which leads to a relatively large number of notional particles in order to reduce statistical error to an acceptable level.

- If flow rates vary significantly over the computational domain, special algorithms are needed to ensure that $N_l^k \geq 1$.

2.8.3 Lagrangian PDF Methods

In Lagrangian PDF methods, Lagrangian notional particles follow trajectories in the velocity-composition-physical space originating from random locations in the physical space. Each notional particle is associated with corresponding position, composition and velocity. Notional particles with various weights can be used to represent the inhomogeneity of the flow field. The information of mean velocity and turbulent fields (i.e., turbulent diffusivity and frequency) is provided by a finite volume code coupled with the Lagrangian PDF methods. In the case of constant-density flows, the position and number density of a notional particle after one time step, Δt can be written as follows (Fox, 2003):

$$X^n(t+\Delta t) = X^n(t) + [\langle U \rangle(X^n(t), t) + \nabla \Gamma_T(X^n(t), t)] \Delta t + 2\Gamma_T(X^n(t), t) 1/2 \Delta W \quad (2-20)$$

$$N^n(t+\Delta t) = N^n(t) + [C_N/2 (\langle N^n(t) \rangle - N^n(t)) + \dot{W}_i(N, Y)] \Delta t \quad (2-21)$$

Moreover, the composition of a notional particle is given as follows:

$$d\phi^{(n)}/dt = C_\phi/2 \omega(X^n(t), t) (\phi_\alpha^* - \phi_\alpha^n) + S(\phi^{(n)}) \quad (2-22)$$

where ΔW_i is a Gaussian pseudo-random number for representing the stochastic fluctuations of Wiener process with mean, $\langle \Delta W_i \rangle = 0$ and covariance, $\langle \Delta W_i \Delta W_j \rangle = \Delta t \delta_{i,j}$, C_N is the characteristic scale concerning micro mixing, $\dot{W}_i(N, Y)$ is the

source term for accounting the variation of particle number density, Γ_T is the turbulent diffusion coefficient, $\langle U \rangle$ is the average velocity. $\phi^{(n)}$ is the vector properties of the notional particles. C_ϕ is the characteristic factor and $S(\phi^{(n)})$ is the source term related to chemical reactions and aerosol dynamic processes. The superscript ‘*’ refers to any notional particle. In Monte Carlo simulation, the Equations (2-20) to (2-22) are simulated numerically with fractional time stepping. By applying a local Courant-Freidrich-Lewy (CFL) condition, the time step, Δt can be determined from the finite volume code (Jenny et al., 2001). For steady flow, the local time stepping technique can be used in the simulation (Möbus et al., 2001). In order to maintain uniform statistical error, the particle weights $\omega^n(t)$ are initialized according the grid cell volumes and then modified during the Monte Carlo simulation (Fox, 2003).

The principal steps of the implementation of the Lagrangian PDF methods are shown in Figure 2.19. The first step is to initialize the particle properties and turbulence fields. Then the simulation time step Δt is obtained based on the local CFL condition. The flow field is advanced with the finite volume code and return turbulent fields. Monte Carlo simulation is then carried out with the turbulent fields from the finite volume code to compute $X^n(\Delta t)$. Meanwhile, the intra-cell processes of micro-mixing, chemical reactions and aerosol dynamic processes are computed to determine the $\phi^n(\Delta t)$. The particle-field estimates are obtained with the updated particle properties. The simulation time is then incremented by Δt . The last step is to check if the simulation time has reached the stopping time.

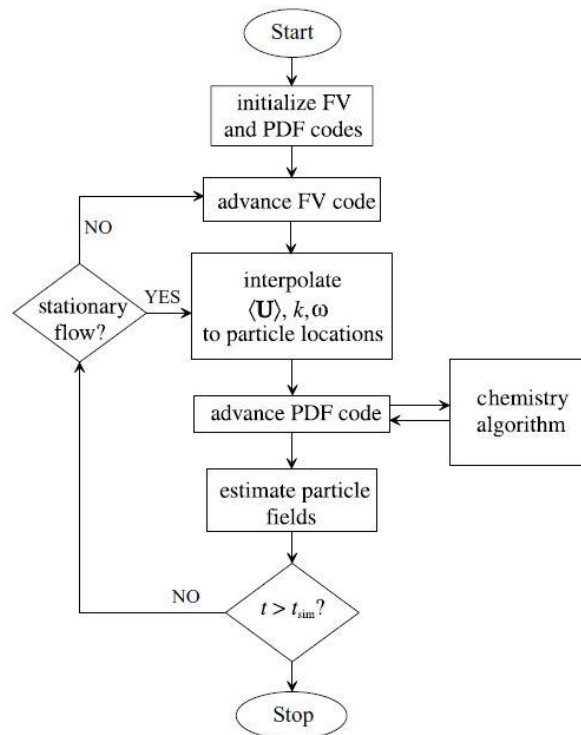


Figure 2.19 Flow diagram of Lagrangian PDF methods (Fox, 2003).

The main advantages of Lagrangian PDF methods are as follows (Fox, 2003):

- The spatial transport algorithm has much higher accuracy, which reduces the number of grid cells required for equivalent accuracy when compared to Eulerian PDF methods;
- The numerical algorithm for intra-cell processes is straightforward and the local mass conservation is guaranteed; and
- The total computational cost (i.e., computational time, computer memory, etc.) only increases linearly with the number of notional particles.

The main disadvantages of Lagrangian PDF methods are that the tracking and sorting of notional particles on non-orthogonal grids is computationally intensive (Pope, 1994), particularly in the case of significant variation of local time

scale over the computational domain. However, local time stepping technique can be used to reduce the computational cost to some extent (Möbus et al., 2001).

2.8.4 Improvements of the PDF Methods

Besides the Eulerian particle based PDF methods and Lagrangian particle based PDF methods, stochastic Eulerian field (SEF) PDF methods (Valiño, 1998; Sabel'nikov and Soulard, 2005; Jaishree and Haworth, 2012; Consalvi and Nmira, 2016) have been proposed to improve the existing PDF methods. In the SEF-PDF methods, the notional particles are replaced by notional Eulerian fields that evolve according to the stochastic partial differential equations (PDEs) (Celis and Silva, 2015). The stochastic PDEs of the SEF method can be solved using Eulerian CFD algorithm.

A deterministic Eulerian field method coupled with direct quadrature method of moments (DQMOM) is developed to a multi-environment PDF-MEPDF method (Jaishree and Haworth, 2012), which shows higher computational efficiency in comparison to Eulerian and Lagrangian particle based PDF methods. More recent improvements of the PDF methods can be found in the literature (Meyer, 2010; Pope and Tirunagari, 2014; Consalvi and Nmira, 2016).

2.9 Summary of Literature Review

The fundamental concepts, knowledge and methods of aerosol dynamics in multi-scale systems are reviewed in this chapter to shed light on the development and state-of-the-art that the researchers have acquired as well as the knowledge gap for this research area. The literature review is summarized as follows:

1. Aerosol dynamics in multi-scale systems is widely encountered in engineering and environmental areas including the production of functional aerosol particles and the prevention of industrial emissions. It is of great importance to gain a better insight and more intrinsic understanding on aerosol particles including the generating and evolution mechanisms and other physiochemical properties.
2. Both experimental and numerical methods play important roles in the investigation of aerosol dynamics. However, experimental study is quite limited to relatively simple cases and would be become difficult even impossible as far as more complex and practical cases are concerned. Numerical simulation provides an alternative solution to the study of aerosol dynamics under complex conditions, which is also the focus of the present study. The advantages of numerical methods are mainly their high capability and low cost.
3. Numerical methods for aerosol dynamics can be divided into two categories (i.e., deterministic methods and stochastic methods). Deterministic methods provide an efficient and accurate approach for the numerical simulation of aerosol dynamics. However, the inherent limitations of deterministic methods are also very obvious and difficult to overcome, among which the inability to provide history information of particles and difficulty to apply to multi-dimensional and multi-scale problems are fatal in the study of complex aerosol dynamics. Stochastic methods such as Monte Carlo methods have unique advantages in dealing with multi-scale and multi-dimensional

problems concerning aerosol dynamics and can provide the history information and arbitrary number of variables.

4. Various modifications have been made to increase the computational efficiency and guarantee the computational accuracy of Monte Carlo methods. In order to solve multi-dimensional problems involving aerosol dynamic processes, Monte Carlo codes of PBE are coupled to CFD codes to formulate the coupled CFD-PBM methods, which will also be presented in Chapters 5 and 6.

Chapter 3 Theoretical Fundamentals of the Present Study

3.1 Introduction

This chapter briefly presents the theoretical fundamentals related to the newly proposed CFD-Monte Carlo/PDF method including the population balance equation, Monte Carlo methods, Eulerian-Lagrangian models for multi-phase flows, and transported PDF methods for turbulent reactive flows.

3.2 Population Balance Equation

3.2.1 Overview

Population balance equations (PBE) in Equation (1-1) can be derived from the Boltzmann equation (Cercignani, 1988) as shown in Equation (3-1), which describes a gas particle behavior. PBE is derived to describe how populations of separate entities evolve or vary in specific properties over time. They are a set of integro-partial differential equations, which give the behavior of a population of particles from the analysis of a single particle behavior in local conditions (Ramkrishna, 2000). Particulate systems feature the birth and death of particles.

$$\frac{\partial f}{\partial t} = \left(\frac{\partial f}{\partial t}\right)_{\text{force}} + \left(\frac{\partial f}{\partial t}\right)_{\text{diff}} + \left(\frac{\partial f}{\partial t}\right)_{\text{coll}} \quad (3-1)$$

where f is an unspecified function. The term on the left-hand side (LHS) is the accumulative term. On the right-hand side (RHS), the first term is the source

term due to external force, the second term is the diffusion term and the last term is the cumulative effect of inter-particle collisions.

Population balance equation (PBE) is used to describe the evolution of PSD of particulate systems mathematically (Ramkrishna, 2000), which is a transport equation of particle number density function or other variables of particles such as mass and volume dependent on space coordinates, time and particle size. Depending on actual aerosol dynamic processes, different source terms such as coagulation, nucleation and growth may appear in PBE, as shown in Equation (2-4). Combining different source terms into different physical processes, the PBE (i.e., in Equation (2-4)) is obviously an integro-differential equation. There has been a large number of research studies concerning the solution of PBE in spatially homogeneous domain i.e., zero dimensional PBE (Efendiev, 2004; Yu et al., 2009; Chan et al., 2010; Zhou and Chan, 2011; Geng et al., 2013; Yu and Chan, 2015; Liu et al., 2015; Liu and Chan, 2017). Zero dimensional PBE here refers to the PBE expressed in terms of particle number density, which is independent of any spatial coordinate. The aerosol particles involve no convection or diffusion process. The particulate phase is not affected by any fluid phase either.

The fundamental assumption in the formulation of PBE is that there is a unique particle number density for every spatial coordinate in the particle scalar space (Ramkrishna, 2000), which consists of internal (quantitative characterization of particle properties) and external (particle location in the physical space) coordinates. Both the internal and external coordinates of particles may be discretized under certain conditions. This renders the theoretical basis on which the discretization of the PBE of particulate systems is performed. Another fundamental

assumption of population balance theory is that the variation rate of any particle state vector is dependent only on the state of the particles of interest as well as the local variables of the continuous phase, which renders the coupling between the transport equation and the population balance equation (Ramkrishna, 2000).

3.2.2 The Self-preserving Behavior of PBE

The self-preserving behavior (also called self-similar behavior) is associated with the invariant domains in the space of the independent variables within which the solution to PBE i.e., the reconstructed particle size distribution (PSD) remains identical or partially identical (Ramkrishna, 2000). A similar transformation for the PSD function was proposed by Swift and Friedlander (1964) and Friedlander and Wang (1966) to obtain self-preserving solutions to the PBE, which are asymptotic forms and independent of the initial PSD.

Based on the assumption that the fraction of the particles in a given size range is a function only of particle volume normalized by the average particle volume (Epstein and Ellison, 1987), the similarity transformation can be carried out as follows:

Firstly, the dimensionless particle size distribution can be written as:

$$\frac{n(v,t)dv}{N_{\infty}} = \psi_v\left(\frac{v}{\bar{v}}\right)d\left(\frac{v}{\bar{v}}\right) \quad (3-2)$$

where v is particle volume, \bar{v} is the average particle volume, N_{∞} is the total number of particles, ψ_v is a dimensionless function whose form is invariant with time. By rearranging Equation (3-2), it can be written as:

$$n(v,t) = \frac{(N_\infty)^2}{\phi} \psi_v(\eta_v) \quad (3-3)$$

where $\eta_v = v/\bar{v} = N_\infty v/\phi$, represents dimensionless particle volume, ϕ is the total volume of all the particles. Equation (3-3) is the similarity transformation for the PSD in terms of particle volume, $n(v,t)$. The boundary conditions are that $n(v,t) \rightarrow 0$ for $v \rightarrow 0$ and $v \rightarrow \infty$. The form of ψ_v can be determined in two-steps. Firstly, the special form of PSD function $n(v,t)$ in Equation (3-3) is tested by substituting in the Equation (1-1) with appropriate collision frequency function, $\beta(v,u)$. If the similar transformation is in accordance with the PBE, one can obtain an ordinary integro-differential equation for ψ_v as a dimensionless function of η_v . Secondly, a solution to the transformed equation is to be found subject to the following integral constraints:

$$\int_0^\infty nvdv = \phi \quad (3-4)$$

$$\int_0^\infty ndv = N_\infty \quad (3-5)$$

Based on the assumption that the fraction of the particles in a given size range is a function only of particle diameter normalized by the average particle diameter, which is similar to Equation (3-2) and it can be written as:

$$\frac{n(d_p,t)d(d_p)}{N_\infty} = \psi_d\left(\frac{d_p}{\bar{d}_p}\right)d\left(\frac{d_p}{\bar{d}_p}\right) \quad (3-6)$$

Let $\eta_{\bar{d}} = d_p/\bar{d}_p$ and $\bar{d}_p = (\phi/N_\infty)^{1/3}$, the obtained similarity transformation for the PSD in terms of $n(d_p,t)$ can be written as:

$$n(d_p, t) = \frac{(N_\infty)^{4/3}}{\phi^{1/3}} \psi_d(\eta_d) \quad (3-7)$$

where $\eta_d = d_p(N_\infty/\phi)^{1/3}$, represents dimensionless particle diameter, d_p is the particle diameter, ψ_d is a dimensionless function of particle diameter, and the other variables have the same meaning as in Equation (3-3). Similarity transformation can be used to obtain closed form solutions for the upper and lower ends of the PSD while numerical method such as Monte Carlo method can be used to match the solutions for intermediate-size particles. More details regarding the existence and feasibility of the self-similar solution to the PBE can be found in the similarity analysis of PBE (Ramkrishna, 2000).

3.2.3 The Solution of PBE

Except for very special and limited cases to which analytical solutions to PBE exist (Zhou et al., 2014; Liu and Chan, 2017), it is quite difficult to solve PBE with analytical methods. Thus, numerical methods e.g., sectional methods (Jeong and Choi, 2001; Mitrakos et al., 2007; Agarwal and Girshick, 2012), method of moments (Yu et al., 2008; Lin and Chen, 2013; Park et al., 2013; Chen et al., 2014; Yu and Chan, 2015; Pollack et al., 2016) as well as Monte Carlo method (Zhao et al., 2009; Wei, 2013, Zhou et al., 2014; Liu et al., 2015; Liu and Chan, 2017) are often used to solve the PBE. In the present study, Monte Carlo method is used to obtain the solution of PBE.

Monte Carlo methods are based on artificial realization of the system behavior (Ramkrishna, 2000). Consider a number of particles distributed in

a computational domain with statistically known initial distribution of particle states, the birth and death processes corresponding to the appearance and disappearance of particles in the computational domain are random and satisfying certain probabilities distribution. By artificially generating random variables satisfying the specified probability laws, a “sample path” can be thus constructed. If a large enough number of “sample paths” are constructed, the expected behavior and evolution of the particle population can be obtained by taking the statistical average over all the sample paths. Two routes for the computations of average particle population behavior via Monte Carlo simulation and PBE are shown in Figure 3.1 (Ramkrishna, 2000). More underlying mathematical fundamentals of Monte Carlo methods are presented in Section 3.3.

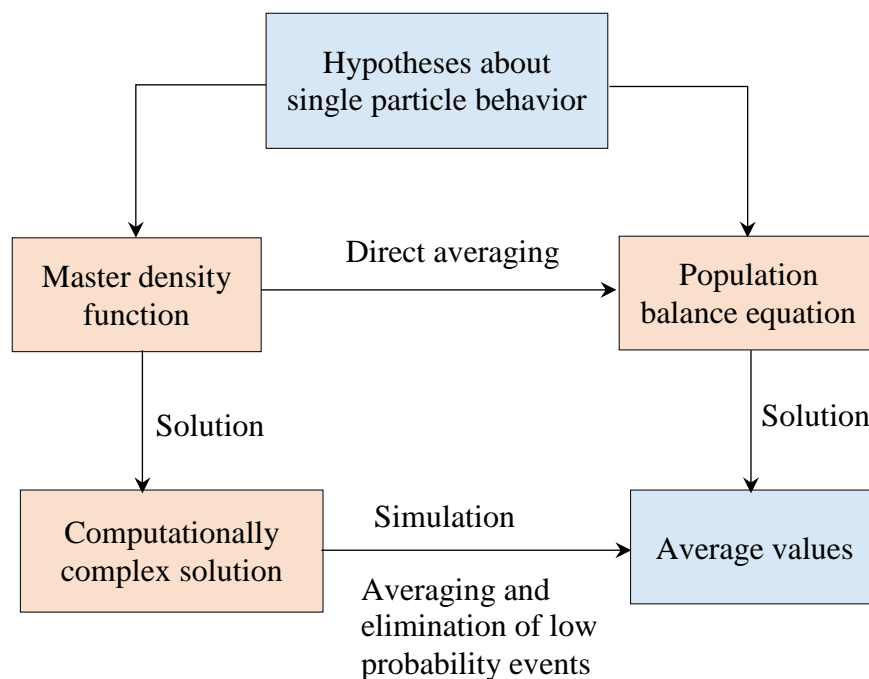


Figure 3.1 Computations of average population behavior via Monte Carlo simulation (left) and PBE (right) (Ramkrishna, 2000).

3.3 Monte Carlo Methods

3.3.1 Overview

Monte Carlo methods are widely used to solve problems with a probabilistic interpretation. According to the law of large numbers (Sznitman and Zerner, 1999), integrals described by the mean value of some random variables can be estimated by taking the empirical average i.e., the mean values of independent samples out of the variables. A Markov Chain Monte Carlo (MCMC) sampler (Hastings, 1970) can be used if the probability distribution of the variables is parameterized. The principal concept is to design a Markov chain model following certain probability law. This distribution can be estimated by the empirical knowledge of Monte Carlo sampler according to the ergodic theorem (Chacon and Ornstein, 1960).

3.3.2 Implementation Procedures

Monte Carlo method is applied to the solution of Boltzmann equation of fluid flow with finite Knudsen number to formulate the DSMC method (Bird, 1994). As mentioned in Chapter 2, the basic idea of DSMC is to use a set of numerical particles to represent the real physical particles. However, only the particle properties of interest such as momentum and mass are tracked. A random generation of collision events is justified by the molecular chaos assumption (Maxwell, 1867) that the velocities of collision particles are independent of position within a homogenous volume. Baxter and Olafsen (2007) reported the first experimental observation of molecular chaos, which proves the assumption of molecular chaos is indeed accurate.

The basic procedures of Monte Carlo methods are as follows (Hesamzadeh et al., 2011):

- Step 1: Define a simulation domain for the possible inputs;
- Step 2: Generate inputs randomly following a specified probability distribution law over the domain;
- Step 3: Perform a deterministic computation on the inputs; and
- Step 4: Aggregate the results.

3.4 Eulerian-Lagrangian Models

3.4.1 Overview

The multi-phase flow models for particulate flows fall into two classes (i.e., Eulerian-Eulerian two-fluid models and Eulerian-Lagrangian fluid-trajectory models), which is subject to the numerical simulation methodology of the discrete phase as shown in Figure 3.2 (Subramaniam, 2013).

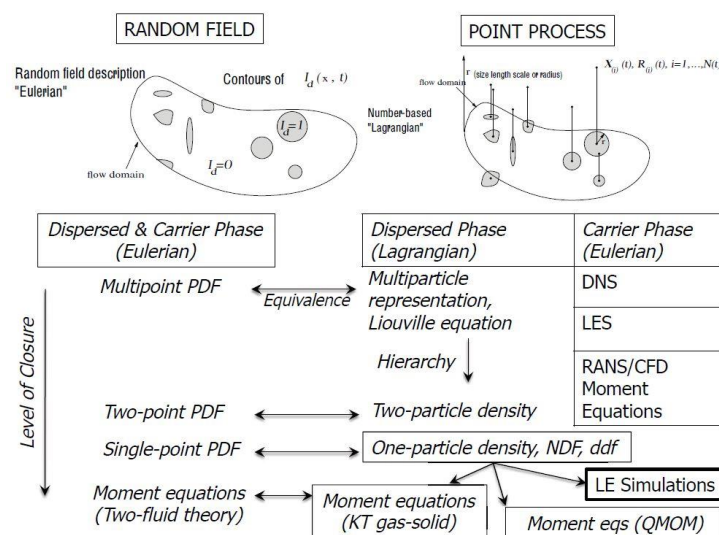


Figure 3.2 Eulerian-Eulerian and Eulerian-Lagrangian multi-phase models under different representations of the discrete phase (Subramaniam, 2013).

The Eulerian-Eulerian models are formulated if the deterministic PBM methods e.g. the sectional method is used to simulate the discrete phase (particulate phase). In the present study, a stochastic PBM-Monte Carlo method is used for the simulation of aerosol dynamics, which is integrated into the Eulerian-Lagrangian models for complex aerosol dynamics in turbulent flows. With the Eulerian-Lagrangian models, the spatiotemporal evolution of particle population can be obtained, which is rarely reported (Zhao and Zheng, 2013).

3.4.2 Interphase Coupling

In the Eulerian-Lagrangian models, the continuous phase is computed in an Eulerian reference frame while the discrete phase is computed in a Lagrangian reference frame (Edge et al., 2011). According to the effect and volume fraction of the discrete phase, the interaction between discrete phase and continuous phase are treated with different ways. For fine particles in a dilute flow at low Reynolds number such as atmospheric aerosols, the effect of particles on the fluid can be neglected and the solution of the Eulerian-Lagrangian models is simplified to track particle trajectories in a flow field which is independent of particles (Kruis et al., 2012; Zucca et al., 2007). Fine particles are airborne particles which are smaller than coarse particles. They have an aerodynamic diameter of $2.5 \mu\text{m}$ or less ($\text{PM}_{2.5}$).

However, the momentum exchange between particles and fluid must be considered if particles have high enough momentum to affect the motion of fluid. Moreover, if the volume fraction of particles in a grid cell is high, the continuity and momentum equations of fluid need to be modified to model the effective viscosity of the particle suspension in the viscous stress term (Patankar and Joseph, 2001).

The mutual coupling between the fluid phase and particulate phase for the inter-particle interactions can be taken into account with the multiphase particle-in-cell (MP-PIC) method (Andrews and O'Rourke, 1996; Snider, 2001). In the MP-PIC method, where the particle phase is treated both as continuous and discrete phases, an accurate mapping from Lagrangian particles is used to associate a particle with a computational grid. While on the grid, the continuum derivative terms that treat the particle phase as a fluid are readily evaluated and then mapped back to individual particles (Andrews and O'Rourke, 1996). For two-way coupling, the particle source in cell (PSI-Cell) method (Crowe et al., 1977) can be used, which regards the particle phase as a source of mass, momentum, and energy to the gaseous phase (Novozhilov et al., 1997).

3.5 Transported PDF Methods for Turbulent Reactive Flows

3.5.1 Overview

Probability density function (PDF) methods have become one of the most promising and powerful approaches for accommodating the effects of turbulent fluctuations in velocity and chemical composition in CFD-based modeling of turbulent reactive flows (Haworth, 2010). Transported PDF methods have also been developed to overcome the closure problems due to interaction between turbulence and particle evolution in turbulent reactive flows by many researchers (Pope, 1981; Pope, 1985; Valino, 1998; Sabel'nikov and Souldard, 2005; Meyer, 2010; Pope and Tirunagari, 2014; Consalvi and Nmira, 2016).

3.5.2 Transport Equations for Turbulent Reactive Flows

The transport equations for constant-density turbulent reactive flows consist of the Navier-Stokes equation for the fluid-phase velocity, U (Bird et al., 2002):

$$\frac{\partial U_i}{\partial t} + U_j \frac{\partial U_j}{\partial x_j} = \nu \frac{\partial^2 U_j}{\partial x_j \partial x_j} - \frac{1}{\rho} \frac{\partial p}{\partial x_i} \quad (3-8)$$

and the transport equation for reacting scalar, ϕ_α (i.e., chemical species concentration or enthalpy):

$$\frac{\partial \phi_\alpha}{\partial t} + U_j \frac{\partial \phi_\alpha}{\partial x_j} = \nu \frac{\partial^2 \phi_\alpha}{\partial x_j \partial x_j} + S(\phi_\alpha) \quad (3-9)$$

where U is the fluid velocity, ν is the kinematic viscosity, ρ is the density, p is the pressure, $S(\phi_\alpha)$ is the source term which accounts for aerosol dynamics and chemical reactions. Equation (3-8) is coupled with Equation (3-9), which forms a complex nonlinear multi-phase system. For reacting scalar turbulent flows, the chemical reaction source term poses novel and difficult closure problems (Fox, 2003), which necessitate the introduction of PDF methods.

3.5.3 Transported PDF Methods

The random velocity field $U_1(x, t)$ for a fixed point in space, \mathbf{x} and a given instant, t can be characterized by a one-point probability density function (PDF) which is defined as follows (Fox, 2003)

$$f_{U_1}(\vec{V}_1; \mathbf{x}, t) d\vec{V}_1 \equiv P\{\vec{V}_1 \leq U_1(\mathbf{x}, t) \leq \vec{V}_1 + d\vec{V}_1\} \quad (3-10)$$

Equation (3-10) can be extended to include any number of random variables or other random variables. The joint velocity and composition PDF is shown in Equation (3-11) and composition PDF is shown in Equation (3-12) (Fox, 2003):

$$f_{U,\psi}(\vec{V}, \psi; \mathbf{x}, t) d\vec{V}_1 d\psi \equiv P\{\vec{V} \leq U(\mathbf{x}, t) \leq \vec{V}_1 + d\vec{V}_1 \cap \psi \leq \phi(\mathbf{x}, t) \leq \psi + d\psi\} \quad (3-11)$$

The joint composition PDF $f_{\psi}(\psi; \mathbf{x}, t)$ can be found by integrating the joint velocity and composition PDF over velocity phase space, as shown in Equation (3-12) (Fox, 2003):

$$f_{\psi}(\psi; \mathbf{x}, t) = \int_{-\infty}^{+\infty} f_{U,\psi}(\vec{V}, \psi; \mathbf{x}, t) d\vec{V} \quad (3-12)$$

Although from the composition PDF approach, all one-point scalar statistics can be computed exactly including chemical source term, the joint velocity and composition PDF approach provides an improved description of the turbulent velocity field and its coupling to the composition fields such as scalar flux and mixing term (Fox, 2003). The transport equation of the composition PDF is shown in Equation (2-17).

3.6 Summary

The theoretical fundamentals of the main ingredients that are used to formulate the proposed CFD-Monte Carlo/PDF method are briefly introduced to present a theoretical framework of the methodology in the present study. The basic concepts, assumptions as well as mathematical theories/governing equations of these ingredients i.e., PBE, Monte Carlo methods, Eulerian-Lagrangian multi-phase models, and transported PDF methods for turbulent reactive flows are presented so that the methodology used in the present study can be more easily reassembled.

Chapter 4 Zero-dimensional Monte Carlo Simulation of Aerosol Dynamics

4.1 Introduction

The purpose of this chapter is to study the complex aerosol dynamic processes by using this newly proposed and developed stochastically weighted operator splitting Monte Carlo (SWOSMC) method. Stochastic weighted particle method and operator splitting method are coupled to formulate the SWOSMC method for the numerical simulation of particle-fluid systems undergoing the complex simultaneous aerosol dynamic processes.

This SWOSMC method is first validated by comparing the numerical simulation results of constant rate coagulation and linear rate condensation with the corresponding analytical solutions. Coagulation and nucleation cases are further studied whose results are compared with the sectional method in excellent agreement. This SWOSMC method has also demonstrated its high numerical simulation capability when used to deal with simultaneous aerosol dynamic processes including coagulation, nucleation and condensation. The comparison between the numerical method used here (SWOSMC method) and the analytical solution is shown in Table 4.1.

Table 4.1 A comparison between the developed SWOSMC method and analytical solutions.

	Advantages	Disadvantages
The analytical solutions	Accurate, stable, simple expression and fully validated by many experimental and numerical simulation results.	Only exist for limited cases; For complex cases, additional assumptions or approximations are needed
The SWOSMC method	Wide applicability to complex cases. Independent of additional assumptions or approximations, high repeatability, low cost.	Not as accurate as analytical solutions or experimental results, requires full validation and repetitions to reduce numerical error.

There always exists conflict and tradeoffs between computational cost (i.e., computational time, computer memory, etc.) and accuracy for Monte Carlo based methods for the numerical simulation of aerosol dynamics. Operator splitting method has been widely used in solving complex partial differential equations while stochastic weighted particle method is commonly used in numerical simulation of aerosol dynamics. However, the integration of these two methods has not been well investigated.

4.2 Numerical Methodology

4.2.1 General Dynamics Equation

The governing equation of the time dependent evolution of particle number density $n(v,t)$ for a single-component aerosol can be written as (Debry et al., 2003):

$$\begin{aligned} \frac{\partial n}{\partial t}(v,t) = & 1/2 \int_{v_0}^{v-v_0} K(u,v-u)n(u,t)n(v-u,t)du \\ & -n(v,t) \int_{v_0}^{\infty} K(u,v)n(u,t)du + \frac{\partial(I_0 n)}{\partial v}(v,t) + \delta(v_0,v)J_0(t) \end{aligned} \quad (4-1)$$

where $K(u,v)$, $I_0(u,v)$ and $J_0(t)$ are the coagulation, condensation and nucleation kernels, respectively.

Compared to the original Smoluchowski's equation which deals only with coagulation, the extended Smoluchowski's equation describes more physical processes which exchange mass between individual particles and the environment such as the fluid in which particles are contained and new particles are also introduced into the particle population (Patterson et al., 2011).

4.2.2 Operator Splitting

For complex aerosol dynamic processes, the terms on the right hand side (RHS) of PBE, i.e., Equation (2-4) may include terms of different physical processes besides coagulation term. Operator splitting is very efficient in solving such complex equation. Instead of integrating all the physical processes simultaneously in one timestep, the operator splitting method divides the integration into multiple steps, as shown in Equations (2-9) to (2-11).

4.2.3 Aerosol Dynamics Kernels

For free molecular regime, the coagulation kernel, $K(u,v)$ can be written as (Zhou et al., 2014):

$$K(u,v) = \left(\frac{6}{\pi}\right)^{\frac{2}{3}} \left(\frac{\pi k_B T_K}{2\rho}\right)^{\frac{1}{2}} \left(\frac{1}{u} + \frac{1}{v}\right)^{\frac{1}{2}} \left(u^{\frac{1}{3}} + v^{\frac{1}{3}}\right)^2 \quad (4-2)$$

where u and v are the volume of the spherical particles; T_K is the temperature, k_B is the Boltzmann's constant and ρ is the density of particles.

In continuous regime, for the size of spherical particles, u and v , the coagulation kernel can be written as (Debry et al., 2003):

$$K(u, v) = 2k_B T_K / 3\mu_{\text{air}} [2 + (v/u)^{1/3} + (u/v)^{1/3}] \quad (4-3)$$

where μ_{air} is the viscosity of air and the other parameters have the same physical meanings as that in Equation (4-2).

The homogeneous nucleation rate can be generally written as (Seinfeld and Pandis, 1998):

$$J_0(t) = C \exp(-\Delta G^* / k_B T) \quad (4-4)$$

where ΔG^* is the free energy that is required to form a stable nucleus and C is a constant which is related to vapor pressure.

As condensation/evaporation process involves the relaxation to an equilibrium state between aerosol and gas phases for one chemical species (Debry et al., 2003), the kernels are thus proportional to the pressure difference between the bulk gas and the equilibrium pressure:

$$I_0(v, t) = C_I \exp(p_i^\infty - p_i^{eq}) \quad (4-5)$$

where C_I is a constant which is related to the diffusion species and temperature, p_i^∞ and p_i^{eq} are the vapor pressure and the equilibrium vapor pressure of species, i from the particle, respectively.

4.2.4 Non-dimensionalization

The GDE Equation (4-1) is non-dimensionalized based on the relative mass density, $\tilde{q}(v,t)$ of aerosol particles (Debry et al., 2003) which can be expressed as Equation (4-6):

$$\tilde{q}(v,t) = \frac{q(v,t)}{Q_0}, \quad Q_0 = \int_0^{\infty} q_0(v)dv \quad (4-6)$$

where $q(v,t)$ is the mass density of aerosol particles and Q_0 is the total initial mass of aerosol particles.

Substituting $n(v,t)$ into Equation (4-1) with $\tilde{q}(v,t)$, it can be expressed as (Debry et al., 2003):

$$\begin{aligned} \frac{\partial \tilde{q}}{\partial t}(v,t) = & 1/2 \int_{v_0}^{v-v_0} Q_0 \frac{K(u, v-u)}{v-u} \tilde{q}(u,t) \tilde{q}(v-u,t) du \\ & - \tilde{q}(v,t) \int_{v_0}^{\infty} Q_0 \frac{K(u, v)}{u} \tilde{q}(u,t) du + \frac{I_0(v,t) \tilde{q}(v,t)}{v} \\ & - \frac{\partial(I_0 \tilde{q})}{\partial v}(v,t) + \frac{v_0 J_0(t)}{Q_0} \delta(v_0, v) \end{aligned} \quad (4-7)$$

4.2.5 Algorithm Formulation

The main idea of the present method is to introduce stochastic weights to various numerical particles according to the mass change caused by different aerosol dynamic processes in order to increase the numerical stability of Monte Carlo method. Operator splitting technique is used to treat stochastic process (i.e., coagulation) and deterministic processes (i.e., condensation, nucleation etc.) separately with corresponding methods to reduce computational time for the simulation of complex aerosol dynamics. The idea of using numerical particles

with varying mass weights (Debry et al., 2003) is adopted herein, where the i -th numerical particle is associated with a varying mass weight, $w_i(t)$ of real aerosol particle of size, $y_i(t)$, thus the i -th numerical particle now stands for a number of $w_i(t)/y_i(t)$ of real aerosol particles.

The introduction of such a varying mass weight to numerical particles in stochastic simulation of simultaneous aerosol dynamic processes is necessary and well justified. When mass weights are adhered to numerical particles (i.e., numerical particles are connected with a certain mass of real aerosols), the total number of numerical particles remains constant and no re-sampling is needed for coagulation process (Eibeck and Wagner, 2001). This is because the total mass of real aerosol particles remains constant in coagulation process although the total number of real aerosol particles decreases.

If the numerical particles are directly connected with the number of real aerosol particles and no further up sampling (adding new particles to the particle-fluid system) is conducted, the decreasing number of numerical particles may cause severe numerical diffusion as coagulation converges on an infinite number of numerical particles. However, for some other aerosol dynamic processes including nucleation, condensation, evaporation, deposition and removal, the total mass of aerosol particles in the particle-fluid system actually varies with time. By introducing varying mass weights to numerical particles, the weights, $w_i(t)$ will evolve with time for mass-varying process such as condensation and evaporation. In here, nucleation is conducted by creating a certain mass of new particles according to nucleation rate which is independent of pre-existing particles. The integration

details for an individual process will be presented in Section 4.3.2. The main algorithm of stochastically weighted operator splitting Monte Carlo (SWOSMC) method over a time period $[0, T]$ is presented as follows:

Initialization: setting of the following quantities:

$$[(y_i^0, w_i^0), i = 1, 2, \dots, N_0],$$

Operator splitting over time loop $[0, T]$:

Integration of Equation (4-7) from t_k to $t_{k+1} = t_k + \tau_k$, where τ_k is the time step determined previously:

- (i) Integration of coagulation based on Monte Carlo based methods (Gillespie, 1972);
- (ii) Integration of condensation using an ODE solver from Zhou et al., (2014);
- (iii) Integration of nucleation: creation of new particles, J ; and
- (iv) Updating the particle-fluid system and when $t > T$, stop the simulation and take average over the results.

4.3 Numerical Setup

4.3.1 Time Step Determination

According to Debry et al., (2003), the time scales for different physical processes can be calculated as Equations (4-8) to (4-10) in order to allow an accurate integration result as well as avoid too much computational time:

For coagulation of aerosols, y_i^k, y_j^k :

$$\Delta t_{\text{coag}} = \frac{y_j^k}{Q_0 w_j^k K(y_i^k, y_j^k)} \quad (4-8)$$

For condensation/evaporation of aerosols, y_j^k ,

$$\Delta t_{\text{cond/evap}} = \frac{y_j^k}{I_0(y_i^k, t_k)} \quad (4-9)$$

For nucleation of aerosols:

$$\Delta t_{\text{nucl}} = \frac{Q_0}{v_0 J_0(t)} \quad (4-10)$$

To ensure an accurate integration, the time step should be less than the minimum of all the time scales (Zhao et al., 2005) from Equations (4-8) to (4-10) which is set as the minimum time step.

4.3.2 Integration Details

The system state after a time step is calculated by integrating over a time step. Noting that a varying mass weight is used, only condensation/evaporation processes that cause the mass change to the particle-fluid system will have numerical particles with varying weights.

For integration of coagulation, the collision criterion should be met. The volume of particle i after a splitting time step becomes the total volume of particle i and its collision partner, while the weight of i -th numerical particle remains

unchanged. For the i -th numerical particle at k -th time step, the integration procedure is written as:

$$y_i^{k+1/2} = y_i^k + y_{j_i}^k, \text{ if } r \leq \frac{Q_0 w_{j_i}^k K(y_i^k, y_{j_i}^k)}{y_{j_i}^k} \tau_k \quad (4-11a)$$

$$\tau_k = \min\left(\frac{y_{j_i}^k}{Q_0 w_{j_i}^k K(y_i^k, y_{j_i}^k)}\right) c \quad (4-11b)$$

where $y_i^{k+1/2}$, y_i^k , $y_{j_i}^k$ are the volume size after the collision step, the volume of i -th particle and the volume collided with i -th particle at k -th time step, respectively. For the criterion part, r is a random number uniformly distributed over $[0, 1]$, τ_k is the defined time step based on the minimum coagulation time scale and is also defined as the collision probability is within $[0, 1]$, c is a constant which is usually

$\frac{Q_0 w_{j_i}^k K(y_i^k, y_{j_i}^k)}{y_{j_i}^k} \tau_k$ equal to 0.1 (Debry et al., 2003).

For integration of condensation, it is performed via integration using a self-adaptive fifth-order Runge-Kutta method (Zhou et al., 2014) over the splitting time step of varying weight function, which is determined by the mechanistic rate of condensation. For the i -th numerical particle at k -th time step, the results obtained from the above coagulation step are used as input for this step, the integration procedure is written as:

$$\frac{dy_i}{dt} = I_0(y_i, t), \quad \frac{dw_i}{dt} = w_i \frac{I_0(y_i, t)}{y_i} \quad (4-12a)$$

$$y_i^{k+1} = y_i^{k+1/2} + \Delta t I_0(y_i^{k+1/2}, t_k), \quad w_i^{k+1} = w_i^{k+1/2} \frac{y_i^{k+1}}{y_i^{k+1/2}} \quad (4-12b)$$

where $y_i^{k+1/2}$, y_i^{k+1} are the volume size, $w_i^{k+1/2}$, w_i^{k+1} are the weights, $I_0(y_i^{k+1/2}, t_k)$ and $I_0(y_i, t)$ are the condensation rates after the condensation step and that obtained

from the previous coagulation step for the i -th particle and the k -th time step, respectively. Δt is the integration time step.

For integration of nucleation, only a certain mass of new particles with the minimum nucleus volume, v_0 are created and added to the particle-fluid system. For the i -th newly created particle, it is defined as:

$$y_i^{k+1} = v_0, w_i = 1, m_c = v_0 J_0(t_k) \Delta t \quad (4-13)$$

where y_i^{k+1} is the volume size of the i -th newly created particle, w_i is the weight of the i -th newly created particle, $J_0(t_k)$ is the nucleation rate mass of of the i -th newly created particle, m_c is the total mass of all the newly created particles within one time step and v_0 is the initial volume size of the newly created particles.

4.3.3 Initial Conditions and Cases with Analytical Solutions

4.3.3.1 Initial Conditions

The initial particle number density is $1.0 \times 10^{18} / \text{m}^3$ and initial particle diameter is set as 1.24 nm for Case 1 (constant rate coagulation and linear rate condensation case) and Case 2 (constant rate coagulation and nucleation) so that the following simple dimensionless expressions for moments can be obtained. The initial conditions of the other cases in the present study can be found in Frenklach and Harris (1987). All the studied cases in the present study are listed in Table 4.2. These cases are selected to represent the typical aerosol dynamic processes taking place in the actual particle-fluid systems such as particulate emission from vehicles and industrial boilers, aerosol formation, colloidal solution, etc. These studied cases are so arranged that the complexity of numerical simulation cases increases from

Case 1 to Case 4, which is used for the evaluation of computational accuracy and efficiency of this newly proposed SWOSMC method (Liu and Chan, 2017).

Table 4.2 Summary of the studied cases (Liu and Chan, 2017).

Cases	Description
Case 1	Constant rate coagulation and linear rate condensation for validation with analytical solution. (The free molecular regime coagulation is only shown as a part of Case 1.)
Case 2	Constant rate coagulation and constant rate nucleation.
Case 3	Free molecular regime coagulation and constant rate nucleation.
Case 4	Simultaneous aerosol dynamic processes including coagulation, nucleation and condensation.

4.3.3.2 Constant Rate Coagulation and Linear Rate Condensation

Analytical solutions to the GDE Equation (4-1) is only available for very limited cases, among which the case of constant rate coagulation and linear rate condensation is selected for the first validation case. For constant rate coagulation and linear rate condensation, when the coagulation and condensation kernel are both set as unity for simplicity, the particle number density $n(v,t)$ and the dimensionless zeroth order moment, M_0 and first order moments, M_1 with respect to the particle volume can be derived as (Ramabhadran et al., 1976):

$$n(v,t) = \frac{(M_0(t))^2}{M_1(t)} \exp\left(-\frac{M_0(t)}{M_1(t)} v\right) \quad (4-14a)$$

$$M_0(t) = \frac{2}{2+t} \quad (4-14b)$$

$$M_1(t) = \exp(t) \quad (4-14c)$$

4.3.3.3 Constant Rate Coagulation and Nucleation

If both coagulation and nucleation rates are constant (i.e., both are set as unity for simplicity in the present study), an analytical solution is available to Equation (4-1). The analytical solutions of relative particle number density and relative particle volume concentration can be expressed as (Maisels et al., 2004):

$$\frac{N}{N_0} = B \frac{1 + B \tanh(\tau_0/2)}{B + \tanh(\tau_0/2)} \quad (4-15)$$

$$\frac{V}{V_0} = 1 + \frac{B}{2} \tau_0 \quad (4-16)$$

where V and V_0 are the total volume of particles at time, t and at initial time, t_0 , respectively. N and N_0 are the number density of particles at time, t and at initial time, t_0 respectively. B , E (in Equation (4-17)) and τ_0 are dimensionless parameters determined by the initial conditions and the detailed expressions can be found in Maisels et al. (2004).

4.3.3.4 Simultaneous Coagulation, Nucleation and Condensation

For simultaneous aerosol dynamic processes, if the nucleation, coagulation, condensation rates and monomer concentration are constant, the analytical solution to these simultaneous processes including coagulation, nucleation and condensation exists (Maisels et al., 2004). The analytical expression of relative particle number density is given in Equation (4-15) since condensation involves no change in the particle number. The analytical expression of the relative particle volume concentration for simultaneous coagulation, nucleation and condensation is written as:

$$\frac{V}{V_0} = 1 + \left[\left(\frac{B}{2} + E \right) \tau_0 + 2E \ln \left(\frac{1 + \exp(-\tau_0)}{2} + \frac{1 - \exp(-\tau_0)}{2B} \right) \right] \quad (4-17)$$

where all the parameters in Equation (4-17) have the same physical meanings with those in Equations (4-15) and (4-16). More information of this case study can be found in Liu et al. (2015).

4.3.4 Calculation of Maximum Relative Error

The maximum relative error used to evaluate the numerical simulation results is defined as:

$$\varepsilon_{\max} = \left\{ \sqrt{[(X(t) - X_0(t))/X_0(t)]^2} \right\}_{\max} \quad (4-18)$$

where ε_{\max} is the maximum relative error, $X(t)$ is the numerical simulation results obtained with this newly proposed SWOSMC method, and $X_0(t)$ is the reference value for comparison.

4.4 Results and discussion

4.4.1 Initial Validation

This newly proposed SWOSMC method (Liu and Chan, 2017) is first validated for constant rate coagulation and linear rate condensation processes. The dimensionless zeroth order moment, M_0 which is proportional to the number density of particles, is shown in Figure 4.1. An increasing number of numerical particles are used for the numerical simulation. It can be seen that the numerical simulation results agree well with the analytical solution when only 1000 numerical

particles are used, which shows the good capability of the SWOSMC method in dealing with simultaneous coagulation and condensation processes.

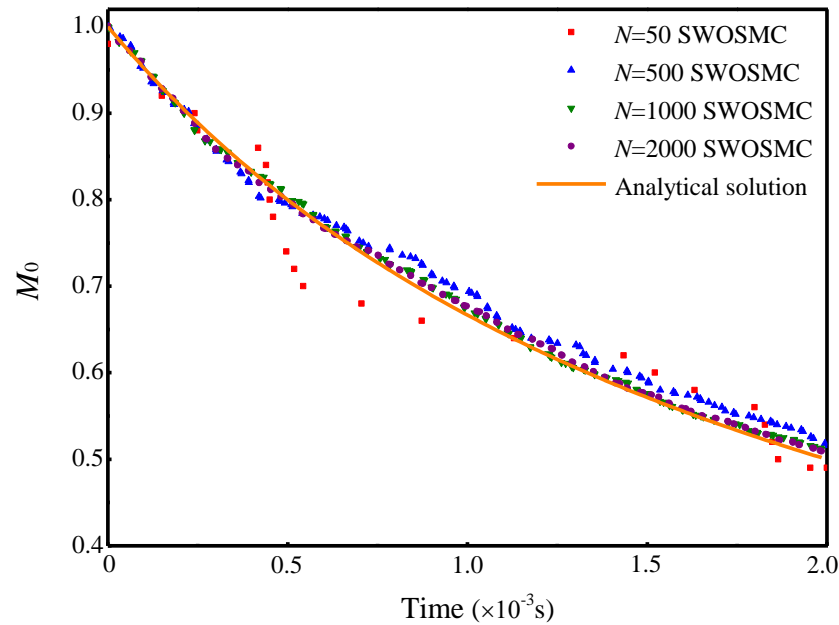


Figure 4.1 Zeroth order moment, M_0 under coagulation and condensation processes for SWOSMC (Liu and Chan, 2017) versus the analytical solution (Ramabhadran et al., 1976) where N is the number of numerical particles used in each simulation run.

An excellent agreement between the dimensionless first order moment, M_1 obtained by the SWOSMC method and analytical solution is also observed in Figure 4.2. The exponentially increasing M_1 with respect to simulation time represents the rapid increase of the total volume of particles in the numerical simulation particle-fluid system due to condensation.

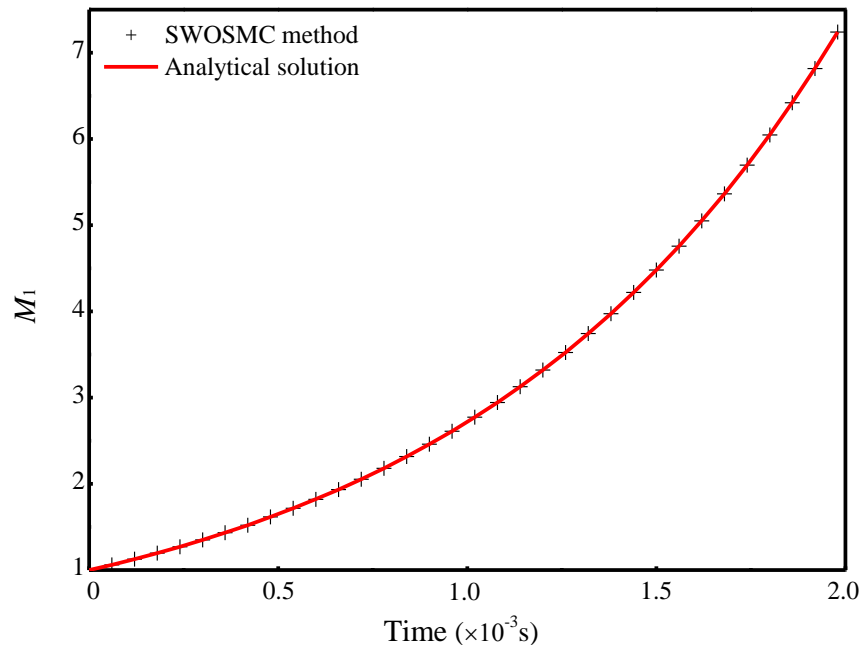


Figure 4.2 First order moment, M_1 under coagulation and condensation processes for SWOSMC (Liu and Chan, 2017) versus the analytical solution (Ramabhadran et al., 1976) where the number of numerical particles, N used in each simulation run is 1000.

Figure 4.3 shows another application of the SWOSMC method to free molecular regime coagulation and the numerical simulation results is validated by comparing to the sectional method (Prakash et al., 2003). Excellent agreement can be also observed between the particle number density obtained by these two methods with the maximum relative error (by taking the sectional method as reference) of less than 1% during the whole simulation time.

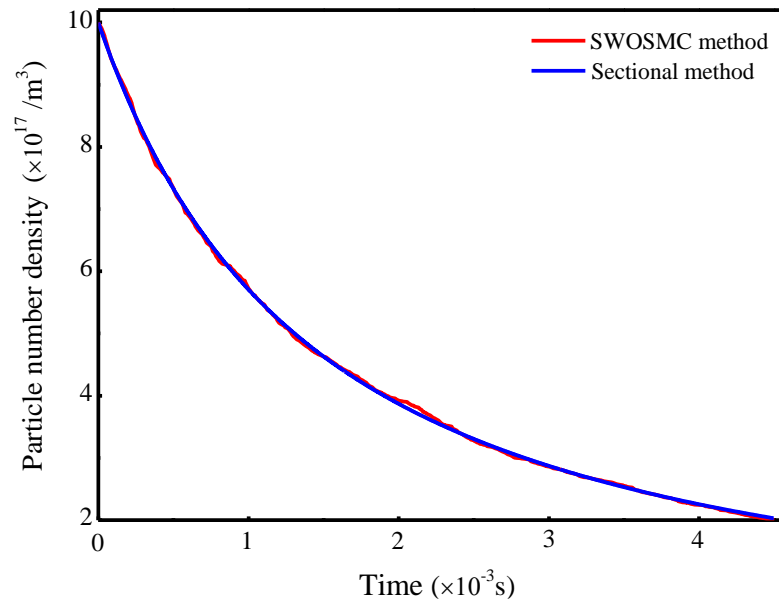


Figure 4.3 Particle number density under free molecular regime coagulation for SWOSMC (Liu and Chan, 2017) versus the sectional method (Prakash et al., 2003) where the number of numerical particles, N used in each simulation run is 1000.

4.4.2 Constant Rate Coagulation and Nucleation

For constant rate coagulation and nucleation, an increasing number of numerical particles are used in the SWOSMC method. Figure 4.4 shows the relative particle number density, N/N_0 obtained via the SWOSMC method and the analytical solution (Maisels et al., 2004), respectively. It can be seen that the SWOSMC method agrees well with the analytical solution with increased number of numerical particles. The increasing relative particle number density implies the nucleation is dominant within the simulation time. As the simulation proceeds, some statistical fluctuations can be observed, but the maximum relative error compared with the analytical solution remains less than 2% during the whole simulation time, which also proves the reliability of this newly proposed SWOSMC method (Liu and Chan, 2017).

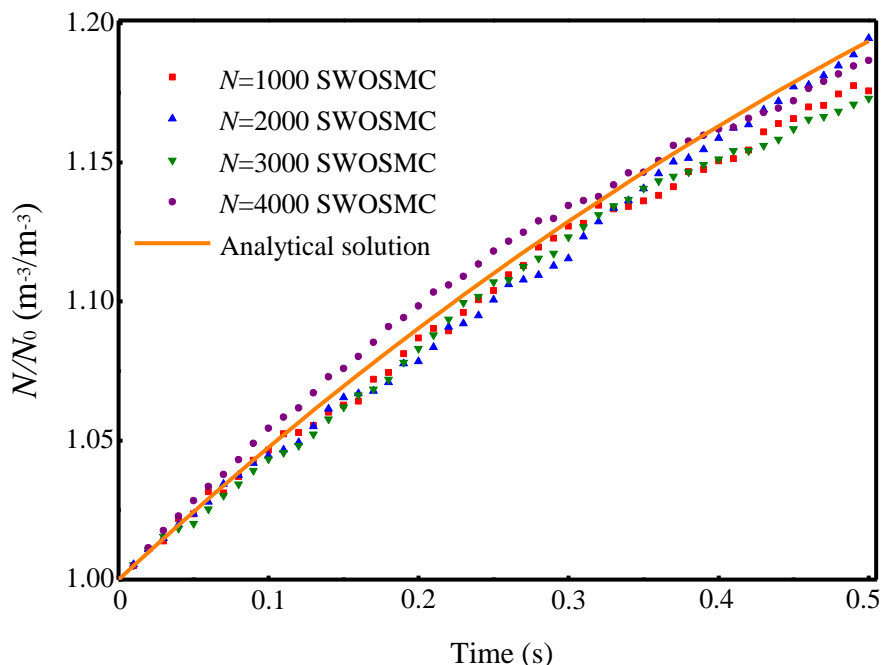


Figure 4.4 Relative particle number density, N/N_0 under constant rate coagulation and nucleation processes for SWOSMC (Liu and Chan, 2017) versus the analytical solution (Maisels et al., 2004) where N is the number of numerical particles used in each simulation run.

The relative particle volume concentration, V/V_0 under the constant rate coagulation and nucleation is shown in Figure 4.5. The agreement between the SWOSMC method and the analytical solution is so excellent that even for using 1000 numerical particles, the maximum relative error is less than 1%. The linear increase in relative particle volume concentration can be well explained by the constant rate nucleation that continuously creates new particles in the particle-fluid system. This SWOSMC method has demonstrated the ability to reach a high accuracy of numerical simulation with acceptable number of numerical particles.

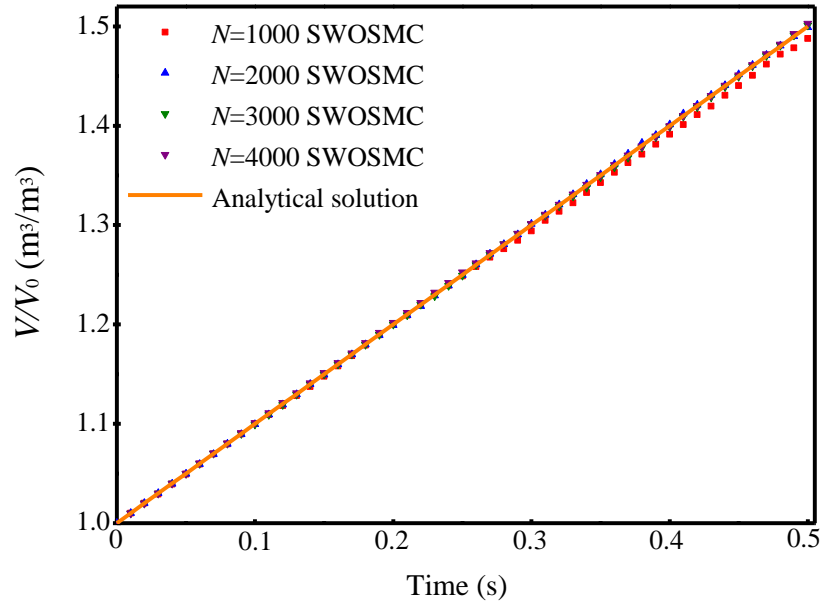


Figure 4.5 Relative particle volume concentration, V/V_0 under constant rate coagulation and nucleation processes for SWOSMC (Liu and Chan, 2017) versus the analytical solution (Maisels et al., 2004) where N is the number of numerical particles used in each simulation run.

4.4.3 Free Molecular Regime Coagulation and Constant Rate Nucleation

Figure 4.6 shows the evolution history of particle number density of simultaneous free molecular regime coagulation and constant rate nucleation obtained via the SWOSMC method (Liu and Chan, 2017) and the sectional method (Prakash et al., 2003). A very satisfactory agreement can be found between the two methods for even 100 numerical particles used for the SWOSMC method, which demonstrates the good applicability and computational efficiency of this SWOSMC method in solving simultaneous free molecular regime coagulation and constant nucleation problem. As the number of numerical particles increases from 100 to 2000, the maximum relative error between these two methods remains basically the same, which implies that 100 numerical particles is already enough to reach very good agreement compared with the sectional method. Some fluctuations can be found for numerical simulation with different number of numerical particles

e.g. the simulation results with 500 numerical particles are closer to the results via the sectional method than that using 1000 particles at the initial stage of simulation, specifically before 2×10^{-3} s. This may be explained by the statistical fluctuations of the particle-fluid system at the initial stage. Similar fluctuations can also be found in Figure 4.7.

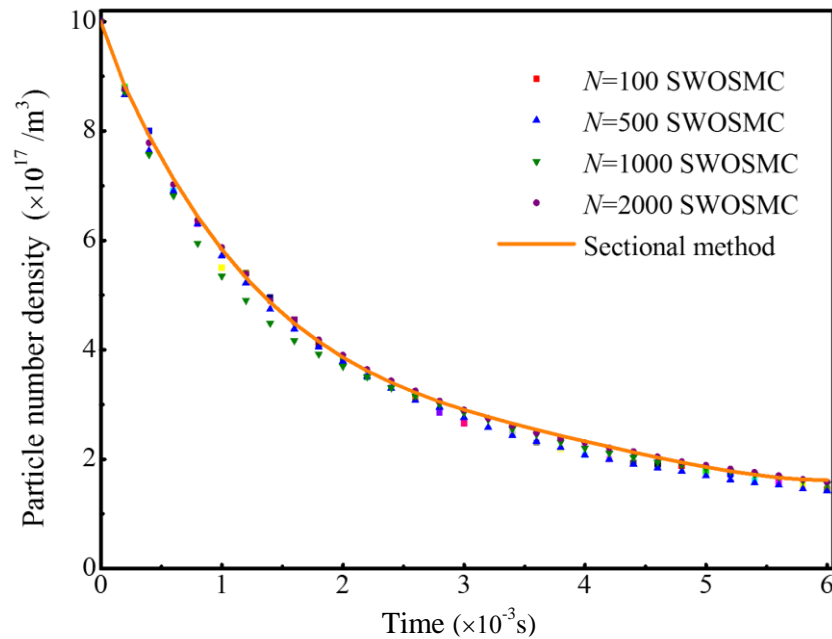


Figure 4.6 Particle number density under free molecular regime coagulation and constant rate nucleation for SWOSMC (Liu and Chan, 2017) versus the sectional method (Prakash et al., 2003) where N is the number of numerical particles used in each simulation run.

The evolution history of number average diameters of particles, d_{ave} is tracked and shown in Figure 4.7. An increasing number of numerical particles from 100 to 2000 are used in the SWOSMC simulation. The number average diameter of particles shows good agreement between the SWOSMC and the sectional methods. A rapid increase of the average particle diameter is observed due to nucleation and coagulation. With the increase of the number of numerical particles, the maximum

relative error between these two methods significantly decreases, reaching far less than 1% when only 500 numerical particles are used.

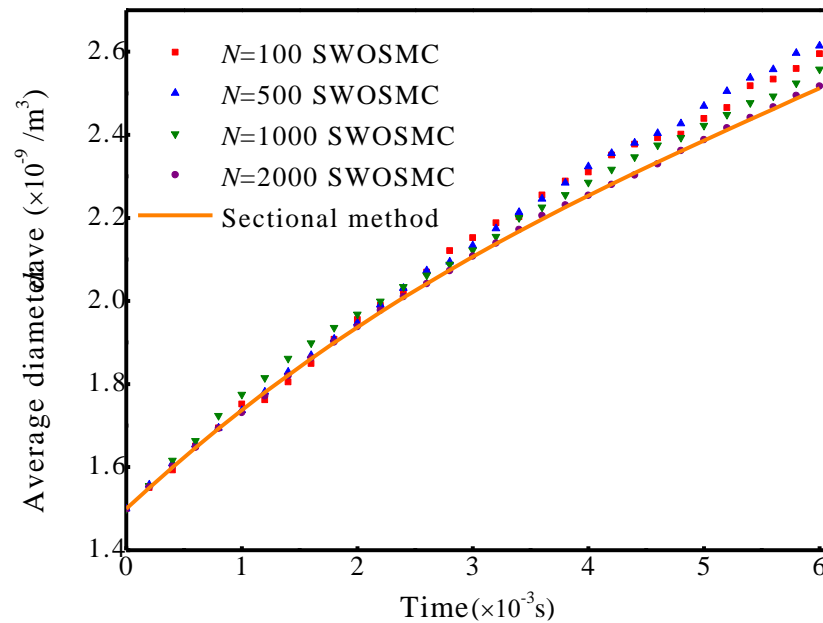


Figure 4.7 Average diameter of the numerical particles, d_{ave} under free molecular regime coagulation and constant rate nucleation via SWOSMC (Liu and Chan, 2017) versus the sectional method (Prakash et al., 2003) where N is the number of numerical particles used in each simulation run.

The second order moment, M_2 with respect to the particle size distribution (PSD) is shown in Figure 4.8. As particles are continually created by nucleation process, the second order moment shows rapid increase once the nucleation process begins. With the increase of the number of numerical particles, the maximum relative error relative to the sectional method (Prakash et al., 2003) decreases rapidly to less than 1% when only 500 numerical particles are used. However, no significant improvement is achieved with the number of numerical particles increasing from 500 to 2000. It shows that 500 numerical particles are good enough to obtain as high computational accuracy as that via the sectional method (Prakash et al., 2003). It can be seen from Figure 4.8 that the newly proposed SWOSMC method

(Liu and Chan, 2017) is highly promising to capture the evolution of high-order moments with a relatively low computational cost (i.e., computational time, computer memory etc.).

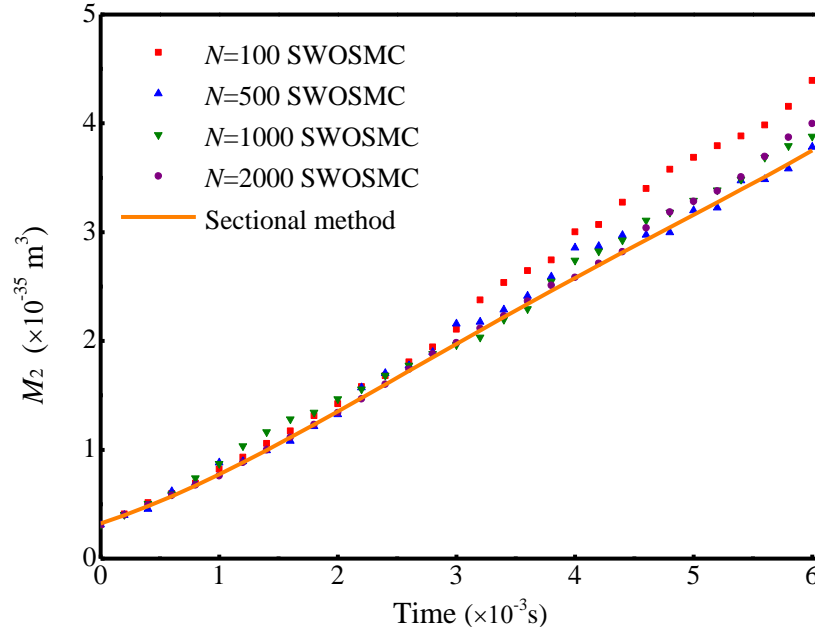


Figure 4.8 Second order moment, M_2 of the particles under free molecular regime coagulation and constant rate nucleation processes for SWOSMC (Liu and Chan, 2017) versus the sectional method (Prakash et al., 2003) where N is the number of numerical particles used in each simulation run).

4.4.4 Simultaneous coagulation, nucleation and condensation processes

As this case is much more complex than the other studied cases, the number of numerical particles used in this case is 4000 so as to obtain the satisfactory computational accuracy. The particle volume concentration, V/V_0 of simultaneous aerosol dynamic processes is shown in Figure 4.9 and is validated with the analytical solution obtained from Maisels et al., (2004). Coagulation, nucleation and condensation processes are simulated simultaneously. It can be seen that the numerical simulation results fit very well with the analytical solution for the selected case. The particle volume concentration increases linearly with the dimensionless

time, which is also consistent with the theoretical expression given in Equation (4-17). As the simulation time is very short, the nonlinear term in the theoretical expression in Equation (4-17) can be neglected, which yields a linear relationship between the particle volume concentration and dimensionless time, as shown in Figure 4.9.

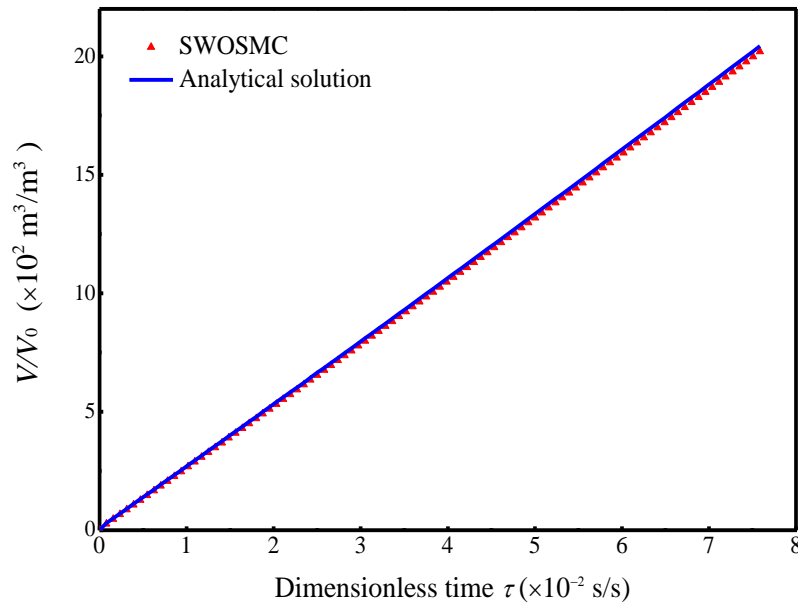


Figure 4.9 Particle volume concentration, V/V_0 under simultaneous aerosol dynamic processes for SWOSMC (Liu and Chan, 2017) versus the analytical solution (Maisels et al., 2004) where the number of numerical particles, N used in each simulation run is 4000.

The particle number density, N/N_0 of this simultaneous aerosol dynamic processes is shown in Figure 4.10. For the reason of short simulation time, the theoretical expression in Equation (4-15) also approximates a linear relationship between the particle number density and the dimensionless time. However, even with small simulation time and only 4000 numerical particles, the results obtained via the SWOSMC method agree well with the analytical solution, which shows the

high potential of this newly proposed SWOSMC method in solving simultaneous full processes in complex aerosol dynamics.

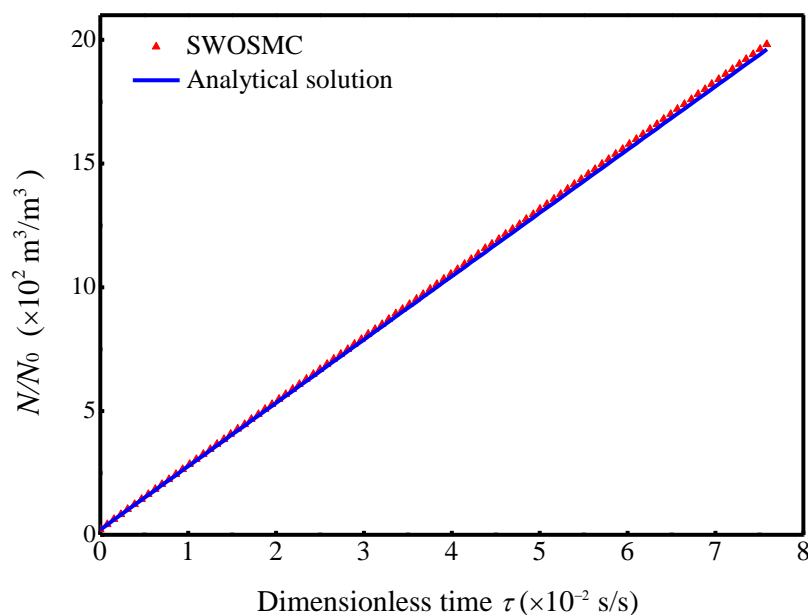


Figure 4.10 Particle number concentration, N/N_0 under simultaneous aerosol dynamic processes for SWOSMC (Liu and Chan, 2017) versus the analytical solution (Maisels et al., 2004) where the number of numerical particles, N used in each simulation run is 4000.

4.4.5 Parametric analysis of the studied cases

The main simulation parameters are presented in Table 4.3 for evaluation purpose of this newly proposed and developed SWOSMC method (Liu and Chan, 2017). It can be seen that with the increase of the complexity from Case 1 to Case 4, an increasing computational time is needed for a fixed number of numerical particles. However, for a certain case, the computational error is inversely proportional to the square root of the total number of the numerical particles (Oran et al., 1998). It also suggests that further optimization of this new SWOSMC method is needed in order to improve the computational efficiency and accuracy for the complex particle-fluid systems. Compared with the sectional method

(Prakash et al., 2003), the SWOSMC method takes shorter simulation time even with the largest number of numerical particles in Case 3. This new SWOSMC method has demonstrated its capability to obtain higher computational accuracy with shorter simulation time than the sectional method for the same case.

Table 4.3 Analysis of main numerical simulation parameters (Liu and Chan, 2017).

Cases	Number of numerical particles	Normalized computational time	Maximum relative error (%)
Case 1	50	1	11
	500	3	5
	1000	5	2
	2000	7.5	<1
Case 2	1000	5	3.7
	2000	7	3
	3000	9	2
	4000	11	<1
Case 3	100	1.5	6.5
	500	4	5.3
	1000	6	<1
	2000	9	<1
	Sectional method	>100	N/A
Case 4	4000	45	<1

Note: Cases 1, 2 and 3 are evaluated by the simulation results of zeroth order moment, M_0 while the particle number concentration is considered for Case 4. The maximum relative error is calculated according to Equation (4-18). Computational time is normalized based on the ratio of any computational time to the shortest computational time (i.e., the computational time of Case 1 with 50 numerical particles) in the present study.

4.5 Summary

The simulation results of this newly proposed and developed stochastically weighted operator splitting Monte Carlo (SWOSMC) method (Liu and Chan, 2017) are fully validated with corresponding analytical solution (Maisels et al., 2004) and the sectional method (Prakash et al., 2003) for various aerosol dynamic processes (i.e., coagulation, condensation and nucleation) in different flow regimes. This validated SWOSMC method also offers higher capacity of numerical simulation for solving simultaneous aerosol dynamic processes occurring in complex particle-fluid systems. Further development of this new method will be presented in the study of multi-dimensional and inhomogeneous aerosol dynamic processes of turbulent particle-fluid systems in Chapter 5.

Chapter 5 **CFD-PBM Simulation of Aerosol Dynamics in Turbulent Flows**

5.1 **Introduction**

A computational fluid dynamics (CFD) coupling with a Monte Carlo (CFD-Monte Carlo) method is presented to simulate complex aerosol dynamics in turbulent flows. A Lagrangian particle method based probability density function (PDF) transport equation is formulated to solve the population balance equation (PBE) of aerosol particles. The formulated CFD-Monte Carlo method allows investigating the interaction between turbulence and aerosol dynamics and incorporating individual aerosol dynamic kernels as well as obtaining full particle size distribution (PSD). Several typical cases of aerosol dynamic processes including turbulent coagulation, nucleation and growth are studied and compared to the sectional method with excellent agreement. Coagulation in both laminar and turbulent flows is simulated and compared to demonstrate the effect of turbulence on aerosol dynamics. The effect of jet Reynolds (Re_j) number on aerosol dynamics in turbulent flows is fully investigated for each of the studied cases. The results demonstrate that Re_j has significant impact on a single aerosol dynamic process (e.g. coagulation) and the competitive and simultaneous aerosol dynamic processes in turbulent flows. This newly proposed and validated CFD-Monte Carlo/PDF method renders an efficient method for simulating complex aerosol dynamics in turbulent flows and provides a better insight into the interaction between turbulence and the full PSD of aerosol particles. The novelty of the present study is to investigate the effect of Re_j number on the PSD of typical aerosol dynamic processes in turbulent flows. The enhancing effect of turbulence on aerosol dynamic

processes as well as the competition and transition between different aerosol dynamic processes are proved and analyzed. A new particle tracking method with high computational efficiency is adopted in the Monte Carlo simulation. Moreover, the operator splitting technique recently proposed by Liu and Chan (2017) for solving simultaneous aerosol dynamic processes is also used to increase the computational efficiency and accuracy.

5.2 Numerical Methodology

5.2.1 Governing Equations of Aerosol Dynamics in Turbulent Flows

The governing equations of the coupled fluid dynamics-aerosol dynamics in turbulent flows include the PBE in terms of particle number density (i.e., Equation (1-1)) as well as continuity, momentum equations (i.e., Navier-Stokes equations) and energy equation, which are written as:

$$\nabla \cdot \mathbf{u}(\mathbf{x}, t) = 0 \quad (5-1)$$

$$\frac{\partial \mathbf{u}(\mathbf{x}, t)}{\partial t} + (\mathbf{u}(\mathbf{x}, t) \cdot \nabla) \mathbf{u}(\mathbf{x}, t) = \nu_k \nabla^2 \mathbf{u}(\mathbf{x}, t) - \nabla P(\mathbf{x}, t) \cdot \nabla / \rho \quad (5-2a)$$

$$\frac{\partial T(\mathbf{x}, t)}{\partial t} + (\mathbf{u}(\mathbf{x}, t) \cdot \nabla) T = k_e \nabla^2 T(\mathbf{x}, t) + H / \rho c_p \quad (5-2b)$$

where \mathbf{u} is the velocity of the carrier fluid phase, ν_k is the kinematic viscosity, which is assumed constant, \mathbf{x} is the coordinates of particles, P is the pressure, ρ is the fluid density, k_e is the heat conductivity, H is the source of energy and c_p is the specific heat capacity, T is temperature. An in-house time dependent Reynolds-Averaged Navier Stokes (RANS) code and k - ε turbulence model (also used in the transported PDF method of Akridis and Rigopoulos (2015)) are used together with the following transported PDF method.

The CFD code is discretized with a finite volume scheme. The averaged momentum and k - ε equations are solved in a two-dimensional axisymmetric domain. The mean velocity field and the turbulence time scale are applied to the scalar PDF by the CFD code while the micro mixing term is obtained via the estimation of ensemble mean scalars in each computational cell of the computational grid. In order to reduce statistical error, a time-averaging method is further used. The following equations show the k - ε turbulence model in Cartesian tensor notation form and repeated indices mean summation (Akridis and Rigopoulos, 2015):

$$\frac{\partial}{\partial t} [\bar{\rho}k] + \frac{\partial}{\partial x_j} [\bar{\rho}\tilde{u}_j k] = \frac{\partial}{\partial x_j} \left[\left(\mu + \frac{\mu_t}{\sigma_k} \right) \frac{\partial k}{\partial x_j} \right] + G - \bar{\rho}\varepsilon \quad (5-3)$$

$$\frac{\partial}{\partial t} [\bar{\rho}\varepsilon] + \frac{\partial}{\partial x_j} [\bar{\rho}\tilde{u}_j \varepsilon] = \frac{\partial}{\partial x_j} \left[\left(\mu + \frac{\mu_t}{\sigma_\varepsilon} \right) \frac{\partial \varepsilon}{\partial x_j} \right] + \frac{\varepsilon}{k} [C_{\varepsilon 1} G - C_{\varepsilon 2} \bar{\rho}\varepsilon] \quad (5-4)$$

where Reynolds averaged quantities are shown with a bar on top while Favre averaged quantities are shown with a tilde on top. ρ is the mixture density, μ is the molecular viscosity of the mixture, μ_t is the turbulent viscosity, σ is the turbulent Prandtl number and G is the generation rate of turbulent kinetic energy.

Estimates of mean quantities in PDF/Monte-Carlo simulation are obtained by means of a particle-cloud-in-cell method and the Favre average of a quantity, Q in a cell, c is shown as follows (Mehta, 2008):

$$\tilde{Q}_c = \frac{\sum_{p \in c} m_p Q_p}{\sum_{p \in c} m_p} \quad (5-5)$$

where m_p is the mass of particle, p and Q_p is the quantity carried by particle, p in a cell, c . The summation is carried out over all the particles in cell, c .

The PBE in terms of particle number density, $n(v, x, t)$, a function of particle volume as well as of space coordinates and time, can be written as Equation (5-6), in which $n(v, x, t)$ is written as $n(v)$ for simplicity:

$$\begin{aligned} & \frac{\partial n(v)}{\partial t} + \nabla(u \cdot n(v)) + \frac{\partial(G(Y_1, Y_2, \dots, Y_m, v))}{\partial v} \cdot n(v) \\ & = D_p \nabla^2 n(v) + B_n(Y_1, Y_2, \dots, Y_m, v) \cdot \delta(v - v_0) \\ & + 1/2 \int_{v_0}^{v-v_0} K(u, v-u) n(u, t) n(v-u, t) du - n(v, t) \int_0^\infty K(u, v) n(u, t) du \quad (5-6) \end{aligned}$$

The terms in PBE i.e., Equation (5-6) from the left-hand side to the right-hand side are:

- Accumulation term of the particle number density.
- Convection term in physical space.
- Condensation/growth term in phase space, where $G(Y_1, Y_2, \dots, Y_m, v)$ is the growth kernel, a function species concentration Y_m and particle volume v .
- Particle diffusion term, where D_p is the diffusion coefficients of particles.
- Nucleation term, where $B_n(Y_1, Y_2, \dots, Y_m, v)$ is the nucleation kernel, Y_m is a function of species concentration and v is particle volume. This term contributes a source for particle with the size of v_0 which is the minimum particle size of the nuclei.
- Coagulation term, which consists of two parts. The first part is the birth part accounting for all the possible gains in particle number density of particles with size of v due to the coagulation between particle of size $(v-v_0)$ and v_0 . The factor 1/2 is used to prevent double counting the coagulation events.

The second part is the death part accounting for all the loss of particles with size of v due to all the possible combinations. $K(u, v)$ is the coagulation kernel dependent on the size of colliding pairs.

5.2.2 PDF Transport Equation Formulation

The derivation of PDF formulation for aerosol dynamics in turbulent flows is based on the work of Rigopoulos (2007). First, a joint multipoint PDF of the mass concentration and particle number density of species at full size range is introduced so that the expected PSD at any point can be determined:

$$Y(\mathbf{x}, t), n(v, \mathbf{x}, t) \equiv f(Y, N; \mathbf{x}, t) \quad (5-7)$$

where $Y \equiv y_1, y_2, \dots, y_m$ and $N \equiv n_1, n_2, \dots, n_n$ have the following constraints:

$$y_a < Y_a(\mathbf{x}, t) < y_a + dy \quad (5-8a)$$

$$n < N(v_i, \mathbf{x}, t) < n + dn \quad (5-8b)$$

and the normalization property is also satisfied:

$$\int_0^1 \int_0^\infty f(Y, N; \mathbf{x}, t) dY dN = 1 \quad (5-9)$$

5.2.2.1 Discretization of the Continuous PBE

As the continuous function of $n(v, x, t)$ is needed for the source terms (e.g., the nucleation growth/condensation and coagulation), the continuous PBE is discretized based on the approximation of infinite space points with finite space points (Rigopoulos and Jones, 2003):

$$N(v) \approx \{N(v_1), N(v_2), \dots, N(v_n)\} = \{N_1, N_2, \dots, N_n\} \quad (5-10)$$

The growth term in Equation (5-6) is discretized as follows:

$$\begin{aligned}
& \partial(G(Y_1, Y_2, \dots, Y_m, v)/\partial v \cdot n(v)) \\
& \approx (G(Y_1, Y_2, \dots, Y_m, v)) \cdot \left(\frac{N_i}{v_i - v_{i-1}} - \frac{N_{i-1}}{v_i - v_{i-1}} \right) + N_i \cdot \partial(G(Y_1, Y_2, \dots, Y_m, v)/\partial v) \\
& = G_1(Y_1, Y_2, \dots, Y_m, v) \cdot N_i + G_2(Y_1, Y_2, \dots, Y_m, v) \cdot N_{i-1} \quad (5-11)
\end{aligned}$$

where

$$G_1 = G(Y_1, Y_2, \dots, Y_m, v) \cdot 1/(v_i - v_{i-1}) + \partial(G(Y_1, Y_2, \dots, Y_m, v_i)/\partial v)$$

$$G_2 = -G(Y_1, Y_2, \dots, Y_m, v) \cdot 1/(v_i - v_{i-1})$$

The nucleation term in Equation (5-3) is discretized as:

$$\begin{aligned}
& B(Y_1, Y_2, \dots, Y_m, v) \cdot \delta(v - v_0) \\
& \approx B(Y_1, Y_2, \dots, Y_m, v) / [1/2(v_1 - v_0)] + B(Y_1, Y_2, \dots, Y_m, v) / [1/2(v_0 - 0)] \\
& = B_1(Y_1, Y_2, \dots, Y_m) \quad (5-12)
\end{aligned}$$

The coagulation term is discretized as:

$$C \approx 1/2 \sum_{j=1}^{i-1} a_{i-j,j}(v_{i-j}, v_j) \cdot N_{i-j} N_j - N_i \sum_{j=1}^{i-1} a'_{i-j,j}(v_i, v_j) \cdot N_j \quad (5-13)$$

where C represents the coagulation term in Equation (5-6), $a_{i-j,j}$ and $a'_{i-j,j}$ are the coagulation kernels.

Based on the above discretized terms, the discretized form of PBE can be written as:

$$\begin{aligned}
& \partial N_i / \partial t + \nabla(u \cdot N_i) + G_1 \cdot N_i + G_2 \cdot N_{i-1} \\
& = D_p \nabla^2 n(v) + B_1(Y) + 1/2 \sum_{j=1}^{i-1} a_{i-j,j}(v_{i-j}, v_j) \cdot N_{i-j} N_j - N_i \sum_{j=1}^{i-1} a'_{i-j,j}(v_i, v_j) \cdot N_j
\end{aligned} \quad (5-14)$$

5.2.2.2 Final PDF Transport Equation

The transport equation PDF can be obtained via averaging the time derivative of the fine-grained density (Lundgren, 1967) which is given as follows:

$$\frac{\partial f}{\partial t} = \left\langle \frac{\partial F}{\partial t} \right\rangle = \left\langle - \sum_{a=1}^M \frac{\partial F}{\partial y_a} \frac{\partial Y_a}{\partial t} - \sum_{i=1}^N \frac{\partial F}{\partial n_i} \frac{\partial N_i}{\partial t} \right\rangle \quad (5-15a)$$

where

$$F = \prod_{a=1}^M \delta(Y_a - y_a) \cdot \prod_{i=1}^N \delta(N_i - n_i) \quad (5-15b)$$

Substituting the derivative terms in Equation (5-15) with corresponding terms in Equation (5-14), the following equation can be obtained:

$$\begin{aligned}
& \frac{\partial F}{\partial t} = - \sum_{a=1}^M \frac{\partial F}{\partial y_a} [-\nabla(u \cdot Y_a) + D \nabla^2 Y_a + \dot{w}(Y_1, Y_2, \dots, Y_m)] \\
& - \sum_{i=1}^N \frac{\partial F}{\partial n_i} [-\nabla(u \cdot N_i) - G_1 \cdot N_i - G_2 \cdot N_{i-1} + D_p \nabla^2 N_i + B_1(Y_1, Y_2, \dots, Y_m) \\
& + 1/2 \sum_{j=1}^{i-1} a_{i,j} \cdot N_{i-j} N_j - N_i \sum_{j=1}^{i-1} a'_{i,j} \cdot N_j]
\end{aligned} \quad (5-16)$$

Substituting Equation (5-16) into Equation (5-15), the final transport equation of PDF is obtained as follows:

$$\begin{aligned}
\frac{\partial f}{\partial t} = & -u \cdot f - \langle u \cdot \nabla F \rangle - \sum_{a=1}^m \sum_{b=1}^m D \frac{\partial^2 (\nabla Y_a \cdot \nabla Y_a \cdot F)}{\partial y_a \partial y_b} \\
& - \sum_{a=1}^m \sum_{b=1}^m D_p \frac{\partial^2 (\nabla N_i \cdot \nabla N_i \cdot F)}{\partial n_i \partial n_j} - \frac{\partial}{\partial y_a} [B_1(y_1, y_2, \dots, y_m) \cdot f] \\
& + \frac{\partial}{\partial n_i} [(G_1(y_1, y_2, \dots, y_m) n_i - G_2 \cdot n_{i-1}) \cdot f] \\
& - \sum_{i=1}^n \frac{\partial}{\partial n_i} [1/2 \sum_{j=1}^{i-1} (a_{i,j} n_i n_j) \cdot f] + \sum_{i=1}^n \frac{\partial}{\partial n_i} [n_i \sum_{i=1}^n [(a_{i,j} N_j) \cdot f] \quad (5-17)
\end{aligned}$$

5.2.3 Monte Carlo Simulation of the PDF Transport Equation

The Monte Carlo method developed by Fox (2003) is further extended to solve the PDF transport equation of aerosol dynamics in turbulent flows. The underlying concept of this Monte Carlo method is to simulate a number of stochastic entities, whose evolution statistics obtained via stochastic differential equations as well as CFD method approximate the PDF of interest. The stochastic model for the evolution of particle position and particle number density used to advance PDF is as follows:

$$X^n(t+\Delta t) = X^n(t) + [\langle U \rangle (X^n(t), t) + \nabla \Gamma_T (X^n(t), t)] \Delta t + 2\Gamma_T (X^n(t), t) 1/2 \Delta W \quad (5-18)$$

$$N^n(t+\Delta t) = N^n(t) + [C_N/2 (\langle N^n(t) \rangle - N^n(t)) + \dot{W}_i(N, Y)] \Delta t \quad (5-19)$$

where ΔW_i is a Gaussian pseudo-random number for representing the stochastic fluctuations of Wiener process with mean $\langle \Delta W_i \rangle = 0$ and covariance $\langle \Delta W_i \cdot \Delta W_j \rangle = \Delta t \delta_{i,j}$, C_N is the characteristic scale concerning micro mixing, $\dot{W}_i(N, Y)$ is the source term for accounting the variation of particle number density, Γ_T is the turbulent diffusion coefficient, $\langle U \rangle$ is the average velocity.

It is noteworthy that in the simulation of coagulation event of particles with a certain size, instead of looping several neighboring grid cells which contain a large amount of notional particles, the loop checking will be carried out within only one grid cell. It implies that the loop checking will be performed over all the particles located within the grid cell to counter check if they are involved in coagulation events. The possible grid cell in which the tracked particles may be located after a time step, Δt is determined before sorting its possible coagulation partners. Then Monte Carlo method is applied to determine the probability of certain aerosol dynamic events in the certain grid cell. It is reasonably assumed that all the coagulation events within one time step, Δt of a tracked notional particle take place in one same grid cell. By this assumption, the computational time spent on sorting particles for coagulation is greatly reduced, thus increasing the computational efficiency.

The procedures of one loop of Monte Carlo simulation are as follows (several repetitions may be carried out in order to reduce the statistical errors caused by the intrinsic nature Monte Carlo method):

Step 1: Initialization of particle properties (particle size distribution, particle number density and initial positions) and the turbulence field (average velocity $\langle U \rangle(x, 0)$, turbulence frequency $\omega(x, 0)$ and turbulent diffusion coefficient $\Gamma_T(x, 0)$);

Step 2: Based on the turbulence field parameters in the previous step, calculate the time step to advance the transport PDF according to Equation (5-20) i.e., constraints of Courant-Friedrichs-Lewy (CFL) number and minimum

characteristic time scale of all the aerosol dynamic processes. The final time step is calculated as follows:

$$\Delta t = c \cdot \text{Minimum} \left\{ N_{\text{CFL}} / \left(\sum_{i=1}^m \frac{u_i}{\Delta L_i} \right), t_{\text{coag}}, t_{\text{nuclea}}, t_{\text{growth}} \right\} \quad (5-20)$$

where c is a constant factor to guarantee the decoupling between the particle dynamics processes and the particle transport, N_{CFL} is the maximum CFL number which is also a constant ($N_{\text{CFL}} = 0.5$ is used in the present study). m is the number of dimensions (for two-dimensional flow, $m = 2$), u_i is the velocity at i -direction, L_i is the width of the grid cell in i -direction, t_{coag} , t_{nuclea} , t_{growth} are the characteristic time scale of coagulation, nucleation and growth processes, respectively which are dependent on the local field parameters (i.e., mass concentration, particle size etc.);

Step 3: Advance the computing of flow field with a finite volume method (FVM) CFD code and return the turbulence field parameters including average velocity, $\langle U \rangle(x, \Delta t)$, turbulence frequency, $\omega(x, \Delta t)$ and turbulent diffusion coefficient, $\Gamma_T(x, \Delta t)$;

Step 4: Monte Carlo method is used to calculate the particle position $X^n(\Delta t)$ and particle number density, $N^n(\Delta t)$. A sorting algorithm based on random number is used to determine the N_{pl} particles and renumber them according to their grid cells. The intra cell process, particularly aerosol dynamic processes, are advanced to determine the source terms in the PDF transport equation (in Equation (5-17)).

Step 5: Update the particle properties accordingly. Using these updated particle properties, particle-field estimates are constructed by particle source in cell (PSIC)

scheme (Crowe et al., 1977) after one time step, Δt to obtain PDF. More details can be referred to Fox (2003);

Step 6: Check whether the accumulative simulation time, t has reached the prescribed stopping time, t_{stop} , if not, go to Step 2 to continue the simulation.

If $t \geq t_{\text{stop}}$, stops the Monte Carlo simulation. Figure 5.1 presents a flowchart of the Monte Carlo simulation procedures.

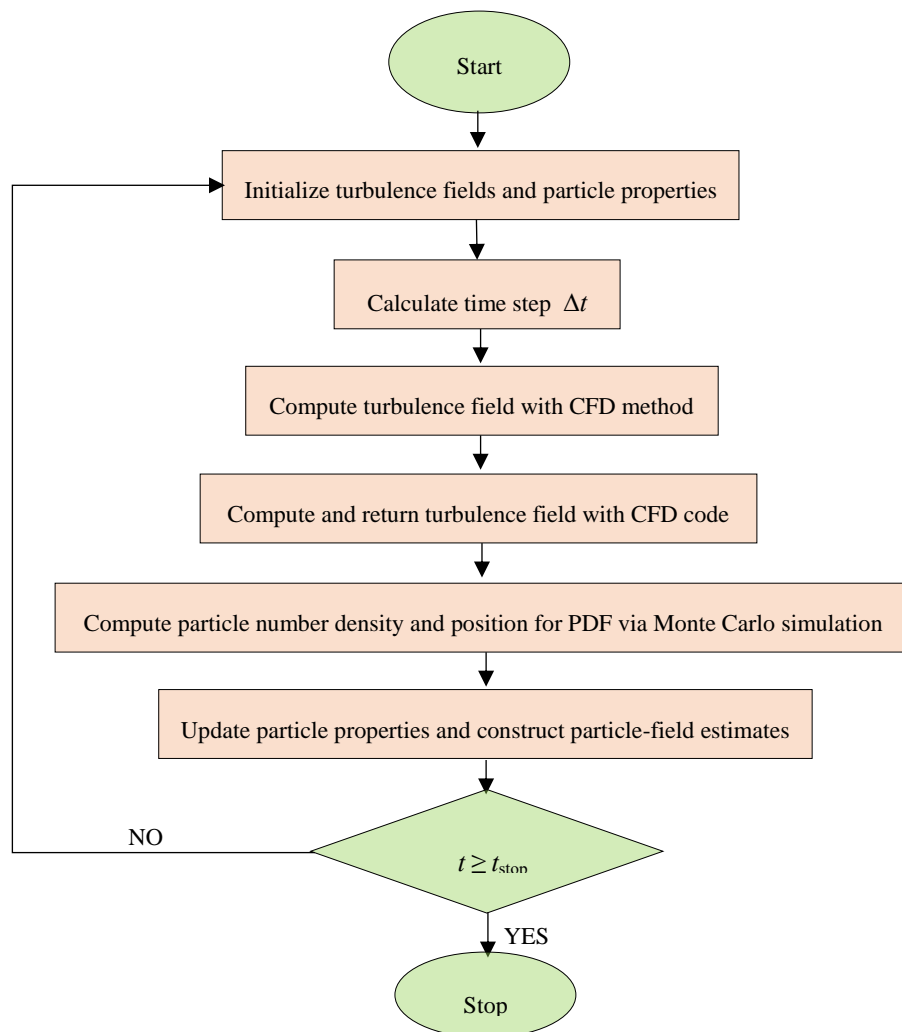


Figure 5.1 Flow chart of the coupled CFD-Monte Carlo/PDF method (Liu and Chan, 2016).

5.2.4 Simulation Analysis

Maximum relative error, ε and convergence time are used to show the computational accuracy and efficiency. The definition of the maximum relative error, ε_{\max} is written as:

$$\varepsilon_{\max} = \left\{ \sqrt{[(n-n_0)/n_0]^2} \right\}_{\max} \quad (5-21)$$

where n is the particle number density obtained via CFD-MC method and n_0 is the particle number density obtained via the PBSM method based on the work of Hounslow (1988). ε is the maximum relative error taken over the whole PSD obtained via the above-mentioned two methods. Convergence time is defined as the time needed for the physical quantities to reach the convergence criteria (1×10^{-5}) with the proposed CFD-MC method. Normalized convergence time is defined as the ratio of any convergence time to the shortest convergence time (i.e., the convergence time of turbulent coagulation with Re_j of 3200) in the present study.

The developed PBE (Hounslow, 1988) is used together with a dimensional splitting technique (Ma et al., 2002) to formulate the PBSM method in this Chapter 5 which makes the method applicable to multi-dimensional PBE. Although the method of Hounslow (1988) is for a homogeneous PBE, it can be modified to be applicable to multi-dimensional cases in the present study. The specific method is to apply the one-dimensional high-resolution algorithm to each one-dimensional homogeneous PBE (Equation 5-22) by setting the velocities to be zero except for one certain coordinate sequentially at each time step (Gunawan et al., 2004):

$$\frac{\partial f}{\partial t} + \sum_{j=1}^n \frac{\partial(M_j(L)f)}{\partial L_j} = 0 \quad (5-22)$$

where M_j is the rate of certain aerosol dynamic process, L_j is the internal coordinate including spatial coordinate, j is the number of internal coordinates.

In order to analyze the variation of particle number density along the axial distance, the particle number density is sampled at different evenly distributed positions in the axial direction with the interval of 0.125 m, which is then plotted versus axial distances. The normalized particle number density is defined as the ratio of local particle number density to the particle number density at the outlet of the nozzle as follows:

$$N_n = \frac{N_l}{N_0} \quad (5-23)$$

where N_n is the normalized particle number density, N_l is the local particle number density in the computational domain and N_0 is the particle number density at the outlet of the nozzle.

5.3 Simulation Setup

The configuration of the aerosol reactor in the present study is shown in Figure 5.2. The aerosol reactor is a cylindrical aerosol reactor with radius of 0.225 m and length of 2 m. A nozzle with radius of 0.005m and length of 0.01 m is located at the center of the cylindrical aerosol reactor. Three internals with height of 0.05 m and thickness of 0.0005 m are evenly mounted in the axial direction inside cylindrical aerosol reactor in order to enhance mixing. For aerosol dynamics in

turbulent flows, particles with a volume fraction of 0.1 in the carrier gas (air) is injected from the nozzle while gas phase (air) is injected through the gas phase inlet. The injected particles are potassium chloride (KCl) particles with a size range of 0.1 μm to 6.4 μm and density of 1980 kg/m^3 (Calvo et al., 2013). The injection velocity of particulate phase ranges from 10 m/s to 40 m/s, the inlet velocity of gas phase is 0.5 m/s. Coagulation kernel is obtained using the turbulent coagulation model by Saffman and Turner (1956). The nucleation rate is kept constant at $7.5 \times 10^{-6} \text{ m}^{-3}\text{s}^{-1}$ with constant growth rate of $6.2 \times 10^{-11} \text{ m/s}$. Aerosol dynamics in laminar flow is also investigated in the same aerosol reactor for comparison with aerosol dynamics in turbulent flows, which is carried out by switching the inlet conditions of velocity and species between inlets of the nozzle and the gas phase. The Reynolds number Re_j of particulate phase is 1440 in the laminar flow. In the turbulent flow, particles are injected from the nozzle of the aerosol reactor at 10 m/s as shown in Figure 5.2. However, in the laminar flow, particles are injected through the air inlet at 0.1 m/s. Although the velocity of the jet in turbulent flow (10 m/s) is higher than that of laminar flow (0.1 m/s), the cross-sectional area of the entrance for particles in laminar flow (i.e., the cross-sectional area of the aerosol reactor with a diameter of 0.225 m) is much higher than that for turbulent flow (i.e., the cross-sectional area of the nozzle with a diameter of 0.005 m). Thus, the volume flowrate for laminar flow is much higher than that for turbulent flow in the present study, which is shown as follows:

$$\dot{Q}_{\text{laminar}} = 20.25 \dot{Q}_{\text{turbulent}} \quad (5-24)$$

where \dot{Q}_{laminar} and $\dot{Q}_{\text{turbulent}}$ are the volumetric flow rates of laminar flow and turbulent flow, respectively. So the result of laminar flow in Figure 5.5 is scaled

down to be consistent with the volumetric flow rate of the turbulent flow. Specifically, for the study of aerosol dynamics in the laminar flow, particles enter the gas phase inlet instead of the nozzle as shown in Figure 5.2 while the nozzle is used for the entry of air at a low velocity of 0.5 m/s.

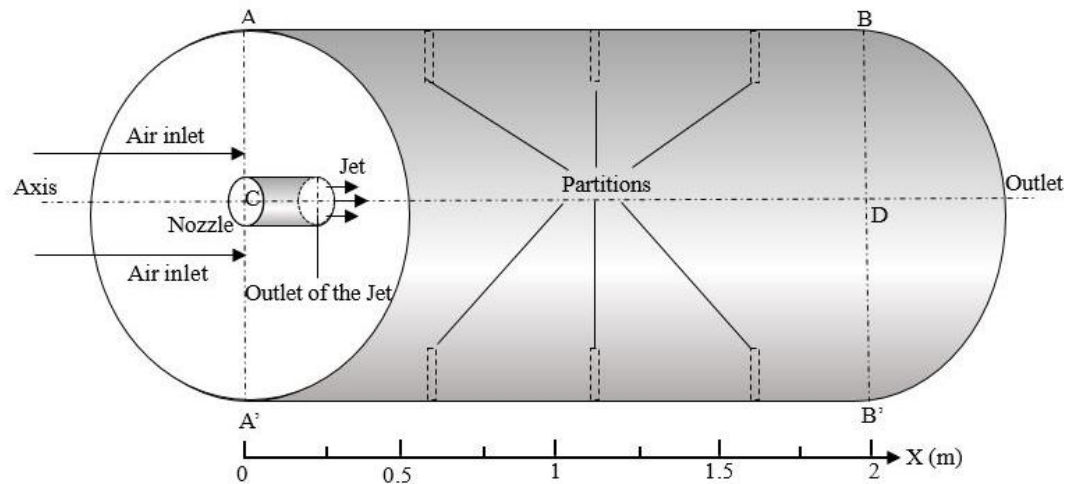


Figure 5.2 Three-dimensional schematic configuration of a cylindrical aerosol reactor (Two-dimensional axisymmetric grid is generated in the rectangular domain ABDC, not in scale) (Liu and Chan, 2016).

Due to the axisymmetrical configuration of the studied cylindrical aerosol reactor, a two-dimensional axisymmetric unstructured grid corresponding to the aerosol reactor is treated as shown in Figure 5.3. There are totally 8112 cells and 8444 nodes in the grid. The grid near the nozzle zone and internals is refined. Four injection velocities of particulate phase i.e., 10 m/s, 15 m/s, 20 m/s and 40 m/s are used to investigate the effect of jet Reynolds (Re_j) number on the aerosol dynamics in turbulent flows. Temperature is kept at 300 K for all the computational domain. The standard k - ϵ turbulence model is used for the turbulence computation. After balancing the computational accuracy and cost (i.e., computational time, computer memory etc.), 30 notional particles are allocated in each cell in the present

Monte Carlo simulation. The simulation parameters for aerosol dynamics in turbulent flows are summarized in Table 5.1

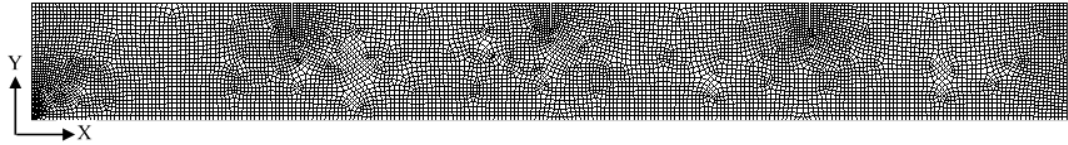


Figure 5.3 Two-dimensional axisymmetric unstructured computational grid of a cylindrical aerosol reactor (Liu and Chan, 2016).

Table 5.1 Simulation parameters for aerosol dynamics in turbulent flows (Liu and Chan, 2016).

Particulate phase	Potassium chloride (KCl)
Particle density (kg/m^3)	1980
Initial particle size range (μm)	0.1-6.4
Injection velocity of the jet (m/s)	10-40
Corresponding Re_j of the jet	3200–12800
Velocity of continuous phase (m/s)	0.5
Coagulation model	Turbulent kernel (Saffman and Turner, 1956)
Nucleation rate ($\text{m}^{-3}\text{s}^{-1}$)	7.5×10^6
Growth rate (m/s)	6.2×10^{-11}
The number of cells in the computational domain	8112
The number of numerical particles per cell	30
Turbulence model	$k-\varepsilon$ model

5.4 Results and Discussion

5.4.1 Comparison of Coagulation in Both Laminar and Turbulent Flows

As mentioned above in Section 5.3, the inlet of fluid and particulate phases is switched to simulate laminar flow, i.e., the particles are injected into the aerosol reactor through the air inlet while air is injected through the nozzle (as shown in Figure 5.2). The Re_j number at the nozzle is 3200 with the injection velocity of 10 m/s for turbulent flows. The entry velocity of the gas phase (air) is 0.5 m/s for both cases.

Figure 5.4 shows the initial PSD of particles before entering the aerosol reactor. It can be seen that small particles account for the majority of the total particle population. Figure 5.5 shows the PSD for particles after coagulation in both laminar and turbulent flows. Compared with the PSD in Figure 5.4, it can be seen that the PSD in Figure 5.5 varies significantly in its shape and order of magnitude (decreasing the order of magnitude from 10^{19} to 10^{16}) due to coagulation. Coagulation is obviously enhanced in turbulent flows which can be seen from the wider spectrum of PSD and higher maxima of particle number density when compared to that in laminar flow. This is because coagulation in an inter-particle process is dependent on the concentration and the mixing effect of particles. Enhanced coagulation leads to a higher particle number density of particles with diameter of 0.6 μm . As coagulation is only enhanced but the coagulation mechanism is not changed, the peaks of the PSDs for laminar coagulation and turbulent coagulation in Figure 5.5 appear in the same particle size.

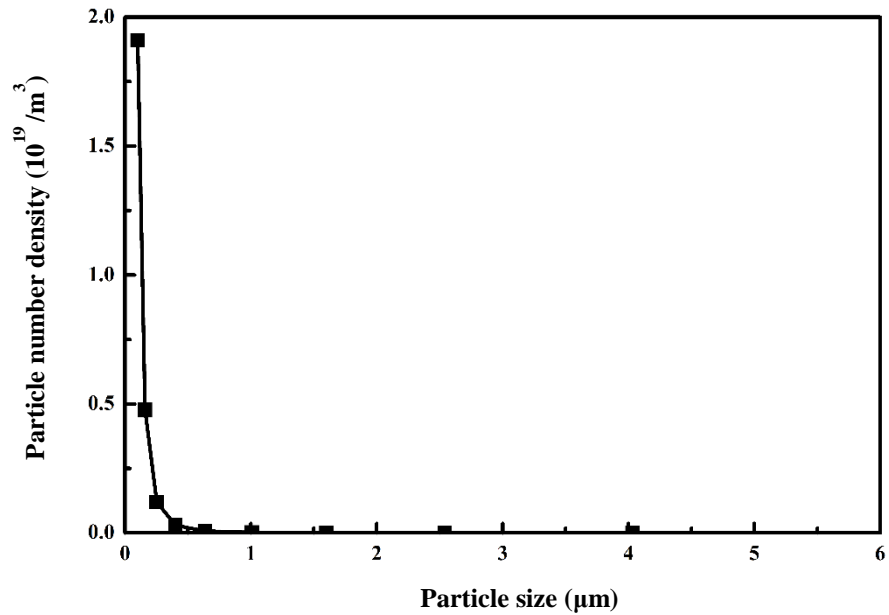


Figure 5.4 Initial PSD of particles before entering the aerosol reactor (Liu and Chan, 2016).

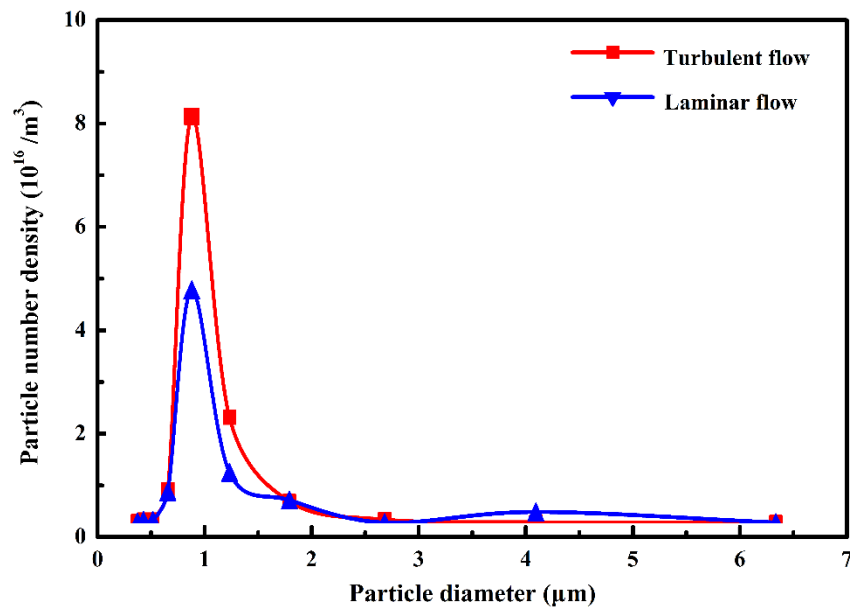


Figure 5.5 PSD in laminar and turbulent coagulation (Liu and Chan, 2016).

Figure 5.6 shows the particle number density distribution within the same aerosol reactor for laminar and turbulent flows, respectively. As particle number

density decreases during pure coagulation process, the coagulation rate distribution can be characterized by the particle number density distribution within the aerosol reactor. From Figure 5.6(a), the high particle number density regions can be found throughout the first half of the aerosol reactor in laminar flow which implies low coagulation rates in these regions. The particle number density does not decrease significantly until the second half of the aerosol reactor. It suggests that coagulation mainly takes place in the second half of the aerosol reactor, which renders high particle number density and low average coagulation rate throughout the whole aerosol reactor in laminar flow. It can be seen from Figure 5.6(b), however, the particle number density in turbulent flows remains very low in most of the regions within the aerosol reactor except for some zones near the outlet of the aerosol reactor and behind the internals. It demonstrates that coagulation process is obviously enhanced in turbulent flows compared to coagulation in laminar flow.

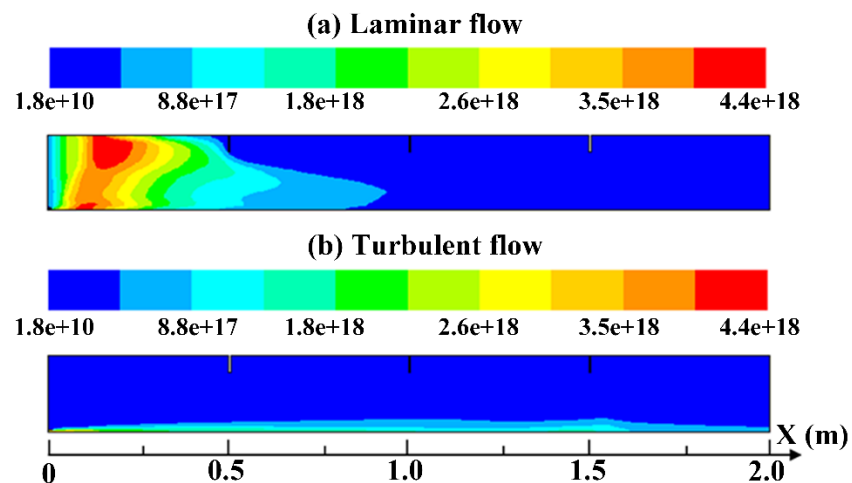


Figure 5.6 Particle number density (m^{-3}) contour in laminar and turbulent coagulation (Liu and Chan, 2016).

5.4.2 The Effect of Re_j Number on Coagulation in Turbulent Flows

The enhanced effect of turbulence on coagulation is shown in Section 5.4.1. The effect of different Re_j numbers on coagulation process in turbulent flows is further studied. Varied jet velocities of 10 m/s, 15 m/s, 20 m/s and 40 m/s are used with corresponding Re numbers of 3200, 4800, 6400 and 12800, respectively. The results obtained via the proposed Lagrangian Monte Carlo/PDF (LMC-PDF) method are directly compared with those obtained via the modified population balance sectional method (PBSM) (Hounslow, 1988).

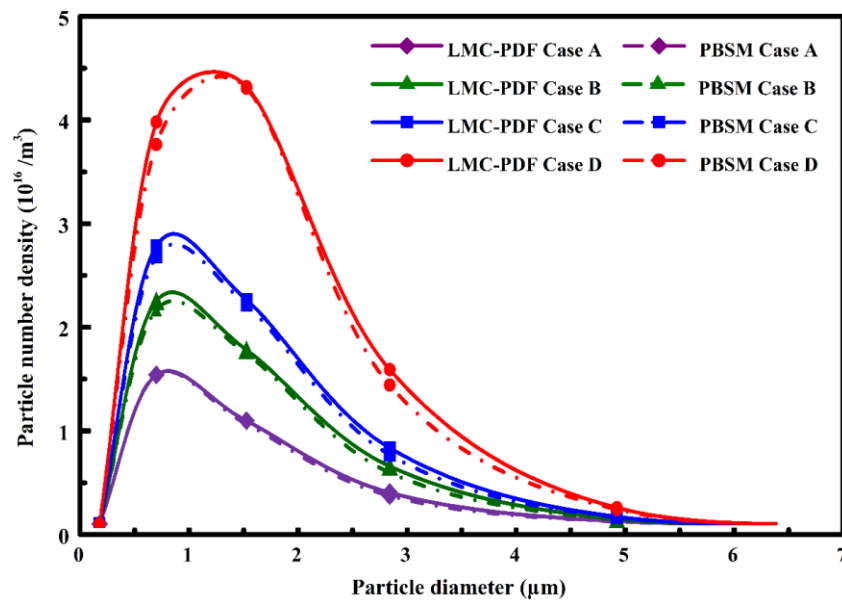


Figure 5.7 PSD in turbulent coagulation: Case A, $Re_j = 3200$; Case B, $Re_j = 4800$; Case C, $Re_j = 6400$; Case D, $Re_j = 12800$ (The PBSM results are obtained based on the method proposed by Hounslow (1988)) (Liu and Chan, 2016).

Figure 5.7 shows the obvious effect of different Re_j numbers on the PSD of aerosol particles experiencing coagulation process in turbulent flows. With Re number of the jet increasing from 3200 to 12800, the PSDs become wider and higher, with the peaks moving towards the larger end of particle size range, which yields a

more evenly distributed population of particles. By controlling proper turbulent flow field, the control over PSD of aerosol particles can be achieved which is of importance in industrial and engineering applications. Comparing the results obtained with the proposed LMC-PDF method and PBSM (Hounslow, 1988), an excellent agreement can be found, which validates the reliability and computational efficiency of this proposed LMC-PDF method. The wider PSD with increasing Re_j number is also in accordance with the previous research studies by Reade and Collins (2000) and Garrick (2015), which reveals the effect of turbulence on PSD. By increasing Re_j numbers, turbulence induced mixing is greatly enhanced, which leads to enhanced coagulation process. Meanwhile, the peaks of PSD moving towards the upper end of particle size spectrum with increasing Re_j number implies that more and larger particles are produced by enhanced coagulation. In other words, as coagulation is enhanced, larger particles have a better chance to appear due to more frequent collisions.

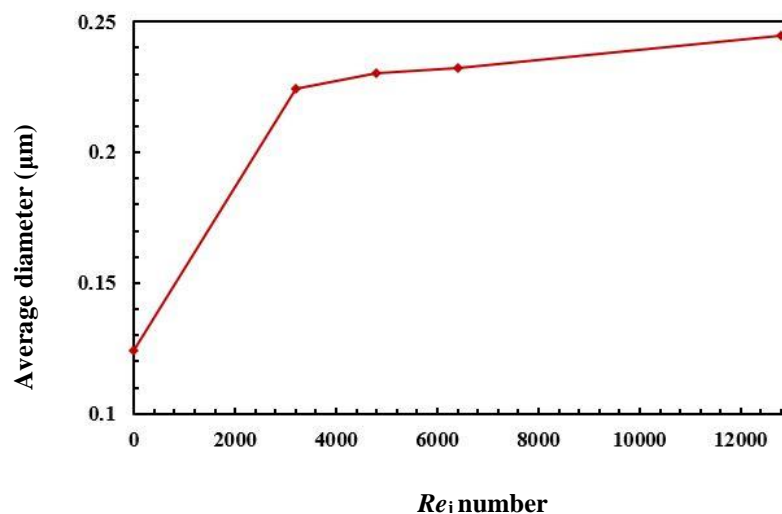


Figure 5.8 Average diameter of particles in turbulent coagulation (Liu and Chan, 2016).

According to the definition of particle number based on average diameter of particles (Friedlander, 2000), the number averaged particle diameter can be obtained by integrating the PSD over the entire particle diameter range and then averaging over the total particle number density of particles. Using this method, the initial average diameter and average diameters of particles under the turbulent coagulation for different Re_j numbers are obtained and shown in Figure 5.8. An increase in average diameter from 0.124 μm to 0.245 μm can be observed with increasing Re_j number from 0 to 12800, which is an obvious increase considering the large number of aerosol particles in the aerosol reactor. The Re_j number of zero corresponds to the initial PSD of aerosol dynamics before entering the aerosol reactor. As higher Reynold number of the jet is related to higher turbulent intensity in the present study, the increase of average particle diameter with Re_j number indicates that coagulation is significantly enhanced, which may be explained by the enhanced mixing and more frequent collisions between particles.

The turbulent kinetic energy (m^2/s^2) under different Re_j numbers is presented in Figures 5.9(a) to (d). As the length of aerosol reactor is 2 m, which is much longer than the nozzle whose length is only 0.01 m, the turbulent zones directly caused by the injection of particulate phase are quite limited as shown in Figure 5.9. The maximum axial length is around 0.5 m (determined from the first internal in the aerosol reactor) and the maximum radial length is around 0.05 m, which is less than a quarter of the radius of the aerosol reactor. With the increasing Re_j number, the turbulent kinetic energy (m^2/s^2) also increases according to Figure 5.9. However, the results presented in Figure 5.7 indicate that turbulence has significant impact on coagulation process in turbulent flows despite of the limited zones of

turbulence. Coagulation in highly turbulent regions is greatly enhanced as more frequent collisions take place producing more and larger particles.

The particle number density (m^{-3}) contour in turbulent coagulation under different Re_j is shown in Figure 5.10. It can be seen that despite of the similar distribution pattern of particle number density in the aerosol reactor, the particle number density decreased with increasing Re_j number due to coagulation, which suggests an increase in average coagulation rate with the increase of Re_j number. The results in Figure 5.10 are also consistent with those in Figure 5.8, indicating the enhancing effect of turbulence on coagulation.

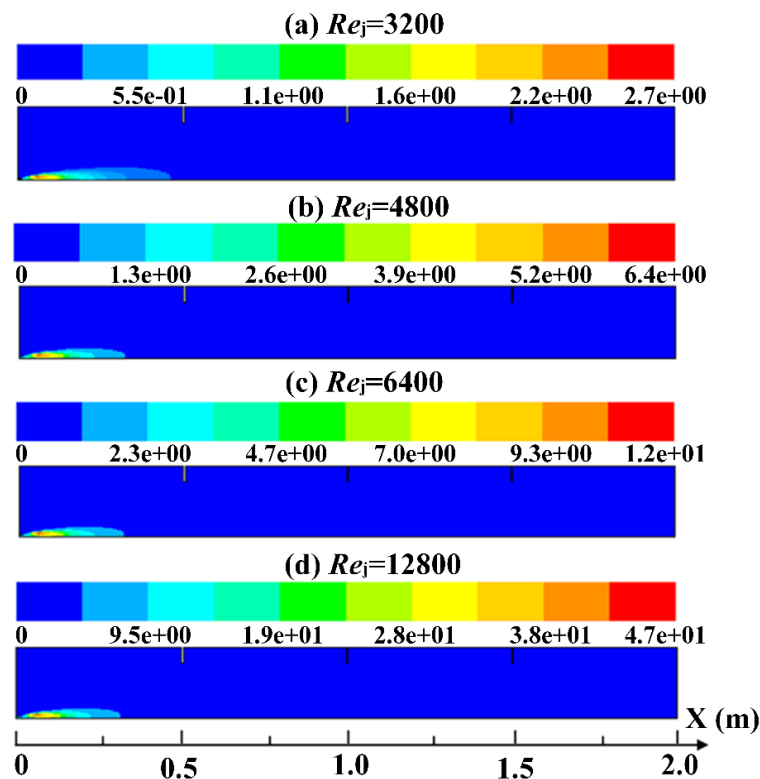


Figure 5.9 Turbulent kinetic energy (m^2/s^2) contour in turbulent coagulation (Liu and Chan, 2016).

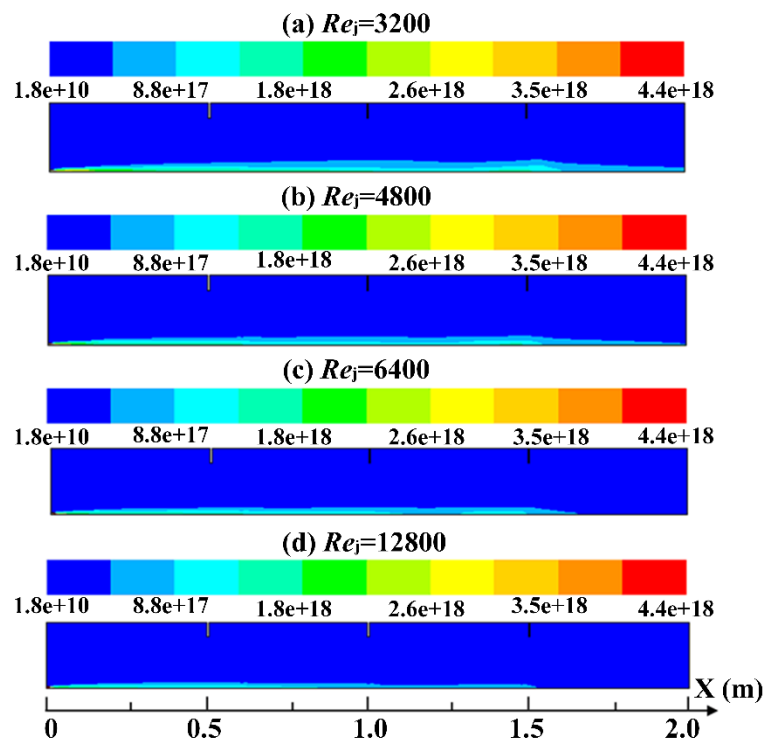


Figure 5.10 Particle number density (m^{-3}) contour in turbulent coagulation (Liu and Chan, 2016).

Figure 5.11 shows the variation of normalized particle number density with the axial distance under different Re_j . As coagulation process continuously reduces particle number density, it can be seen that the normalized particle number density for any fixed Re_j decreases with the axial distance as coagulation process takes place. Consider the same axial position, the difference between the normalized particle number density shows the different coagulation rates. Obviously, a higher Re_j yields higher turbulence, which in turn leads to a higher coagulation rate. The results in Figure 5.11 show clearly the enhancing effect of turbulence on coagulation. When Re_j reaches 12800, the maximum value used in the present study, it can be observed that the normalized particle number density first decreases rapidly, then decreases slightly and finally decreases with the rate almost equal to that with Re_j of

6400. The three-stage decrease of normalized particle number density indicates that the coagulation rate experiences with three different stages. This may be explained by the physical nature of coagulation process. Coagulation is a binary particle event which is dependent on local concentration and micro-mixing. Coagulation rate is first increased due to the enhanced mixing caused by high turbulence, which consumes a large number of particles in a short time. As a result, a low local concentration of particles in turn reduces the coagulation rate until more particles are accumulated and coagulation rate increases again in the final stage.

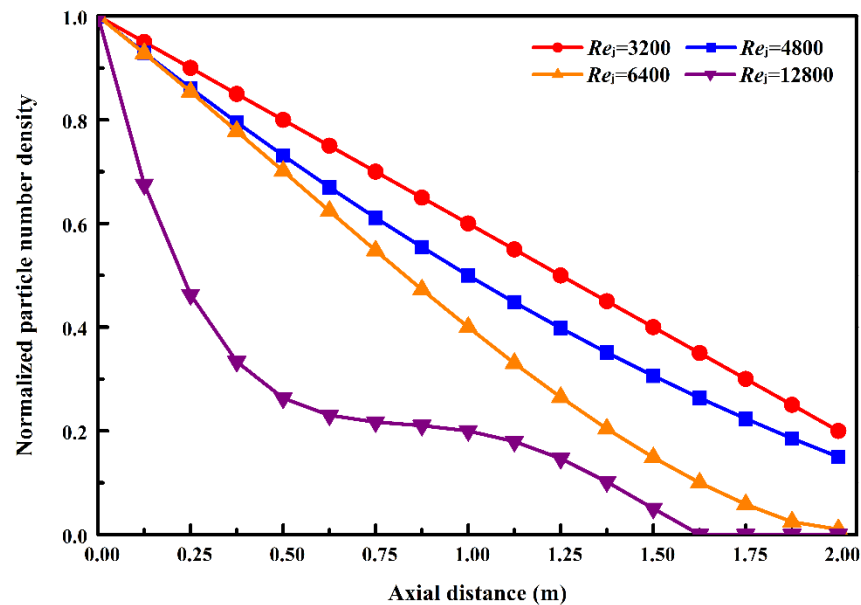


Figure 5.11 Normalized particle number density of turbulent coagulation (Liu and Chan, 2016).

5.4.3 The Effect of Re_j Number on Coagulation and Nucleation in Turbulent Flows

The effect of different Re_j numbers on two simultaneous aerosol dynamic processes (i.e., coagulation and nucleation) in turbulent flows is studied. The adopted Re_j numbers are the same as described before. Coagulation process is

modeled by the turbulence model used in Saffman and Turner (1956) while nucleation rate is kept constant as $7.5 \times 10^{-6} \text{ m}^{-3}\text{s}^{-1}$ for all the studied cases. Also, the results are validated with the PBSM (Hounslow, 1988).

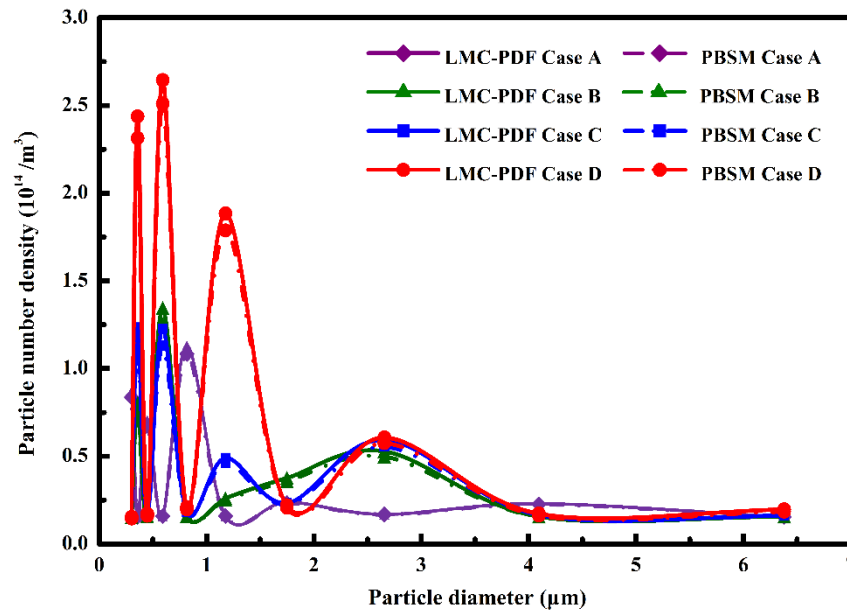


Figure 5.12 PSD for simultaneous coagulation and nucleation in turbulent flows: Case A, $Re_j = 3200$; Case B, $Re_j = 4800$; Case C, $Re_j = 6400$; Case D, $Re_j = 12800$ (The PBSM results are obtained based on the method proposed by Hounslow (1988)) (Liu and Chan, 2016).

The PSD of turbulent coagulation and nucleation for different Re_j numbers is shown in Figure 5.12. Compared with the PSD shown in Figure 5.7, in which only coagulation is involved, the PSDs presented in Figure 5.12 become much more complicated due to the simultaneous coagulation and nucleation processes in turbulent flows. For the case with Re_j number of 3200, the PSD extends throughout the full particle size range with peaks falling into both small size range (less than $1 \mu\text{m}$) and large size range (larger than $2 \mu\text{m}$), which suggests that the simultaneous nucleation and coagulation processes taking place and producing small particles and relatively large particles simultaneously. As Re_j number increases from

3200 to 4800, a new peak appears on the new PSD whose position is around $2.5 \mu\text{m}$ while the other part of the PSD only varies slightly. It indicates that coagulation process is enhanced, which produces relatively larger particles to some extent. However, as Re_j number increases from 4800 to 6400, a new peak appears at the position of $1 \mu\text{m}$ on the PSD while the other part of the PSD remains basically the same. It is probably because nucleation process is enhanced which will be discussed in the following Figure 5.13. With further increasing Re_j number from 6400 to 12800, the shape of PSD and the positions of peaks both remain unchanged, but the values of the peaks are greatly increased, which implies the competition between coagulation and nucleation is not changed. With Re_j number increases from 4800 to 12800, a transition from coagulation-dominant mechanism to competition between coagulation and nucleation can be reasonably concluded from Fig. 5.12.

According to Garrick (2015), nucleation is the dominant process until the collapse of the jet potential core and turbulent mixing begins in the proximal region of the jet, where coagulation becomes the dominant process and leads to a broader PSD. Although increasing Re_j number may lead to stronger turbulence in order to enhance coagulation, but high velocity of jet also causes the delay of turbulent mixing in which nucleation becomes dominant in the proximal region of the jet. The reason accounting for the change of PSD mentioned above can be verified by the evolution of average diameter of particles with increasing Re_j number as shown in Figure 5.13. It can be seen that the average diameter of particles increases slightly with increasing Re_j number from 3200 to 4800, and reaches the peak of around $0.8 \mu\text{m}$ on the PSD. This is due to the enhanced coagulation as nucleation leads to smaller average diameter of particles. Moreover, Figure 5.13

shows that average diameter of particles decreases when Re_j number is larger than 4800, which yields a maximum average diameter of particles at $Re_j = 4800$ for these four studied cases. The Re_j number at zero corresponds to the initial average diameter of particles before entering into the aerosol reactor.

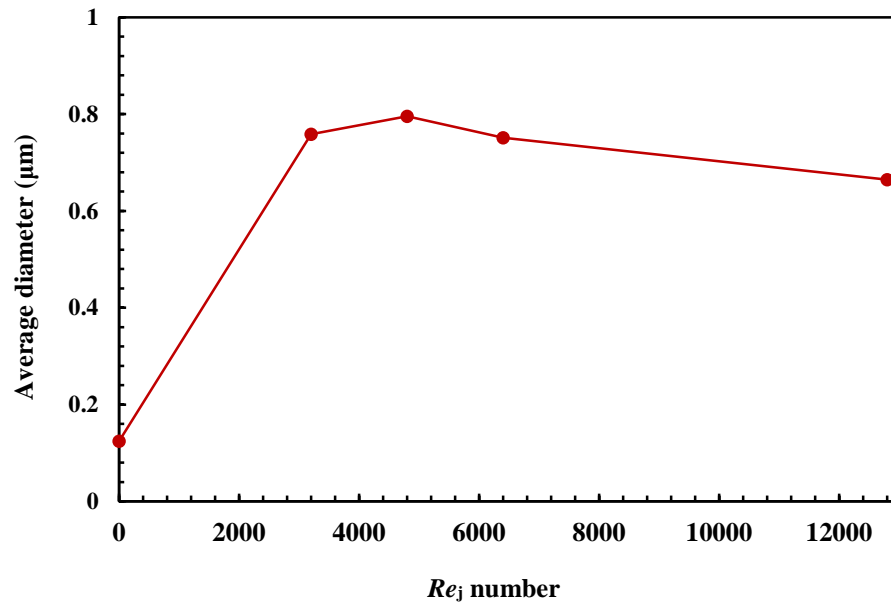


Figure 5.13 Average diameter of particles for simultaneous coagulation and nucleation in turbulent flows (Liu and Chan, 2016).

The contour of turbulent kinetic energy for different Re_j numbers is presented in Figure 5.14. It can be seen that with Re_j number increasing from 3200 to 12800, the maxima of turbulent kinetic energy is increased from $2.73 \text{ m}^2/\text{s}^2$ to $47.2 \text{ m}^2/\text{s}^2$, a significant increase of turbulence in the aerosol reactor, which affects the aerosol dynamics in turbulent flows by enhanced mixing as well as stochastic fluctuations. Actually, the interaction between turbulence and aerosol dynamics is the very challenging problem that is to be solved. The particle number density contour for simultaneous coagulation and nucleation is shown in Figure 5.15. With Re_j number increasing from 3200 to 4800, the maxima of the particle number density decreases,

implying that coagulation process which reduces particle density is dominant. An increase of the maxima of particle number density is observed when Re_j number increases from 4800 to 12800.

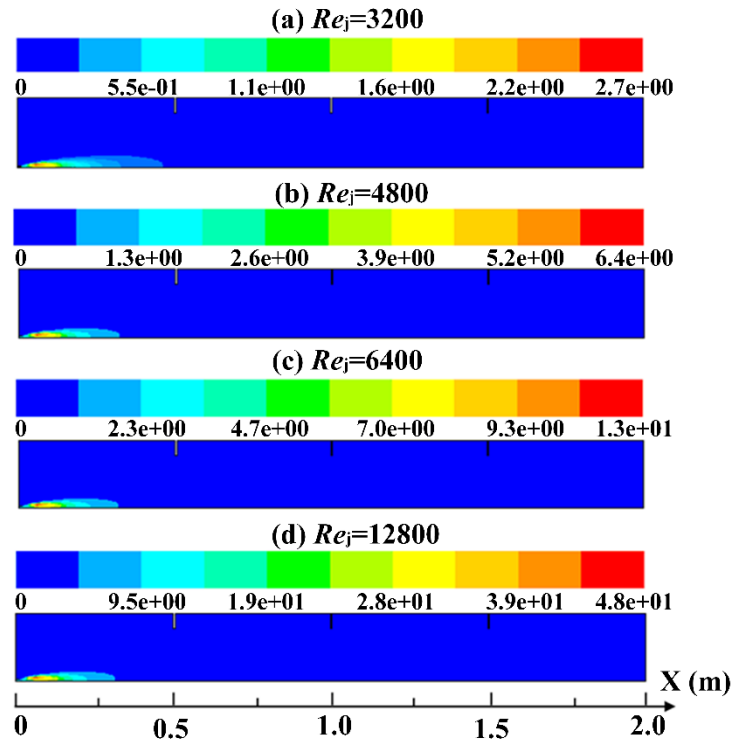


Figure 5.14 Turbulent kinetic energy (m²/s²) contour for simultaneous coagulation and nucleation in turbulent flows (Liu and Chan, 2016).

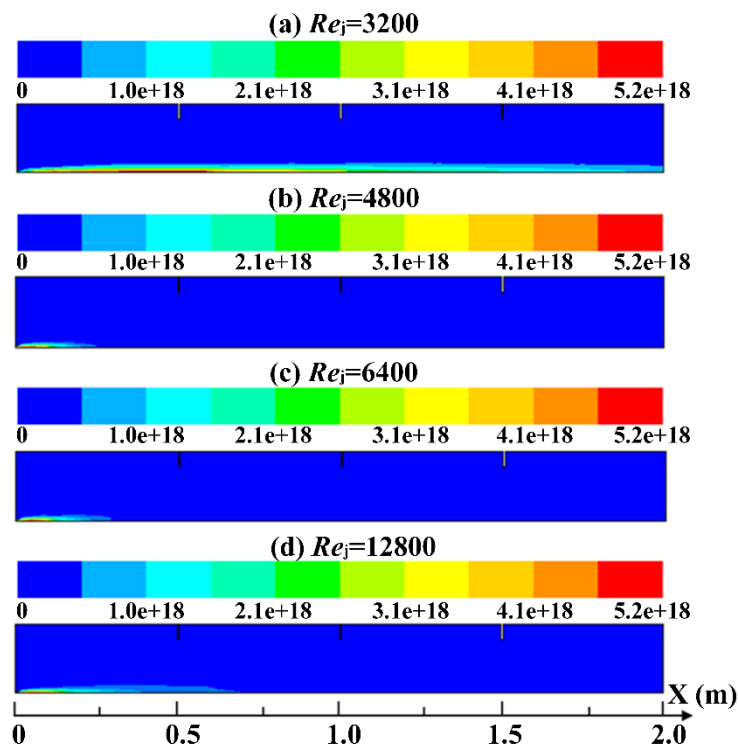


Figure 5.15 Particle number density (m^{-3}) contour for simultaneous coagulation and nucleation processes in turbulent flows (Liu and Chan, 2016).

Comparing Figure 5.15 with Figure 5.13, it can be found that the variation particle number density contour is consistent with the variation of average particle diameter in Figure 5.13, which reflects the fact that coagulation becomes dominant with Re_j number increasing from 3200 to 4800. However, as Re_j number increases from 4800 to 12800, nucleation becomes dominant in the competition with coagulation as the average particle diameter decreases continuously.

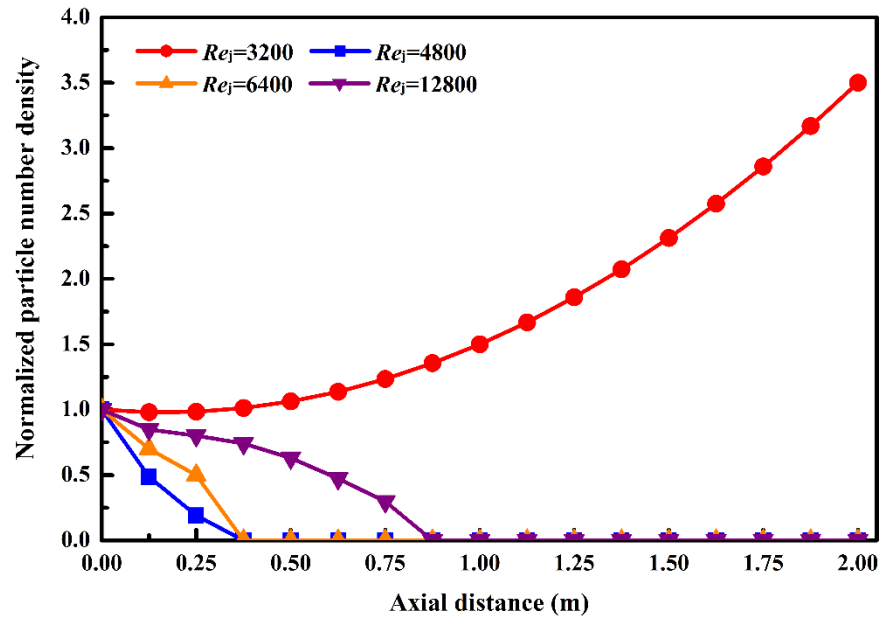


Figure 5.16 Normalized particle number density for simultaneous coagulation and nucleation in turbulent flows (Liu and Chan, 2016).

Figure 5.16 shows the variation of normalized particle number density with axial distance. It can be seen clearly that the normalized particle number density experiences significant change with Re_j number increasing from 3200 to 12800. The normalized particle number density increases rapidly with Re_j number of 3200, which implies that nucleation is the dominant mechanism resulting in a large number of new particles. As Re_j number increases from 3200 to 4800, the normalized particle number density decreases significantly, indicating that the dominant mechanism in the aerosol reactor changes from nucleation to coagulation as the latter reduces the total number of particles, which is also in accordance with the increase of average diameter as shown in Figure 5.13. However, as the Re_j number further increases from 4800 to 12800, the normalized particle number density also increases when compared with that with Re_j number of 4800 at the same axial position. These results indicate that coagulation is weakened while nucleation is enhanced when Re_j number increases from 4800 to 12800, which is consistent with the findings in

Garrick (2015) that too high injection velocity causes the delay of turbulent mixing and in turn reduces coagulation rate as mentioned above.

5.4.4 Simultaneous Coagulation, Nucleation and Growth Processes in Turbulent Flows

Complex aerosol dynamics in turbulent flows has been widely encountered and is a challenging problem in the numerical research. The PSDs of aerosol particles experiencing simultaneous coagulation, nucleation and growth processes for different Re_j numbers are shown in Figure 5.17. The results are also validated with PBSM (Hounslow, 1988). Comparing with the results of PSDs in Figure 5.12, it can be found that the shape of the PSDs are basically the same except for the positions and values of some peaks on them. The PSD at $Re_j=3200$ is also characterized by its peaks, which are closer to the lower end of the particle size range in Figure 5.17 when compared to that in Figure 5.12. The different positions of peaks of the PSD should be due to the growth process since the other conditions in this case are the same with that in turbulent coagulation and nucleation processes except that growth process is introduced. With Re_j number increasing from 3200 to 4800, a new peak at around $1.5 \mu\text{m}$ appears on the new PSD. This is caused by the growth and coagulation processes as nucleation process forms much smaller particles rather than particles with diameter of $1.5 \mu\text{m}$, which is shown by the increase of average particle diameter with Re_j number increasing from 3200 to 4800 in Figure 5.18. However, as Re_j number increases from 4800 to 6400, the value of the peak at $1.5 \mu\text{m}$ decreases very slightly while the value of the peak at around $0.6 \mu\text{m}$ increases significantly, which may be due to the enhanced nucleation process as nucleation produces more particles with the smallest size. The value of the peak

at $0.6 \mu\text{m}$ increased sharply again with Re_j number increasing from 6400 to 12800, implying that nucleation process is further enhanced to be the dominant process.

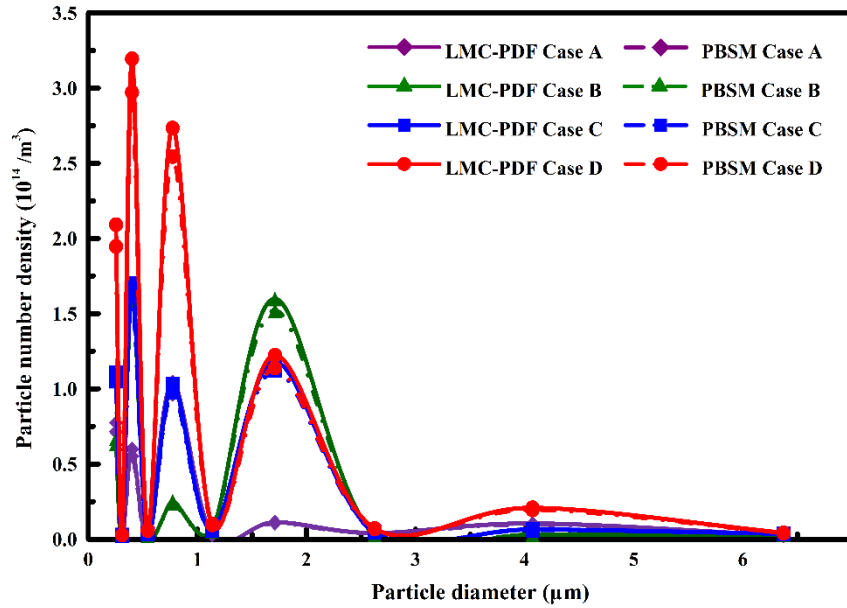


Figure 5.17 PSD for simultaneous coagulation, nucleation and growth in turbulent flows: Case A, $Re_j = 3200$; Case B, $Re_j = 4800$; Case C, $Re_j = 6400$; Case D, $Re_j = 12800$ (The PBSM results are obtained based on the method proposed by Hounslow (1988)) (Liu and Chan, 2016).

The average diameters of particles for different Re_j numbers are calculated in order to reveal the physical mechanism behind the change of the PSD. Figure 5.18 shows an increase in average diameter of particles for increasing Re_j number from 3200 to 4800. Whereas for Re_j number larger than 4800 (within these four studied Re_j numbers for this case), the average diameter of particles decreases with increasing Re_j number. Based on the average diameter of particles calculated from the obtained PSD, it can be concluded that, with increasing Re_j number from 4800 to 6400, the change of the peak at around $0.6 \mu\text{m}$ is due to pure nucleation as neither growth nor coagulation leads to the decrease in average diameter of particles. Comparing the case of turbulent coagulation and nucleation processes in Figure 5.13

with this case in Figure 5.18, it can be found that the particle number density of small particles increases with Re_j number in both of the two cases, which implies that nucleation, is the dominant process among the simultaneous processes in the present study.

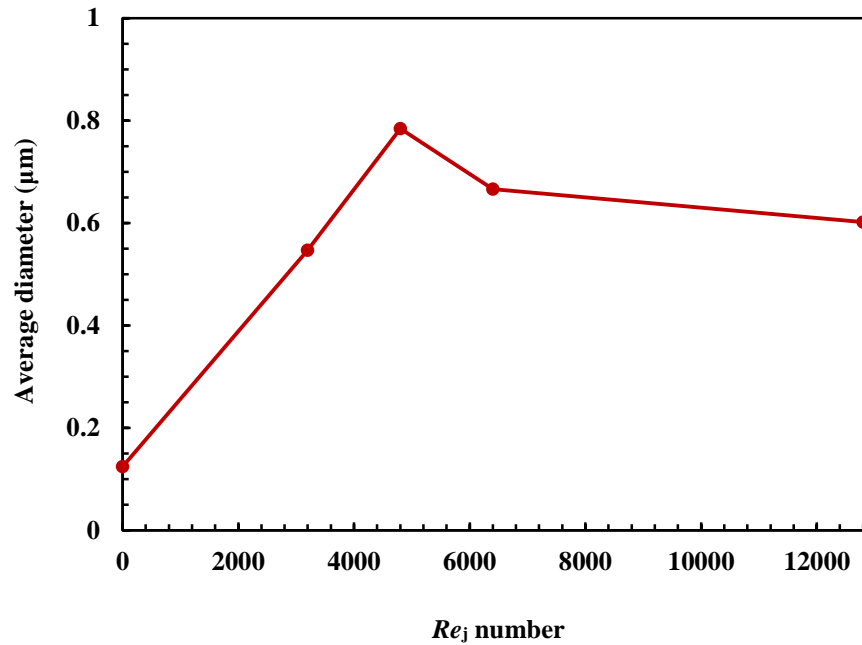


Figure 5.18 Average diameter of particles for simultaneous coagulation, nucleation and growth processes in turbulent flows (Liu and Chan, 2016).

Figure 5.19 shows the particle number density contour for simultaneous coagulation, nucleation and growth in turbulent flows. Consistent with the variation of average diameter of particles, the maxima of the particle number density contour also increases with increasing Re_j number from 3200 to 4800 and then decreases with Re_j number for larger than 4800. The variation of particle number density contour also verifies the effect of Re_j number on the competition between coagulation and nucleation. The dominant process changes from coagulation to nucleation with increasing Re_j number from 3200 to 12800 in the present study.

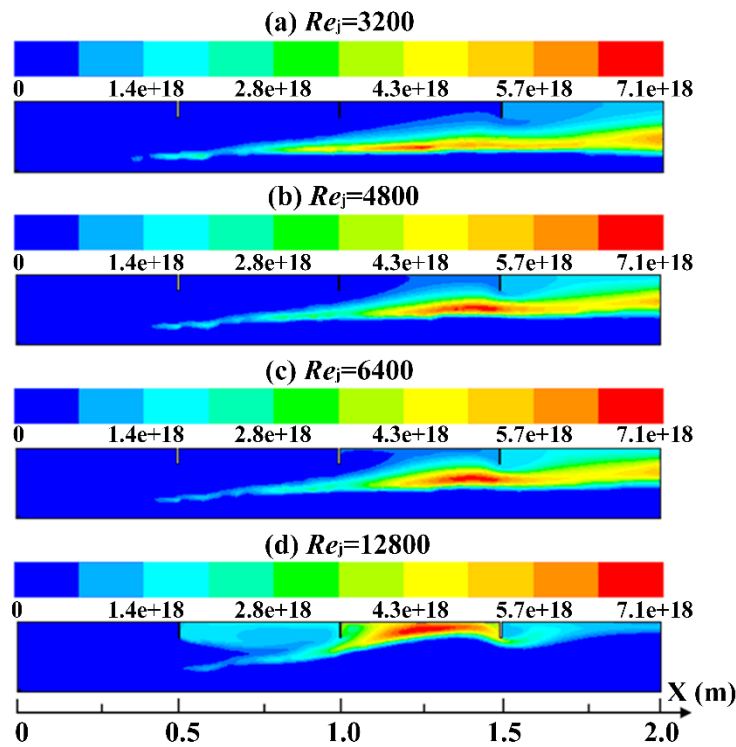


Figure 5.19 Particle number density (m^{-3}) contour for simultaneous coagulation, nucleation and growth in turbulent flows (Liu and Chan, 2016).

Comparing with the results in Figure 5.15, regions with high particle number density appear within the core of the jet in Figure 5.19(a) to (c), which may be due to the growth processes taking place in these regions. The regions with high particle number density regions in Figure 5.19(d), however, move from the core of the jet to the zone between the second and the third internals, and close to the wall of the aerosol reactor. This may be because this zone becomes a dead zone of flow and mixing for $Re_j=12800$, which leads to weakened coagulation process in this dead zone of flow and mixing.

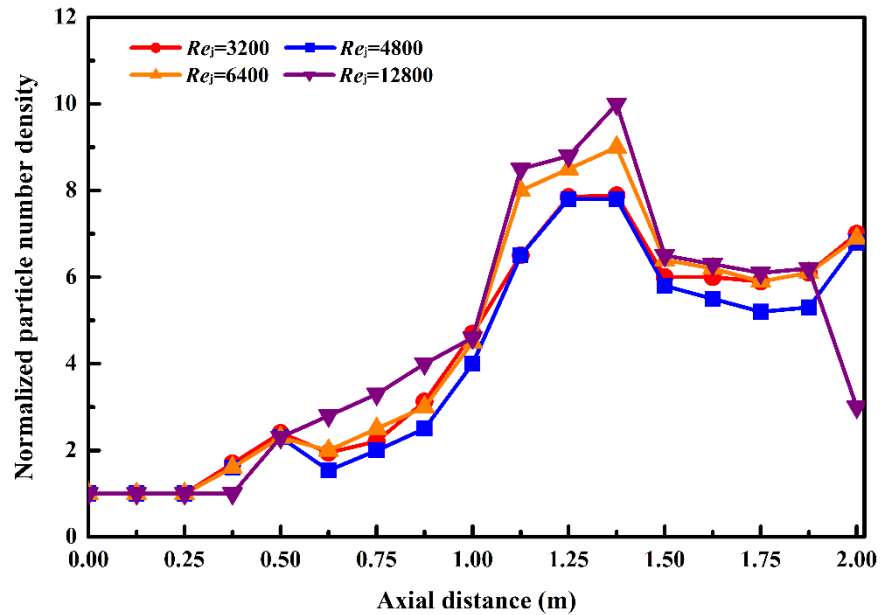


Figure 5.20 Normalized particle number density for simultaneous coagulation, nucleation and growth in turbulent flows (Liu and Chan, 2016).

Figure 5.20 presents the variation of normalized particle number density with axial distance. It can be seen that the variation of normalized particle number density is basically the same for all the four studied Re_j numbers despite small differences, which increases first until a peak appears between the second and the third partition of the aerosol reactor. Except for the case with Re_j number of 12800, the normalized particle number density after the peak decreases, and then basically remains stable with slight increase at the outlet of the aerosol reactor for all the other three cases. The variation of normalized particle number density for Re_j number ranging from 3200 to 6400 can be explained by the competition of multiple aerosol dynamic processes including coagulation, nucleation and growth. However, the particle number density at the peak is so high that coagulation process takes place, which reduces the particle number density to a basically dynamic equilibrium between the increasing factor (nucleation) and decreasing factor (coagulation) of particle number density. Although coagulation is not the dominant process in

the four studied cases, it is still shown in Fig. 5.20 that once the Re_j number is larger than 4800, the normalized particle number density increases due to the delay of turbulent mixing at high injection velocity (Garrick, 2015). As for the case with Re_j number of 12800, the low particle number density near the outlet of the aerosol reactor may be caused by the dead zone between the second and the third partitions of the aerosol reactor where those particles are trapped.

5.4.5 Computational Accuracy and Efficiency

The term “accuracy” here refers to the agreement between the numerical simulation results via the proposed coupled CFD-Monte Carlo method and the reference method (i.e. the PBSM method). The maximum relative error and normalized convergence time for different studied cases are shown in Table 5.2. It can be seen that for the same Re_j number, the maximum relative error only varies very slightly for different aerosol dynamic processes. With the Re_j number increasing from 3200 to 12800, however, the maximum relative error for any of the studied cases in Table 5.2 increases rapidly, which may be explained by the increasing turbulent fluctuations caused by the increasing Re_j number. The maximum relative error amongst all the studied cases is only 4.83%, which proves the high accuracy of this newly proposed and developed CFD-MC method. The normalized convergence time is used to represent the computational efficiency of the numerical simulation. It can be seen that for any fixed case amongst the studied cases in Table 5.2, the normalized convergence time only increases very slightly with increasing Re_j number. However, comparing different studied cases with the same Re_j number shows that the normalized convergence time increases significantly with the complexity of the studied cases. When Re_j number is 12800,

for instance, the normalized convergence time of pure coagulation process is about 1.10, which increases to 5.00 for coagulation and nucleation processes and to 11.25 for simultaneous coagulation, nucleation and growth processes, respectively. The variation of the normalized convergence time shows that the complexity of the studied cases has much greater influence on the computational efficiency than Re_j number, which may be because more computational time is needed for more complex aerosol dynamic processes in order to reach convergence. It can be also seen that although PBSM method needs a shorter normalized convergence time than the LMC-PDF method for the simple cases, almost the same normalized convergence time is needed for complex cases. Thus, this newly proposed and validated LMC-PDF provides an efficient but relatively simple algorithm.

Table 5.2 Maximum relative error and normalized convergence time for different studied cases (Liu and Chan, 2016).

Studied cases	Re_j	Maximum relative error, ε_{\max} (%)	Normalized convergence time of LMC-PDF	Normalized convergence time of PBSM
Coagulation	3200	1.00	1.00	0.75
	4800	3.00	1.08	0.88
	6400	4.10	1.08	0.88
	12800	4.60	1.10	1.00
Coagulation and nucleation	3200	1.00	4.50	4.00
	4800	2.90	4.50	4.00
	6400	4.30	4.63	4.25
	12800	4.80	5.00	5.00
Coagulation, nucleation and growth	3200	1.10	10.00	10.00
	4800	3.00	10.25	10.25
	6400	4.30	10.75	10.50
	12800	4.80	11.25	11.25

LMC-PDF: Lagrangian Monte Carlo-PDF method; PBSM: Population balance sectional method. The convergence time is normalized based on the ratio of any convergence time to the shortest convergence (i.e., the convergence time of turbulent coagulation for $Re_j = 3200$) in the present study.

5.4.6 Numerical Stability Analysis

The typical grid independence analysis is given in Table 5.3. For the relatively simple turbulent coagulation case ($Re_j=3200$), the normalized convergence time increases to more than nine times (i.e., from 1.00 to 9.36) with the number of grid cells increasing from 8112 to 22800 while the maximum relative error hardly changes (i.e., from 1.00% to 0.99%). For the relatively complex simultaneous case such as coagulation, nucleation and growth processes ($Re_j = 12800$), the normalized convergence time increases rapidly and drastically (i.e., from 11.25 to 112.50) with number of grid cells increasing-from 8112 to 22800 while the maximum relative error hardly changes (i.e., from 4.80% to 4.78%). So the grid cell independence can be confirmed from Table 5.3 and the optimal grid cells is selected to be 8112 in the present study.

Table 5.3 Typical grid cell independence analysis.

Selected cases	Number of grid cells	Maximum relative error, ε_{\max} (%)	Normalized convergence time
Turbulent Coagulation ($Re_j= 3200$)	8112	1.00	1.00
	12044	0.99	2.25
	15200	0.99	4.00
	22800	0.99	9.36
Coagulation nucleation and growth ($Re_j= 12800$)	8112	4.80	11.25
	12044	4.80	25.30
	15200	4.79	45.00
	22800	4.78	112.50

The normalized convergence time is defined by the ratio of any convergence time to the shortest convergence (i.e., the convergence time of turbulent coagulation for $Re_j = 3200$) in the present study.

Table 5.4 Typical analysis of the number of simulation particles per grid cell.

Selected cases	Number of simulation particles per grid cell	Maximum relative error, ε_{\max} (%)	Normalized convergence time
Turbulent Coagulation ($Re_j = 3200$)	20	2.00	0.80
	30	1.00	1.00
	60	0.99	4.50
	100	0.99	16.36
Coagulation nucleation and growth ($Re_j = 12800$)	20	4.90	10.90
	30	4.80	11.25
	60	4.79	52.80
	100	4.79	125.50

The normalized convergence time is defined by the ratio of any convergence time to the shortest convergence (i.e., the convergence time of turbulent coagulation for $Re_j = 3200$) in the present study. The total number of grid cells used is 8112.

The effect of the number of simulation particles per grid cell is shown in Table 5.4. Similar variations can be found in Table 5.4, the normalized convergence time becomes unacceptably high while the maximum relative error remains almost unchanged for the studied Re_j from 3200 to 12800 with the increasing number of simulation particles per grid cell. Hence, the number of simulation particles is set as 30 to strike a balance between the computational accuracy and time in the present study. The numerical stabilities can be well verified by the results presented in Tables 5.3 and 5.4 and the above discussions.

5.5 Summary

Typical simultaneous aerosol dynamic processes (i.e., coagulation, nucleation and growth) are widely encountered in turbulent flows. They are investigated with this newly proposed and developed Lagrangian PDF approach based CFD-Monte Carlo method. The effect of different Re_j numbers on

the interaction between turbulence and aerosol dynamics is fully studied. The results reveal the significant impact of Re_j on both single aerosol process (e.g. coagulation) and the competitive and simultaneous aerosol dynamic processes in turbulent flows.

This newly proposed and validated CFD-Monte Carlo/PDF method renders an efficient and accurate method to deal with the interaction between turbulence and aerosol dynamics by overcoming the closure problems. The full PSD of aerosol particles is accurately obtained. The enhancing effect of turbulence on coagulation is demonstrated by comparison of laminar coagulation and turbulent coagulation. Further study reveals the effect of turbulence on the PSDs for simultaneous aerosol dynamic processes and significant impact of turbulence on the final PSD of particles. For simultaneous complex aerosol dynamics in turbulent flows, turbulence plays an important role in-broadening the PSD. The coupled CFD-Monte Carlo/PDF method also shows excellent numerical stability according to typical grid cell independence analysis and typical analysis of the number of simulation particles per grid cell.

Chapter 6 Simulation of Aerosol Dynamics in Turbulent Reactive flows

6.1 Introduction

Combustion processes of the fossil fuels contain brief descriptions that convert the chemical energy into sensible energy in the products. The fossil fuels provide a major source of energy for miscellaneous applications ranging from household and industrial heating to power generation and metallurgy as well as combustion chamber in engine and propulsion systems (Kuo and Acharya, 2012). Turbulent reactive flows conditions are widely encountered in most practical combustion devices such as internal combustion (IC) engine and fluidized bed. The release of chemical energy involves radiative heat transfer (Modest, 2003) and pollutant emissions (Boushaki et al., 2016). Models accounting for all aspects of combustion devices ranging from gas turbines and IC engines to industrial furnaces are needed to meet the increasingly stricter emissions regulations from combustion devices and the higher combustion efficiency requirements. Thus, it is necessary to develop models with various physical sub-processes and detailed chemistry in combustion process to evaluate the performance of different combustion flows. Moreover, turbulence adds to the complexity required for modeling of combustion processes resulting from the turbulence chemistry interaction (TCI) and turbulence radiation interaction (TRI) (Mehta, 2008). The modeling of soot formation in turbulent reactive flows is the focus of this chapter.

A comprehensive modeling of turbulent reactive flows, including detailed chemistry, radiation and soot models with detailed closures for TCI and TRI is

presented in this chapter. This newly proposed and validated CFD-MC method (Liu and Chan, 2016) derived from the transported PDF approach coupling with PBE in Chapter 5 is used to simulate a turbulent non-premixed jet flame of methane. A time-dependent Reynolds-averaged Navier-Stokes (RANS) model is used in conjunction with the k - ϵ turbulence model as the CFD code to solve the turbulent combustion flow fields. One of the advantages of using the transported PDF approach is that the chemical reaction source, radiation emission and soot generation source terms appear in closed form (Akridis and Rigopoulos, 2015).

Both the kinetics of soot formation kinetics and the chemistry of combustion are taken into account in the numerical simulation. The classical combustion mechanism GRI 1.2 (Frenklach et al., 1995), which is still widely used today in combustion simulation (Akridis and Rigopoulos, 2015; Pant et al., 2016; Buchmayr et al., 2016). It is used to describe the combustion chemistry in the present study. The particle representations of mixture fraction, species, enthalpy and particle size distribution (PSD) are obtained with the Lagrangian Monte Carlo method. The turbulence-chemistry interaction (TCI) and turbulence-radiation interaction (TRI) are also considered to provide a better insight into soot dynamics in the turbulent non-premixed jet flame of methane. The transported PDF method is used to capture the TCI (as described by Lindstedt and Louloudi, 2005) and TRI (as described by Mehta et al., 2010). Temperature, mixture fraction and soot distribution are computed in both radial and axial direction. The numerical simulation results are then compared with the classical experimental results (Brookes and Moss, 1999) available in the literature.

6.2 Numerical Methodology

6.2.1 The CFD Code

The governing equations of the coupled fluid dynamics-aerosol dynamics in turbulent flows include the continuity, momentum equations (i.e., Navier-Stokes equations) and energy equation as well as the discretized population balance equation (PBE) of particle number density given in Chapter 5.

The one-point, one-time composition PDF approach is coupled with a time-dependent RANS code with a k - ε turbulence model. The CFD code is discretized with a finite volume scheme. The averaged momentum and k - ε turbulence equations are solved in a two-dimensional axisymmetric domain. The boundary conditions and the geometry of the domain are set by following the experiment of Brookes and Moss (1999). The mean velocity field and the turbulence time scale are provided to the scalar PDF by the CFD code while the micro mixing term is obtained via the estimation of ensemble mean scalars in each computational cell of the computational grid. In order to reduce the statistical error, a time-averaging method is further used. The following equations show the k - ε turbulence model in Cartesian tensor notation form and repeated indices mean summation (Akridis and Rigopoulos, 2015):

$$\frac{\partial}{\partial t} [\bar{\rho}k] + \frac{\partial}{\partial x_j} [\bar{\rho}\tilde{u}_j k] = \frac{\partial}{\partial x_j} \left[\left(\mu + \frac{\mu_t}{\sigma_k} \right) \frac{\partial k}{\partial x_j} \right] + G_t - \bar{\rho}\varepsilon \quad (6-1)$$

$$\frac{\partial}{\partial t} [\bar{\rho}\varepsilon] + \frac{\partial}{\partial x_j} [\bar{\rho}\tilde{u}_j \varepsilon] = \frac{\partial}{\partial x_j} \left[\left(\mu + \frac{\mu_t}{\sigma_\varepsilon} \right) \frac{\partial \varepsilon}{\partial x_j} \right] + \frac{\varepsilon}{k} [C_{\varepsilon 1} G_t - C_{\varepsilon 2} \bar{\rho}\varepsilon] \quad (6-2)$$

where Reynolds averaged quantities are shown with a bar on top while Favre averaged quantities are shown with a tilde on top. ρ is the mixture density, μ is the molecular viscosity of the mixture, μ_t is the turbulent viscosity, σ is the turbulent Prandtl number and G_t is the generation rate of turbulent kinetic energy. The default standard model constants are modified and listed in Table 6.1, where the constant $C_{\varepsilon 2}$ is changed from 1.92 to 1.8 for correction in order to obtain better prediction of turbulence (Akridis and Rigopoulos, 2015).

Table 6.1 Model constants for the k - ε turbulence model

C_μ	$C_{\varepsilon 1}$	$C_{\varepsilon 2}$	σ_k	σ_ε
0.09	1.44	1.8	1.0	1.3

6.2.2 The Lagrangian PDF Method

In the Lagrangian PDF method, stochastic particles are used to represent the quantities including mixture fraction, species mass fraction, total enthalpy and the particle size distribution (PSD). Although deterministic techniques such as finite difference or finite volume schemes can be used to solve the transported PDF equations, the computational time increases exponentially (Leonard and Dai, 1994) and becomes intractable for transported PDF equations with a large number of scalars of interest. Thus, stochastic algorithm i.e., Monte Carlo algorithm is used to solve the transported PDF equations, in which the computational time only increases linearly with the number of independent scalars (Leonard and Dai, 1994).

The motion equation of notional particles in physical domain is similar to Equation (5-18) and is shown as below:

$$dX^{(P)}(t) = [\tilde{u} + \frac{\nabla \Gamma_T}{\bar{\rho}}]_{(P)} dt + [2 \frac{\Gamma_T}{\bar{\rho}}]^{1/2}_{(P)} dW \quad (6-3)$$

where W is an isotropic vector Wiener process, Γ_T is the turbulent diffusivity, X is the position and \tilde{u} is the Favre averaged velocity of notional particles, ρ is the mixture density. The subscript P represents a single Lagrangian notional particle.

The Euclidean minimum spanning tree (EMST) model (Subramaniam and Pope, 1998) is chosen as the mixing model, in which the variation of particle composition is obtained by computing the interaction of particles along the edges of Euclidean minimum spanning trees based on ensembles of particles in the composition space. The complete equation of Lagrangian particles in scalar space is shown as below:

$$dX_a^{(P)}(t) = \Phi_{mix}^{(P)} + S_a^{(P)} dt + \delta_{rad} \frac{\dot{Q}_{rad}^{(P)}}{\rho^{(P)}} dt \quad (6-4)$$

where $\Phi_{mix}^{(P)}$ in the first term is the micro-mixing term, $S_a^{(P)}$ in the second term is the chemical reaction source term, $\dot{Q}_{rad}^{(P)}$ in the last term is the radiation by emission source term, δ_{rad} is Kronecker delta function, $\rho^{(P)}$ is the density of particles on the right-hand side of Equation (6-4). With the assumption of equal diffusivities for all scalars, the micro-mixing term is assumed the same for all scalars. As more than one mechanism appear in Equation (6-4), a time step operator splitting method (Liu and Chan, 2017) is used to compute different mechanisms one by one. The Lagrangian Monte Carlo method is used to obtain the ensemble mean scalars by

time averaging and then input the results to the CFD (RANS) code to close other terms. The detailed procedures of one loop of Monte Carlo simulation can be found in Chapter 5.

6.2.3 Particle Tracking Algorithm

The particle tracking algorithm of Subramaniam and Haworth (2000) is adopted here. For a particle, j in cell, i , let the minimum time of particle, j to intersect a face of cell, i be $t_{i,j}$, and the time step be Δt . If $t_{i,j} > \Delta t$, the particle, j stays in cell, i at the end of one time step. If $t_{i,j} < \Delta t$, the particle, j is moved to the face intersection point of cell, i at the end of one time step, and its cell pointer is updated and time-step is decremented by $t_{i,j}$. Repeat the tracking particles until the remaining time of all the particles becomes zero. The total number of particles in a cell is maintained within a prescribed range by cloning or destroying particles if a lower bound or upper bound is reached. The time step, Δt_i in a cell is chosen to be the minimum time for satisfying the turbulence time scale and CFL conditions in Chapter 5. Moreover, the final time step Δt is chosen to be the minimum amongst all the cells in the computational domain as follows:

$$\Delta t = \min \{ \Delta t_i, i=1, 2, \dots, n \} \quad (6-5)$$

where n is the total number of cells in the computational domain.

6.2.4 Estimation of Mean Field

Estimates of mean quantities in PDF/Monte-Carlo simulation are obtained by means of a particle-cloud-in-cell method and the Favre average of a quantity, Q in a cell, c is shown as follows (Mehta, 2008):

$$\tilde{Q}_c = \frac{\sum_{p \in c} m_p Q_p}{\sum_{p \in c} m_p} \quad (6-6)$$

where m_p is the mass of particle p and Q_p is the quantity carried by particle, p in a cell, c . The summation is carried out over all the particles in cell, c .

6.2.5 Soot Model

An acetylene based soot model with only growth/oxidation and nucleation processes (Akridis and Rigopoulos, 2015; Liu et al., 2003) is used in the present study. According to the experimental results of the same jet flame (Brookes and Moss, 1999), the soot volume concentration in the jet flame is only of magnitude order 10^{-7} , in which the coagulation events of soot particles hardly take place. Thus, coagulation process is not included in the soot model here. An important assumption is that the shape of soot particles is considered spherical. Nucleation and surface growth rate are assumed the first-order dependent on acetylene concentration while the oxidation rate is a function of molecular oxygen and hydroxyl concentrations, which is as follows (Akridis and Rigopoulos, 2015):

Nucleation rate:

$$NU_0 = \frac{2N_A k_n(T)[C_2H_2]}{C_{\min}} \quad (6-7)$$

Growth rate:

$$G_{SG} = \frac{2k_{HW}(T)[C_2H_2]A_s}{\rho_s} \quad (6-8)$$

Oxidation rates:

$$G_{O_2} = \frac{120 \left[\frac{k_a X_{O_2} \chi_1}{1 + k_z X_{O_2}} + k_b X_{O_2} (1 - \chi_1) \right] A_s}{\rho_s} \quad (6-9a)$$

$$G_{OH} = \frac{\frac{167 X_{OH}}{\sqrt{T}} A_s}{\rho_s} \quad (6-9b)$$

where k is reaction rate constant, a function of temperature. C_{\min} is the minimum number of carbon atoms that is needed to produce an incipient soot particle, which is assumed 700 here with an initial soot diameter of 2.4 nm (Liu et al., 2003). N_A is the Avogadro constant. The density of soot, ρ_s is assumed 1800 kg/m³. A_s is the surface area of soot particles. X is the mole fraction of a species. Other constants are set according to Hall et al. (1997) and Liu et al. (2003).

6.2.6 Radiation Model

An optically thin radiation model is chosen as the radiation model in the-present study where the gaseous phase and soot particles only emit radiation but do not re-absorb any energy. The radiation coefficients are calculated according to Akridis and Rigopoulos (2015). The radiation model with CH₄, H₂O, CO and CO₂ taken into account is shown as follows:

$$\dot{Q}_{\text{rad}} = 4\sigma(T^4 - T_b^4) \sum_{i=1}^{N_{sp}} p_i a_{p,i} + 4\sigma f_v (T^5 - T_b^5) \quad (6-10)$$

where σ is the Stefan-Boltzmann constant, T_b is the background temperature of the experiment and N_{sp} is the total number of species. p_i is the partial pressure and $a_{p,i}$ is the Planck mean absorption coefficient of species, i . f_v is the volume fraction of soot particles (Lindstedt and Louloudi, 2005).

6.3 Numerical Simulation Setup

The configuration of the combustor in the numerical simulation is shown in Figure 6.1, which is a piloted non-premixed combustor in the experiment of Brookes and Moss (1999). The combustor consists of a jet burner with internal diameter of 4.07 mm having a jet flame at 20.3 m/s. The Reynolds number of the jet at exit is 5000. An air co-flow is supplied at 0.5 m/s surrounding the central fuel tube. A Pyrex tube with internal diameter of 156 mm and height of 600 mm is used to confine the jet flame. The outlet of the burner is at 290 K and atmospheric pressure. The detailed jet burner parameters of the studied combustor is shown in Table 6.2.

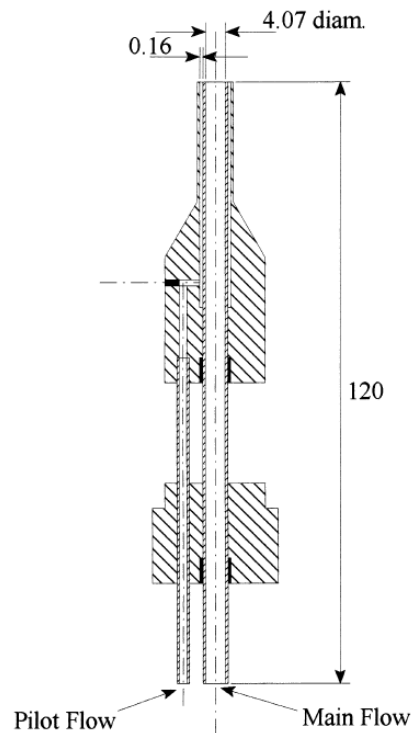


Figure 6.1 Jet burner configuration of the combustor (Brookes and Moss, 1999).

Table 6.2 Jet burner parameters and conditions for the studied combustor.

Absolute pressure	1 atm
Velocity of methane	20.3 m/s
Flow rate of methane	10.3 g/min
Inlet temperature of methane	290 K
Velocity of air	0.5 m/s
Flow rate of air	708 g/min
Inlet temperature of air	290 K
Reynolds number of jet flame exit, Re_j	5000
Internal diameter of the burner	4.07 mm
Internal diameter of confined Pyrex tube	156 mm
Number of notional particles per cell	50

The computational domain is shown in Figure 6.2, which is a two-dimensional (2D) axisymmetric jet domain. The non-uniform 2D grid is generated with 160 points in the axial direction and 100 points in the radial direction. There are totally 5542 cells and 5597 nodes in the grid. The number of notional particles used for each cell is 50 to compute the scalar variables in the Lagrangian PDF method. In addition, the scalar variables are time averaged with 3000 iterations in order to reduce the statistical error. The mixture fraction is defined as the mass fraction of species originating from the fuel stream amongst all the species, which is used to characterize the instantaneous thermochemical state of the non-premixed turbulent combustion in the present study.

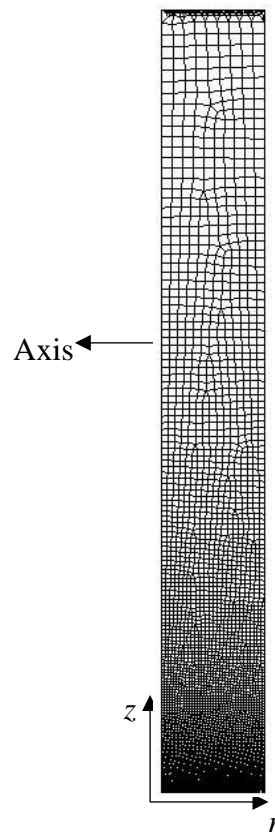


Figure 6.2 The computational grid used in the numerical simulation of an axisymmetric combustor.

The mixture fraction is defined as a normalized ratio by the following newly added Equation (6-11), measuring the fuel/oxidizer ratio (Turns, 2011):

$$Z = \frac{sY_F - Y_{O^+} (Y_O)^0}{sY_F + (Y_O)^0} \quad (6-11)$$

where Z is the mixture fraction, Y_F is the molecular fraction of fuel in the mixture, Y_O is the molecular fraction of oxygen in the mixture, $(Y_O)^0$ is the initial molecular fraction of fuel, s is the molecular ratio of fuel to oxidizer (i.e., air).

6.4 Results and Discussion

6.4.1 Axial and Radial Jet Temperature Variations of the Studied Combustor

In the present studied axisymmetric combustor, the jet temperature varies in both radial and axial directions. It can be seen that axial distance is actually the height above the inlet of the burner as shown in Figure 6.2. The simulation results are compared with the classical experimental results available from Brookes and Moss (1999). Figure 6.3 shows the axial jet temperature variation at the centerline of the studied combustor for $Re_j = 5000$. The numerical results agree well with the experimental results. With increasing axial distance from zero (the inlet of the burner) to 0.6 m, the sampling position in the jet flame moves from the inner layer to the outer layer of methane flame, which corresponds to the increase of jet temperature axially.

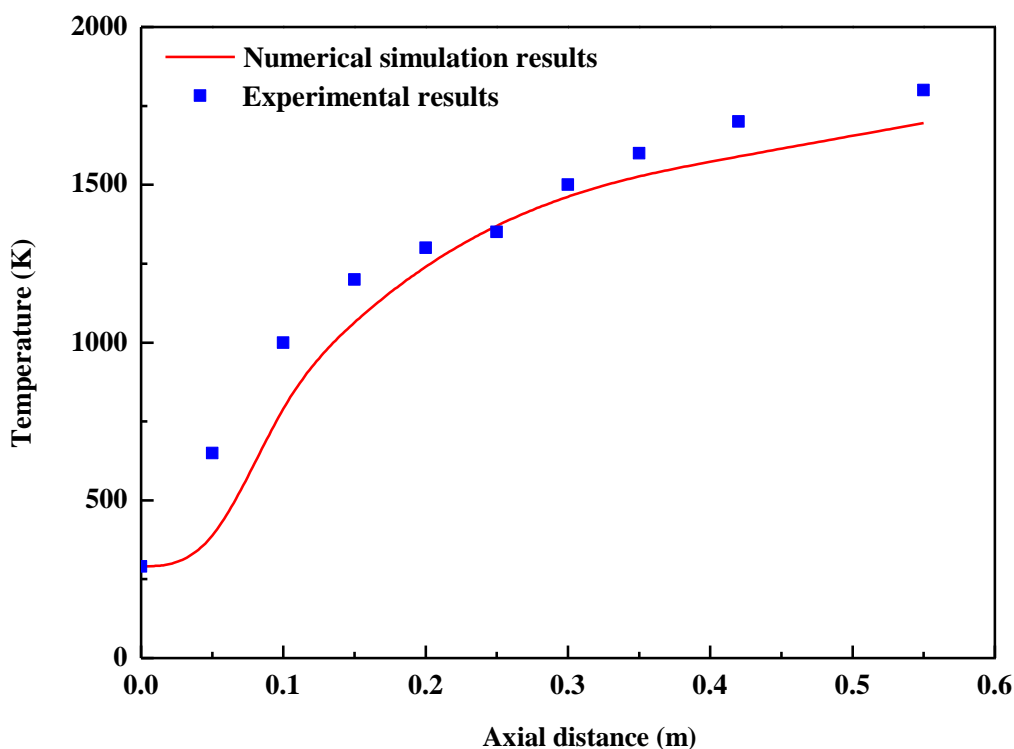


Figure 6.3 Axial jet temperature variation at the centerline of the studied combustor for $Re_j=5000$ (The experimental results are obtained from Brookes and Moss (1999)).

Figure 6.4 shows the radial jet temperature variation at the axial distance of 250 mm for the studied combustor at $Re_j = 5000$. Excellent agreement can be observed between the jet temperature from numerical simulation and that from the experiment of Brookes and Moss (1999). The radial distance of zero corresponds to the centerline of the jet flame. With increasing radial distance from zero to 0.06 m, the sampling position moves from the centerline of jet flame to the outer layer of the methane flame and finally out of the flame region. Thus, the radial jet temperature in Figure 6.4 increases first and then decreases when the sampling position moves out of the flame region. It is obvious that the simulation results obtained by the proposed coupled CFD-Monte Carlo method accurately capture the radial jet temperature variation in the combustor.

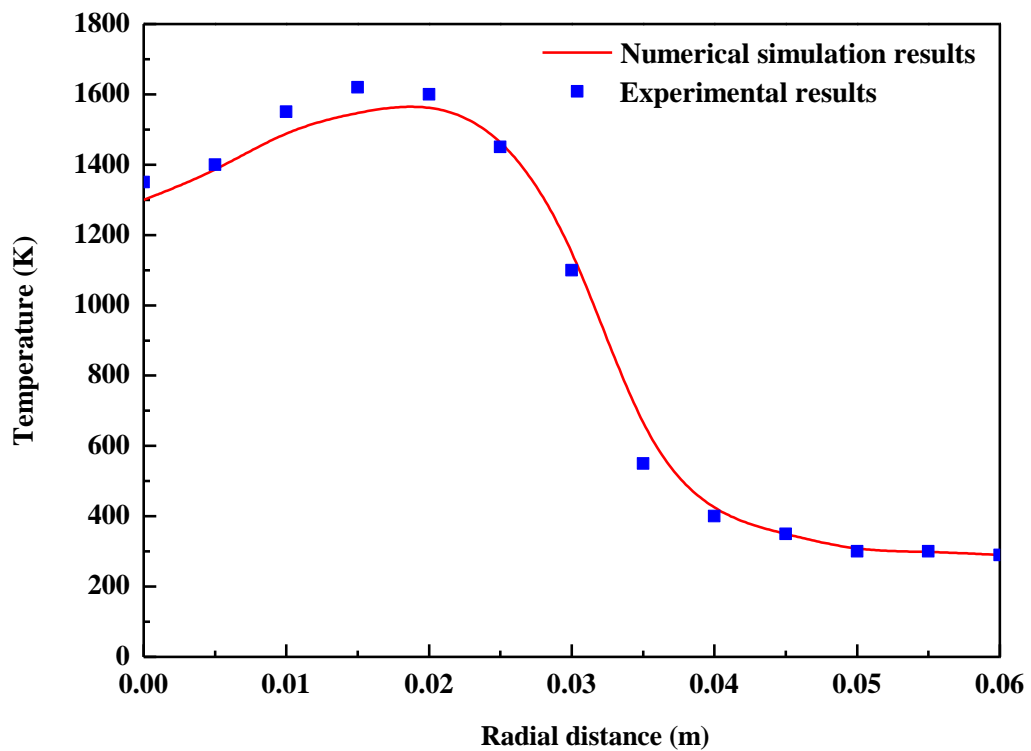


Figure 6.4 Radial jet temperature variation at the axial distance of 250 mm for the studied combustor at $Re_j=5000$ (The experimental results are obtained from Brookes and Moss (1999)).

The radial jet temperature variation at the axial distance of 350 mm for the studied combustor at $Re_j = 5000$ is shown in Figure 6.5. A higher jet temperature at radial distance of zero can be observed in Figure 6.4 than that in Figure 6.5, which reflects the effect of axial distance on jet temperature. With increasing radial distance from 0 to 0.06 m, the temperature first increases slightly then decreases gradually to about 290 K (i.e., ambient temperature), which is consistent with the results in Figure 6.4. The temperatures predicted by numerical simulation agree well with the classical experimental results available from Brookes and Moss (1999).

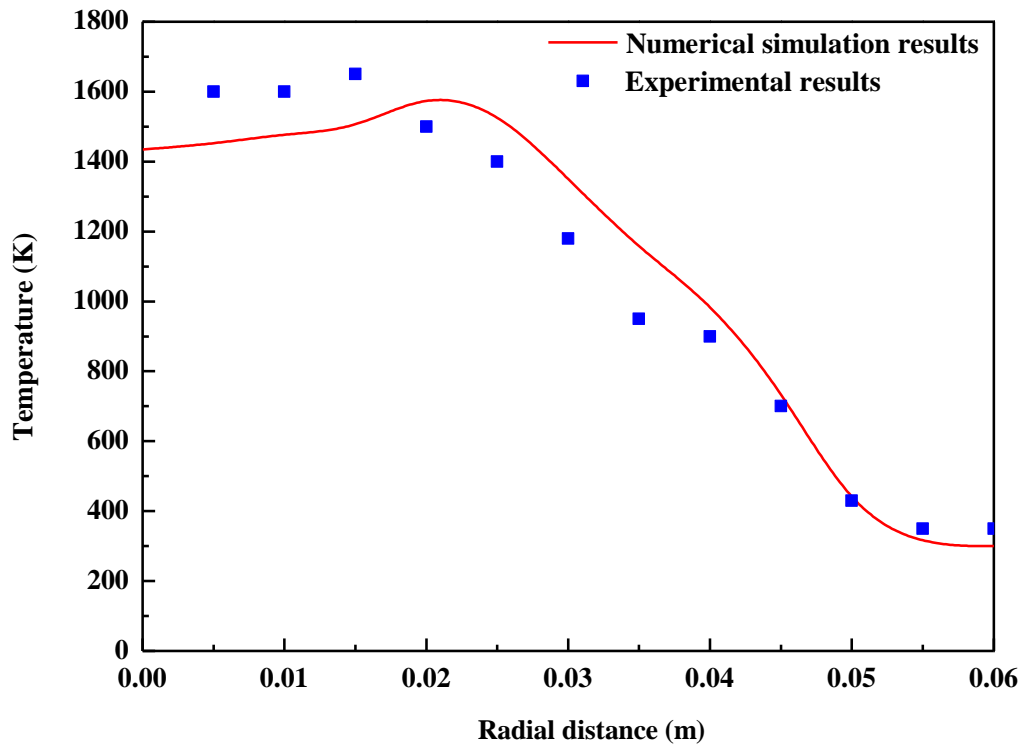


Figure 6.5 Radial jet temperature variation at the axial distance of 350 mm for the studied combustor at $Re_j = 5000$ (The experimental results are obtained from Brookes and Moss (1999)).

6.4.2 Axial and Radial Jet Mixture Fraction Variations of the Studied Combustor

Figure 6.6 shows the axial jet mixture fraction variation at the centerline of the studied combustor for $Re_j = 5000$. Comparing the numerical results obtained by this newly proposed coupled CFD-Monte Carlo method and the experimental results (Brookes and Moss), a good agreement can be found. With increasing axial distance from zero (i.e., the outlet of the burner centerline) to 0.6 m, the mixture fraction decreases rapidly, indicating the processing of the non-premixed methane combustion.

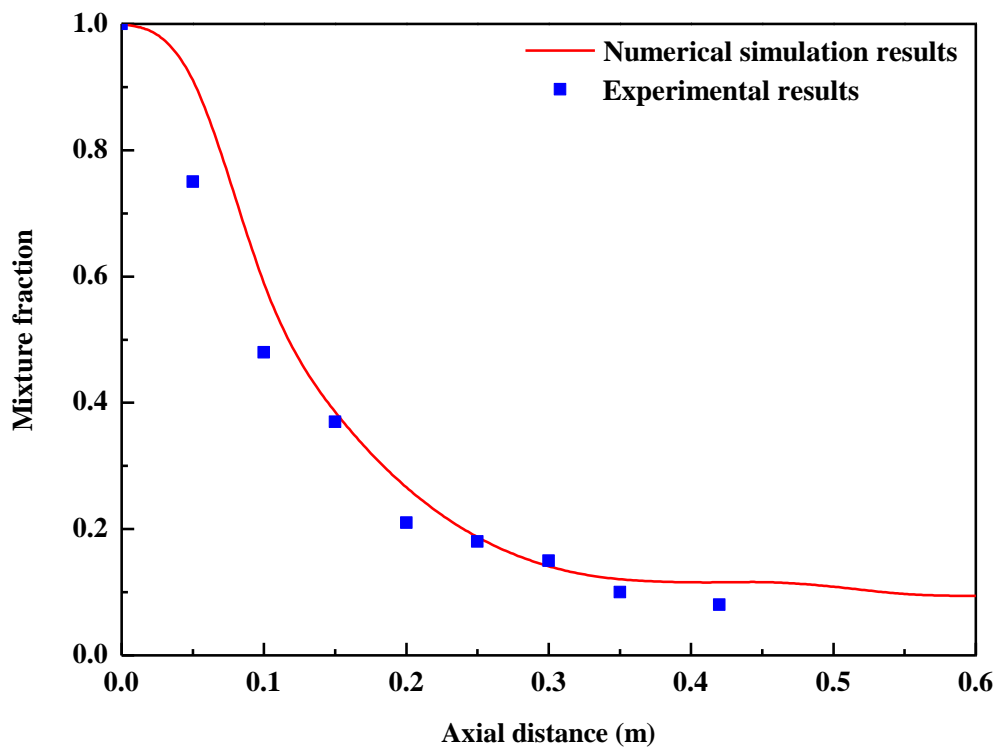


Figure 6.6 Axial jet mixture fraction variation at the centerline of the studied combustor for $Re_j = 5000$ (The experimental results are obtained from Brookes and Moss (1999)).

The radial jet mixture fraction variation at the axial distance of 250 mm for the studied combustor at $Re_j = 5000$ is shown in Figure 6.7. The numerical results obtained agree well with the experimental results despite slight over prediction of mixture fraction. However, the discrepancy at 0.005 m in the radial distance may be caused by the instability and stagnation region of jet flame. With increasing radial distance from 0 to 0.04 mm, the mixture fraction in Figure 6.8 decreases gradually to almost zero at 0.04 mm in the radial direction.

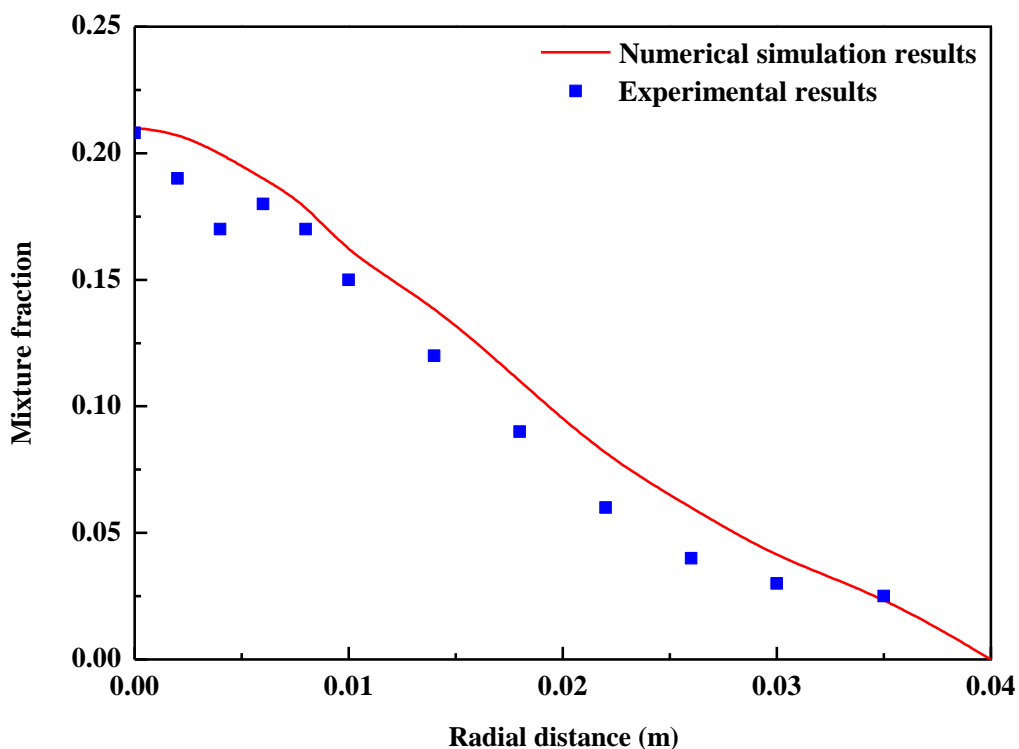


Figure 6.7 Radial jet mixture fraction variation at the axial distance of 250 mm for the studied combustor at $Re_j = 5000$ (The experimental results are obtained from Brookes and Moss (1999)).

Figure 6.8 shows the radial jet mixture fraction variation at the axial distance of 350 mm for the studied combustor at $Re_j = 5000$. Good agreement can be obtained between the numerical results and the experimental results except for the mixture fraction at the radial distance of 0 mm (i.e., centerline of jet flame) which may be caused due to the instability and stagnation region of jet flame. Comparing the mixture fraction in Figures 6.7 and 6.8, it can be found that the mixture fraction at 250 mm in the axial direction is higher than that at 350 mm in the axial direction if radial distance is less than 0.03 m. With increasing radial distance from 0 to 0.04 mm, the mixture fraction in Figure 6.8 decreases gradually to a stable value at 0.04 mm in the radial direction. The higher mixture fraction at 0.04 m in Figure 6.8

implies that the configuration of jet flame at different heights above the burner are different.

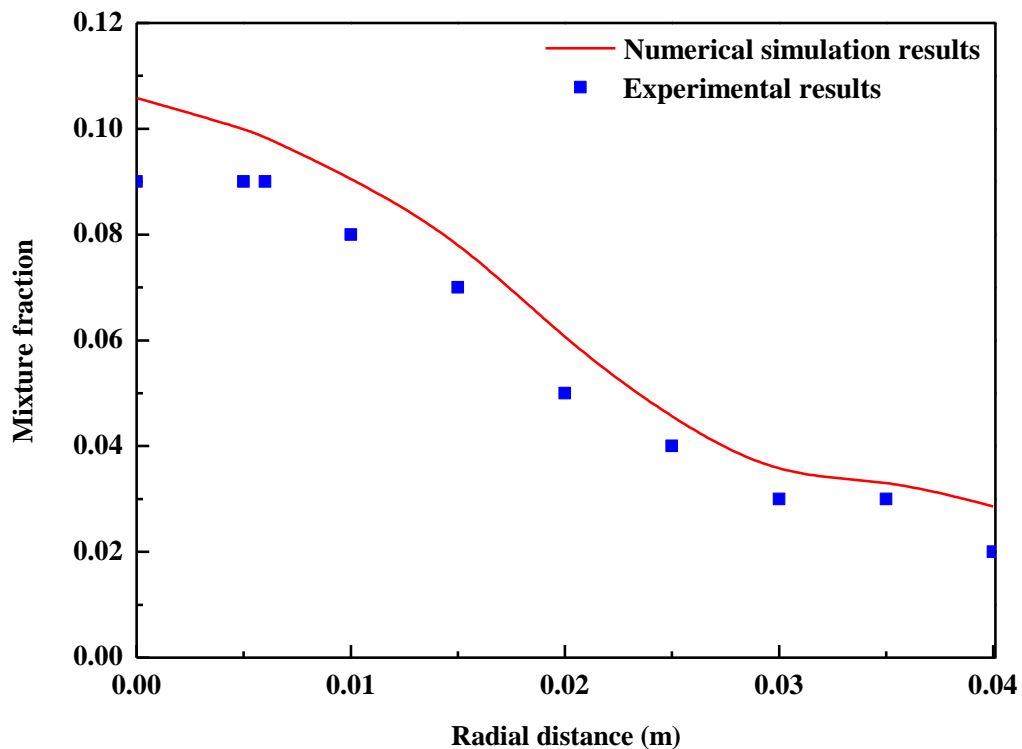


Figure 6.8 Radial jet mixture fraction variation at the axial distance of 350 mm for the studied combustor at $Re_j=5000$ (The experimental results are obtained from Brookes and Moss (1999)).

6.4.3 Axial and Radial Jet Soot Volume Fraction Variations of the Studied Combustor

Figure 6.9 shows the axial jet soot volume fraction variation at the centerline of the studied combustor for $Re_j = 5000$. It can be seen that the numerical results provide excellent prediction of the soot volume fraction compared with the experimental results (Brookes and Moss, 1999). The slight under prediction at the axial distance of 0.55 m may be due to the instability and stagnation region of jet flame.

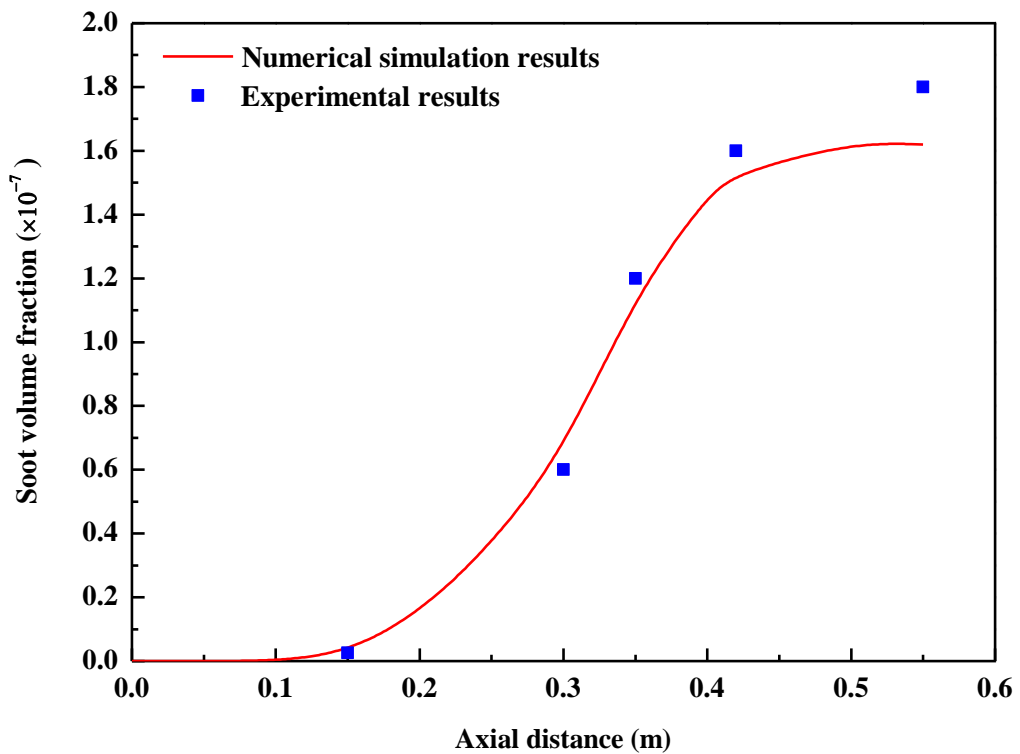


Figure 6.9 Axial jet soot volume fraction variation at the centerline of the studied combustor for $Re_j = 5000$ (The experimental results are obtained from Brookes and Moss (1999)).

Comparing Figure 6.9 with Figure 6.3, it can be seen that as jet temperature increases with the axial distance, the soot volume fraction increases accordingly, implying that high jet temperature is conducive to the formation of soot particles. This can be explained from the Equations (6.7) to (6.9). As jet temperature increases, the aerosol dynamic processes including nucleation, growth and oxidation are all accelerated, resulting in the increase of soot volume fraction in the axial direction.

Figure 6.10 shows the radial jet soot volume fraction variation at the axial distance of 350 mm for the studied combustor at $Re_j = 5000$. An excellent agreement between the numerical results and experimental results can be obtained in Figure 6.10. With increasing radial distance from 0 to 0.05 m, an obvious gradient of soot volume fraction can be observed. Comparing Figure 6.10 with Figure 6.5,

it can be found that the higher soot volume fraction corresponds to higher jet temperature. As jet temperature decreases in the radial direction, the soot volume fraction decreases accordingly. The numerical simulation with the newly proposed coupled CFD-Monte Carlo method demonstrates high capability in capturing the variation of soot volume fraction in the non-premixed turbulent jet flame of methane.

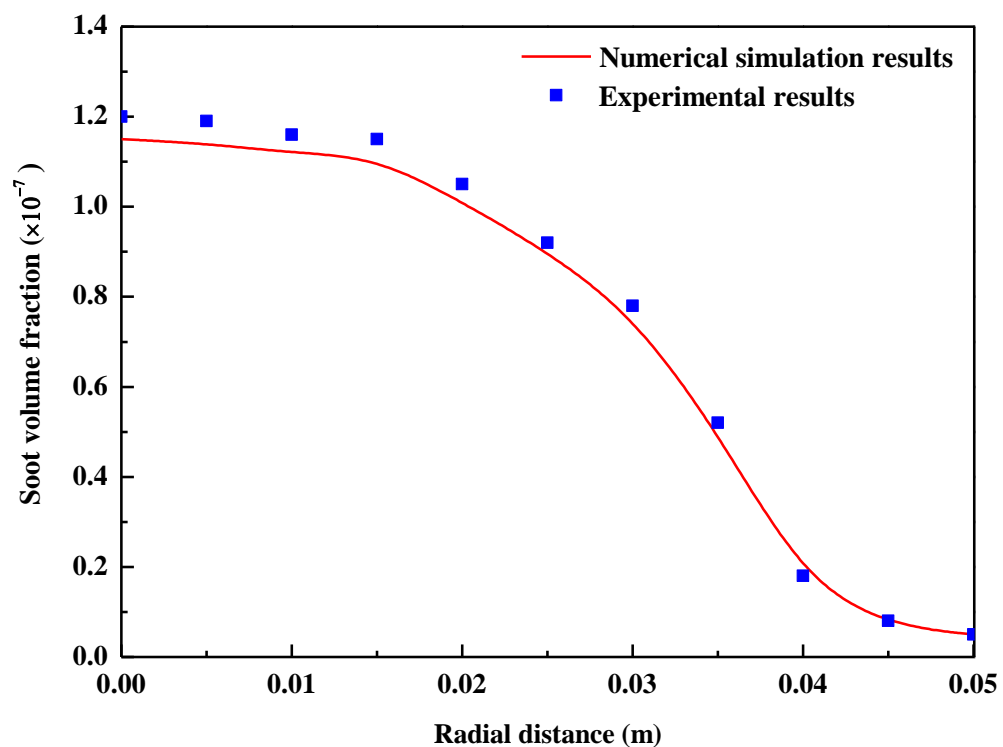


Figure 6.10 Radial jet soot volume fraction variation at the axial distance of 350 mm for the studied combustor at $Re_j=5000$ (The experimental results are obtained from Brookes and Moss (1999)).

A similar radial jet soot volume fraction variation at the axial distance of 425 mm above the burner for the studied combustor at $Re_j=5000$ in Figure 6.11. With the increase of radial distance, the soot volume fraction decreases obviously. An excellent agreement can be obtained between the numerical results and the experimental results of Brooke and Moss (1999). The variation of jet soot volume

fraction in Figure 6.11 can also be explained by the decrease of temperature in the radial direction of jet flame, which is consistent with the soot kinetics described by Equations (6.7) to (6.9). Combining the results in Figures 6.9 to 6.11, it can be concluded that the variation of jet temperature directly affects the variation of jet soot volume fraction.

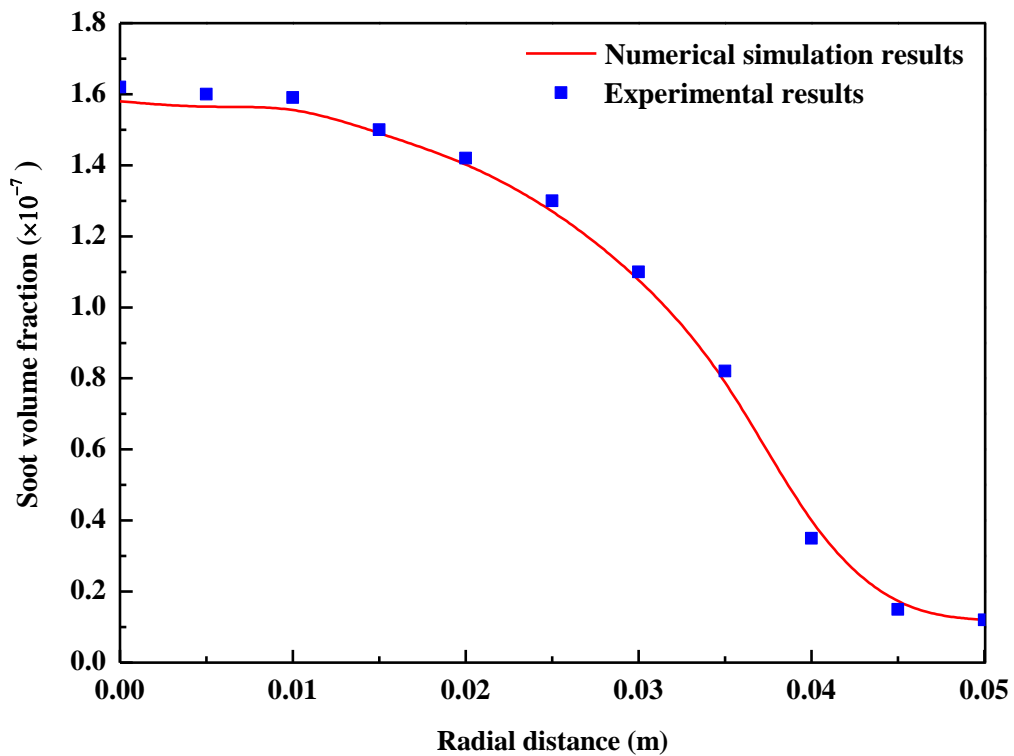


Figure 6.11 Radial jet soot volume fraction variation at the axial distance of 425 mm for the studied combustor at $Re_j = 5000$ (The experimental results are obtained from Brookes and Moss (1999)).

6.4.4 Soot Size Distribution

Figure 6.12 shows the jet soot particle size distribution (PSD) at the axial distances of 138 mm and 308 mm. The PSD results obtained with the coupled CFD-Monte Carlo method proposed in the present study are compared with those obtained by Akridis and Rigopoulos (2015).

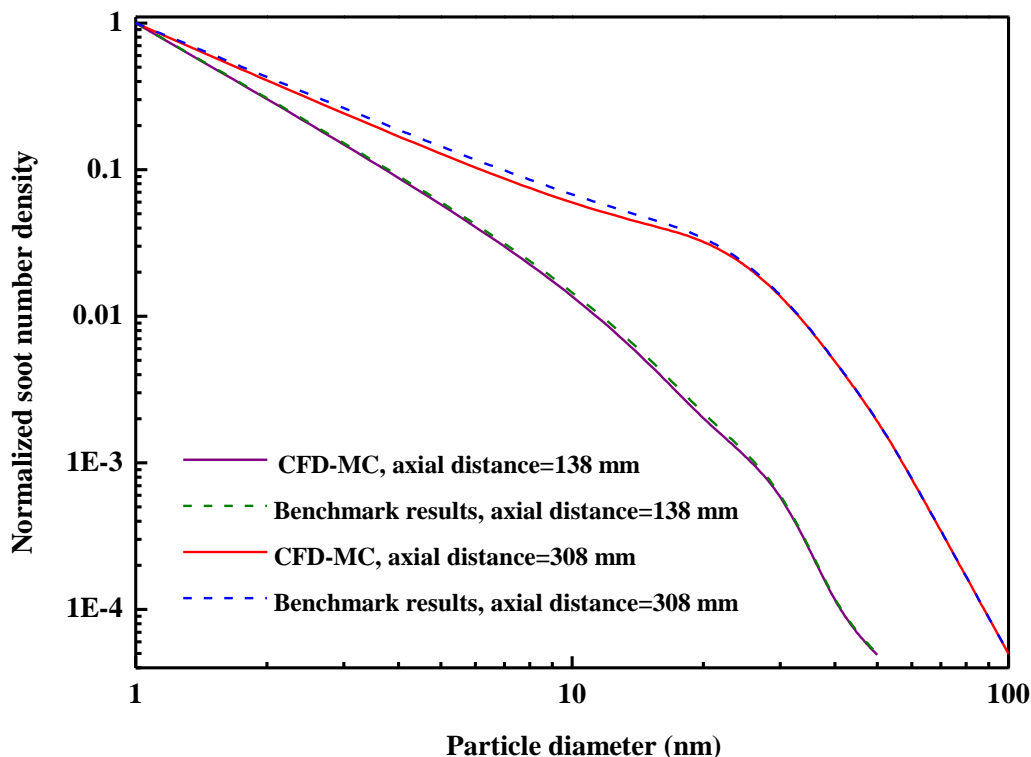


Figure 6.12 PSD of jet soot particles at the axial distances of 138 mm and 308 mm (The benchmark results are obtained from Akridis and Rigopoulos (2015)).

The PSD results are presented in a logarithmic coordinate system. The definition of normalized particle number density can be found in Equation (5.23). An excellent agreement is found between the numerical results obtained with the coupled CFD-Monte Carlo method and those obtained by Akridis and Rigopoulos (2015), which again validates this proposed method in predicting the PSD of soot particles in turbulent reactive flows. The PSD at 308 mm in the axial direction is higher than the PSD at 138 mm in the axial direction, which is consistent with the results in Figure 6.9, i.e., a higher axial distance corresponds to a higher soot volume fraction. It can be observed that the soot particles cover a size spectrum ranging from 1 nm to 100 nm. With the increase of soot particle diameter, the normalized particle number density decreases obviously. A wider PSD can be observed at 308 mm in the axial direction than that at 138 mm in Figure 6.12.

Comparing Figure 6.12 with Figure 6.3 implies that temperature has vital effect on soot formation as temperature directly affects the soot formation processes such as nucleation and growth.

6.4.5 Relative Error Analysis

Table 6.3 shows the relative error analysis between the present numerical and experimental results (Brookes and Moss, 1999). It can be seen from Table 6.3 that the maximum relative error mainly appears at the physical boundary locations. For example, at axial distance of 0.05 m, the maximum relative error of the temperature is as high as 50.0%, which may be due to the experimental uncertainties in the boundary conditions as similar discrepancy can also be found in the numerical simulation results by Akridis and Rigopoulos (2015) which are also compared to the experiments by Brookes and Moss (1999). Akridis and Rigopoulos (2015) also pointed out the fact of experimental uncertainties. However, the particle size distribution (PSD) obtained via the present coupled CFD-Monte Carlo method is found to have the smallest relative error (less than 0.1%), which indicates the high capability of this method in obtaining accurate PSD of soot particles in turbulent non-premixed flames.

Table 6.3 Relative error analysis between the present numerical and experimental results (Brookes and Moss, 1999).

	Temperature		Mixture fraction		Soot volume fraction		PSD
	Position (m)	Error (%)	Position (m)	Error (%)	Position (m)	Error (%)	Value (%)
Axial direction	0.05	50.0	0.05	16.7	0.55	11.1	N/A
Radial direction	0.35	14.0	0.05	15.0	0.05	4.3	<0.1

Note: The “relative error” is defined by Equation (4.18). “Position” is used to represent the axial or radial distance of the sampling point at which the corresponding relative error appears. Particle size distribution (PSD) is taken in the radial direction in the experiments (Brookes and Moss, 1999), but no PSD results are given in the axial direction. N/A: not applicable.

6.5 Summary

The newly proposed and validated CFD-Monte Carlo method in Chapter 5 is used together with the soot and radiation models to investigate aerosol dynamics i.e., soot dynamics in non-premixed turbulent reactive flows. The variation of jet temperature, and mixture fraction and soot volume fractions in both axial and radial direction are obtained and compared with experimental results of Brookes and Moss (1999). Excellent agreement is obtained between the numerical results and the experimental results, which validates the reliability and capability of this proposed method. Moreover, the PSDs of jet soot particles at different axial distances predicted by this newly modified and developed CFD-Monte Carlo method agree very well with the results of Akridis and Rigopoulos (2015). The numerical results demonstrate that temperature is of great significance to soot dynamics and high temperature is conducive to the formation of soot particles in the present studied low sooty flame. However, considering the low soot volume

concentration in the studied flame (< 0.2 ppm), it should not be interpreted to be of any generality in other turbulent sooty flames. Relative error analysis of the numerical simulation results shows that the highest discrepancy with the experimental results (Brookes and Moss, 1999) appears at boundary locations in the jet flame, which may be due to the uncertainties of the experimental boundary conditions. However, the present modified CFD-Monte Carlo method still demonstrates high capability of obtaining PSD with high accuracy.

Chapter 7 Conclusions and Recommendations for Future Work

7.1 Review of the Present Research

This thesis is mainly focused on the numerical simulation of multi-scale and multi-dimensional turbulent reactive flows with the newly proposed and developed computational fluid dynamics (CFD) based Monte Carlo method. The research work in this thesis can be divided into three major parts:

In the first part of the current research, a newly proposed and developed stochastically weighted operator splitting Monte Carlo (SWOSMC) method is used for the simulation of complex aerosol dynamics. Stochastically weighted particle method is coupled with operator splitting method to formulate the SWOSMC method for the numerical simulation of particle-fluid systems undergoing the complex simultaneous aerosol dynamic processes. The studied cases cover all the typical aerosol dynamic processes including coagulation, nucleation, growth and condensation. This proposed SWOSMC method is first validated by comparing its numerical simulation results of constant rate coagulation and linear rate condensation with the corresponding analytical solutions. Coagulation and nucleation cases are further studied and the results show excellent agreement with the sectional method. This newly proposed SWOSMC method has also demonstrated its high numerical simulation capability when used to deal with simultaneous aerosol dynamic processes including coagulation, nucleation and condensation.

The second part of the current research is the development of a CFD-population balance modelling (PBM) method for simulating aerosol dynamics in turbulent flows. The validated SWOSMC method in Chapter 4 is further modified and coupled with CFD method based on the transported probability density function (PDF) approach. The formulated CFD-Monte Carlo method allows investigating the interaction between turbulence and aerosol dynamics, and incorporating individual aerosol dynamic kernels as well as obtaining full particle size distribution (PSD). Several typical cases of aerosol dynamic processes including turbulent coagulation, nucleation and growth processes are studied and compared to the sectional method with excellent agreement. Coagulation in both laminar and turbulent flows is simulated and compared to demonstrate the effect of turbulence on aerosol dynamics. The effect of different jet Reynolds (Re_j) numbers on aerosol dynamics in turbulent flows is fully investigated for each of the studied cases.

The third part of the current research is the simulation of aerosol dynamics in turbulent reactive flows by using the newly proposed and developed CFD-PBM method together with GRI 1.2 combustion chemistry and soot kinetics models. Soot formation in turbulent non-premixed flames of methane as well as its interaction with radiation is studied. The particle representations of mixture fraction, species, enthalpy and distribution of soot number density are solved using the Lagrangian particle method. Both turbulence-radiation and turbulence-chemistry interactions are considered.

7.2 Main Conclusions of the Thesis

7.2.1 Conclusions of the Zero-Dimensional Monte Carlo Simulation of Aerosol Dynamics

The simulation results of this newly proposed and developed stochastically weighted operator splitting Monte Carlo (SWOSMC) method are fully validated with corresponding analytical solutions (Ramabhadran et al., 1976; Maisels et al., 2004) and the sectional method (Prakash et al., 2003) for various aerosol dynamic processes (i.e., coagulation, condensation and nucleation) in different flow regimes. Excellent results are obtained from this new SWOSMC method. For just an average number of numerical particles 2000 used, the maximum relative error is less than 1%.

With the increase of the complexity from the studied Case 1 to Case 4, an increasing computational time is obviously required for using a fixed number of numerical particles. However, for a certain case, the computational error is inversely proportional to the square root of the total number of the numerical particles (Oran et al., 1998). It also suggests that further optimization of this newly proposed SWOSMC method is needed in order to improve the computational efficiency and accuracy for the complex particle-fluid systems. Compared with the sectional method (Prakash et al., 2003), this newly proposed SWOSMC method takes a much shorter computational time even with the largest number of numerical particles in the studied Case 3.

There always exists conflicts and tradeoffs between computational cost (i.e., computational time, computer memory, etc.) and accuracy for Monte Carlo based

methods for the numerical simulation of complex aerosol dynamics. However, this validated SWOSMC method has clearly demonstrated a promising high capacity to obtain higher computational accuracy and efficiency with a much shorter computational time than the sectional method for the same typical studied case.

7.2.2 Conclusions of the CFD-PBM Simulation of Aerosol Dynamics in Turbulent Flows

Typical simultaneous aerosol dynamic processes including coagulation, nucleation and growth are widely encountered in turbulent flows. They are investigated with this newly proposed and developed Lagrangian particle method based CFD-Monte Carlo method.

The effect of different Re_j numbers on the interaction between turbulence and aerosol dynamics is fully investigated. The results reveal the significant impact of Re_j on both single aerosol process (e.g. pure coagulation) and the competitive and simultaneous aerosol dynamics processes in turbulent flows. The newly proposed CFD-Monte Carlo/PDF method renders an efficient method to deal with the interaction between turbulence and aerosol dynamics by overcoming the closure problems.

The full particle size distribution (PSD) of aerosol particles is readily obtained. The enhancing effect of turbulence on coagulation is demonstrated by comparison of laminar coagulation and turbulent coagulation. Further investigation of the effect of turbulence on the PSDs of simultaneous aerosol dynamics reveals the competition between aerosol dynamic processes, which also has significant impact on the final

PSD of particles. For simultaneous complex aerosol dynamics in turbulent flows, turbulence has an effect of broadening the PSD. The coupled CFD-Monte Carlo/PDF method also shows excellent numerical stability according to typical grid cell independence analysis and typical analysis of the number of simulation particles per grid cell.

7.2.3 Conclusions of Simulation of Aerosol Dynamics in Turbulent Reactive Flows

The variation of jet temperature, and mixture and soot volume fractions in both axial and radial directions of a turbulent non-premixed jet flame of methane are obtained and compared with the classical experimental results available from Brookes and Moss (1999). Excellent agreement is found between the numerical and the experimental results, which validates the high reliability of this newly proposed and developed CFD-PBM method coupled with combustion chemistry and soot kinetics models.

Moreover, the PSDs of jet soot particles at different axial distances predicted by the newly proposed and developed CFD-Monte Carlo method agree very well with the results obtained from Akridis and Rigopoulos (2015). The numerical results demonstrate clearly that temperature is of great significance to soot dynamics and high temperature is conducive to the formation of soot particles for this special low sooty flame. Relative error analysis of the numerical results shows that the highest discrepancy with the experimental results (Brookes and Moss, 1999) appears at boundary locations in the jet flame, which may be due to the uncertainties of the experimental boundary conditions. However, the present modified CFD-Monte Carlo method still demonstrates high capability of obtaining PSD with high accuracy.

7.3 Recommendations for Future Work

The thesis presents the numerical simulation of typical and complex aerosol dynamic processes ranging from zero-dimensional complex aerosol dynamics to multi-dimensional aerosol dynamics in reactive flows with consideration of the effect of turbulence. Based on the coupled stochastic weighted particle and operator splitting methods, the aim of the thesis is to propose a robust and highly efficient CFD-Monte Carlo method for solving complex aerosol dynamics in multi-scale systems. Multi-dimensional aerosol dynamics and transport as well as interaction with turbulence and reactive flows are fully investigated in the thesis with this newly proposed and developed SWOSMC and CFD-Monte Carlo methods. However, further research work is still recommended to overcome the limitations of these proposed numerical methods and optimizations are also needed to make the methods more robust and powerful.

7.3.1 Limitations of the Current Research

The limitations of this newly proposed and developed SWOSMC and CFD-Monte Carlo methods are as follows:

1. The two-dimensional axisymmetric grid cells are used for the numerical simulation of aerosol dynamics in turbulent reactive flow. However, for practical applications, aerosol reactors with arbitrary configuration are widely encountered. Thus, a three-dimensional simulation can be performed to further validate this newly proposed and developed method, subject to the relevant and appropriate experimental datasets

available and accessible in literature for the study on the complexity of aerosol processes and phenomena.

2. Parallel computing is not implemented in the present study. Considering the stochastic motion of large number of Monte Carlo numerical particles, a parallel computing approach may further improve the computational efficiency and accuracy of the numerical simulation with this newly proposed and developed method; and
3. Due to the fact that very few analytical solutions and experimental data are available for complex aerosol dynamics in literature especially for aerosol dynamic processes in turbulent reactive flows, the validation of this newly proposed and developed methods is therefore limited to mainly comparing with other numerical methods. Only for very limited cases, validation can be performed by comparing with the analytical/experimental results available in literature.

7.3.2 Recommendations for Future Work

Considering the above-mentioned limitations on the present study, recommendations are made as follows:

1. Three-dimensionalization. The programs of this newly proposed methods can be modified and optimized so that they can be fully applied to three-dimensional simulations of complex aerosol dynamics in aerosol reactors or other fluid-particle systems with arbitrary configurations for validation, but subject to the relevant availability and accessibility of the

three-dimensional experimental datasets in literature. Moreover, with appropriate modifications to this proposed and developed CFD-Monte Carlo method, the large eddy simulation (LES) model can be applied to provide better insight into the interaction between aerosol dynamics and turbulence;

2. Parallelization. In order to reduce computational cost (i.e., computational time, computer memory, etc.) and increase computational efficiency, parallelization of the source codes of these proposed and developed numerical methods is required which is consistent with the three-dimensionalization of these methods. It is because three-dimensional simulation with more complicated turbulence models requires higher computational cost.
3. Experimental investigations. More results from the related experiments are needed in order to provide more reliable experimental data for the numerical validation. Individually designed experiments are necessary to obtain first-hand reliable results and validate these proposed and developed numerical methods.

Appendices

A.1 Coagulation Process

Coagulation process is a binary particle event, which means that two smaller particles collide and coalesce to form a larger particle. The colliding particles are reasonably assumed to be a spherical particle according to the kinetic molecular dynamics (Mitchelle and Frenklach, 2003; Mehta et al., 2010). Coagulation can be modelled in three flow regimes according to different Kn numbers (Kandlikar et al., 2005).

If $Kn \gg 1$, the free molecular regime coagulation kernel is applicable, which is as follows:

$$K(u, v) = \left(\frac{6}{\pi} \right)^{\frac{2}{3}} \left(\frac{\pi k_B T_K}{2\rho} \right)^{\frac{1}{2}} \left(\frac{1}{u} + \frac{1}{v} \right)^{\frac{1}{2}} \left(u^{\frac{1}{3}} + v^{\frac{1}{3}} \right)^2 \quad (\text{A-1})$$

If $Kn \ll 1$, the continuous regime coagulation kernel is applicable, which is as follows:

$$K(u, v) = 2k_B T_K / 3\mu_{\text{air}} [2 + (v/u)^{1/3} + (u/v)^{1/3}] \quad (\text{A-2})$$

If $10^{-3} \ll Kn \ll 10^3$, the transition regime coagulation kernel is applicable, which is the harmonic mean of the limit values as follows:

$$K(u, v) = K_c K_{fm} / (K_c + K_{fm}) \quad (\text{A-3})$$

where $K(u, v)$ is the coagulation kernel, K_c and K_{fm} are the coagulation kernels at continuous regime and free molecular regime, respectively. Other parameters have the same physical meanings as mentioned in Chapter 4.

A.2 Nucleation Process

Nucleation a single particle event, which generates the smallest size particles in soot formation. The general equation of nucleation can be written as follows (Kazakov and Frenklach, 1998):

$$\frac{dN_0}{dt} = R_0 - G_0 - k_s s_0 N_{g0} / \Delta m \quad (\text{A-4})$$

where N_{g0} is the number density of newly generated smallest size particles, R_0 is the chemical rate that creates the smallest size particles, G_0 is the reduction rate of the smallest size particles by coagulation. The last term on the right-hand side of Equation (A-4) is the reduction rate of the smallest size particles by surface reaction where k_s is the reaction rate per unit area, s_0 is the surface area of the smallest size particles and Δm is the change during a single reaction event.

A.3 Surface Reactions in Soot Formation

The soot surface reactions using the Hydrogen-abstraction-Carbon-addition mechanism is shown as follows (Frenklach and Wang, 1994; Wang et al., 1996):



The surface growth is assumed to occur due to the reactions of C₂H₂ with surface radicals, and condensation of polyaromatic hydrocarbon on the particle surface and surface reactions with O₂ and OH (Mehta, 2008). Another assumption is that all soot particles are assumed to be spherical one (Akridis and Rigopoulos, 2015).

A.4 Soot Formation Models

A.4.1 The One-Step Soot Formation Model

The one-step soot formation model was proposed by Khan and Greeves (1974), which solves the following transport equation of soot mass fraction:

$$\frac{\partial}{\partial t} (\rho Y_{\text{soot}}) + \nabla \cdot (\rho \vec{v} Y_{\text{soot}}) = \nabla \cdot \left(\frac{\mu_t}{\sigma_{\text{soot}}} \nabla Y_{\text{soot}} \right) + R_{\text{soot}} \quad (\text{A-12})$$

where Y_{soot} is soot mass fraction, σ_{soot} is turbulent Prandtl number for soot transport, R_{soot} is the net rate of soot generation (kg/m³·s), which equals to the balance between soot formation, $R_{\text{soot, form}}$ and soot combustion, $R_{\text{soot, combst}}$.

$R_{\text{soot, form}}$ is calculated using an empirical rate equation as follows:

$$R_{\text{soot, form}} = C_s p_{\text{fuel}} \phi_{\text{combst}}^r e^{(-E_a/RT)} \quad (\text{A-13})$$

where C_s is soot formation constant (kg/N·m·s), p_{fuel} is fuel partial pressure (Pa), ϕ_{combst} is equivalence ratio, r is equivalence ratio exponent, E_a/R is activation temperature, T is the temperature.

The rate of soot combustion, $R_{\text{soot, combst}}$ is calculated as follows:

$$R_{\text{soot, combst}} = \min\left[A_{\text{soot}} \rho Y_{\text{soot}} \frac{\varepsilon}{k}, A_{\text{soot}} \rho \left(\frac{Y_{\text{ox}}}{\nu_{\text{soot}}}\right) \left(\frac{Y_{\text{soot}} \nu_{\text{soot}}}{Y_{\text{soot}} \nu_{\text{soot}} + Y_{\text{fuel}} \nu_{\text{fuel}}}\right) \frac{\varepsilon}{k}\right] \quad (\text{A-14})$$

where A_{soot} is constant in the Magnussen model, Y_{ox} and Y_{fuel} are mass fractions of oxidiser and fuel, respectively. ν_{soot} and ν_{fuel} are mass stoichiometries for soot and fuel combustion, respectively.

A.4.2 The Two-Step Soot Formation Model

The two-step soot formation model proposed by Tesner (1971) is used to predict the generation of radical nuclei and then computes the formation of soot on these nuclei (Vela, 2009). The transport of soot mass fraction in Equation (A-12) is solved with the following transport equation of the normalized radical nuclei concentration:

$$\frac{\partial}{\partial t} (\rho b^*_{\text{nuc}}) + \nabla \cdot (\rho \vec{v} b^*_{\text{nuc}}) = \nabla \cdot \left(\frac{\mu_t}{\sigma_{\text{nuc}}} \nabla b^*_{\text{nuc}} \right) + R^*_{\text{nuc}} \quad (\text{A-15})$$

where b^*_{nuc} is the normalized radical nuclei concentration ($\text{particle} \times 10^{-15} / \text{kg}$), σ_{nuc} is the turbulent Prandtl number for nuclei transport and R^*_{nuc} is the normalized net rate of nuclei generation ($\text{particle} \times 10^{-15} / \text{m}^3 \cdot \text{s}$) (Patki et al., 2014).

A.4.2.1 Net Rate of Soot Generation

The rates of nuclei and soot generation in both Equations (A-12) and (A-15) are the net rates that involve a balance between formation rate, $R_{\text{soot, form}}$ and combustion rate $R_{\text{soot, combst}}$ (Heravi et al., 2010). The rate of soot combustion in two-

step model is calculated similarly to the one-step model (Equation (A-14)), while the rate of soot formation is calculated as follows:

$$R_{\text{soot, form}} = m_p(\alpha - \beta N_{\text{soot}})c_{\text{nuc}} \quad (\text{A-16})$$

where m_p is the average mass of soot particle (kg), N_{soot} is the soot particle concentration, c_{nuc} is the concentration radical nuclei (/m³), α and β are the empirical constants.

A.4.2.2 Net Rate of Nuclei Generation

The net rate of nuclei generation is given by the balance of nuclei formation rate, $R_{\text{nuc,form}}^*$ (particles $\times 10^{-15}$ /m³-s) and combustion rate, $R_{\text{nuc,combst}}^*$ (particles $\times 10^{-15}$ /m³-s) (Peglow et al., 2006):

$$R_{\text{nuc}}^* = R_{\text{nuc,form}}^* - R_{\text{nuc,combst}}^* \quad (\text{A-17})$$

In two-step model, the rates of nuclei formation and combustion are calculated as follows (Patki et al., 2014):

$$R_{\text{nuc,form}}^* = a_0^* c_{\text{fuel}} e^{(-E_a/RT)} + (f-g)_{\text{soot}} c_{\text{nuc}}^* - g_0 c_{\text{nuc}}^* N_{\text{soot}} \quad (\text{A-18})$$

where c_{nuc}^* is the normalized nuclei concentration, a_0^* is pre-exponential rate constant, c_{fuel} is fuel concentration (kg/m³), $(f-g)_{\text{soot}}$ is the linear branching-termination coefficient (s⁻¹), g_0 is the linear termination term of soot particles (m³/particle-s) (Patki et al., 2014).

The rate of the combustion of nuclei is regarded as the linear function of the rate of soot combustion $R_{\text{soot,combst}}$ in Equation (A-14):

$$R_{\text{nuc, combst}}^* = R_{\text{soot, combst}} \frac{b_{\text{nuc}}^*}{Y_{\text{soot}}} \quad (\text{A-19})$$

where b_{nuc}^* is the normalized radical nuclei concentration ($\text{particle} \times 10^{-15}/\text{kg}$) and Y_{soot} is soot mass fraction.

A.4.3 The Moss-Brookes Model

Both the transport equations of normalized radical nuclei concentration, b_{nuc}^* and soot mass fraction, Y_{soot} are solved in the Moss-Brookes soot formation model (Brookes and Moss, 1999), which are shown as follows:

$$\frac{\partial}{\partial t} (\rho Y_{\text{soot}}) + \nabla \cdot (\rho \vec{v} Y_{\text{soot}}) = \nabla \cdot \left(\frac{\mu_t}{\sigma_{\text{soot}}} \nabla Y_{\text{soot}} \right) + \frac{dM}{dt} \quad (\text{A-20})$$

$$\frac{\partial}{\partial t} (\rho b_{\text{nuc}}^*) + \nabla \cdot (\rho \vec{v} b_{\text{nuc}}^*) = \nabla \cdot \left(\frac{\mu_t}{\sigma_{\text{nuc}}} \nabla b_{\text{nuc}}^* \right) + \frac{1}{N_{\text{norm}}} \frac{dN}{dt} \quad (\text{A-21})$$

where M is soot mass concentration, N is soot particle number density and $N_{\text{norm}} = 10^{15}$ particles.

The instantaneous generation rate of soot particles due to nucleation and free molecular coagulation, is shown as follows:

$$\frac{dN}{dt} = C_{\alpha} N_A (X_{\text{prec}} P / RT)^l \exp\left(-\frac{T_{\alpha}}{T}\right) - C_{\beta} (-24RT / \rho_{\text{soot}} N_A)^{1/2} d_p^{1/2} N^2 \quad (\text{A-22})$$

where C_{α} , C_{β} and l are dimensionless constants of the model, N_A is Avogadro number, X_{prec} is the mole concentration of soot precursor, ρ_{soot} is soot mass density, d_p is the mean diameter of soot particles and T_{α} is the activation temperature for nucleation reaction.

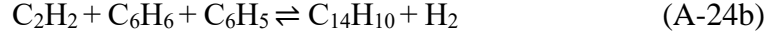
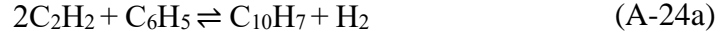
The source term of soot formation process is shown as follows:

$$\begin{aligned} \frac{dM}{dt} = & M_P C_\alpha (X_{\text{prec}} P / RT)^l \exp\left(-\frac{T_\alpha}{T}\right) \\ & + C_\gamma (X_{\text{sgs}} P / RT)^m \exp\left(-\frac{T_\gamma}{T}\right) [(\pi N)^{1/3} (6M / \rho_{\text{soot}})^{2/3}]^n \\ & - C_{\text{oxid}} C_\omega \eta_{\text{coll}} \left(\frac{X_{\text{OH}} P}{RT}\right) \sqrt{T} (\pi N)^{1/3} (6M / \rho_{\text{soot}})^{2/3} \end{aligned} \quad (\text{A-23})$$

The terms on the right-hand side of Equation (A-23) are nucleation, surface growth and oxidation terms, respectively. C_γ , C_{oxid} , C_ω , m and n are also dimensionless constants. M_P is the mass of an incipient soot particle, X_{sgs} is the mole fraction of the species participating surface growth process, M is the total source term due to all the aerosol dynamic processes. The set of constants in the Moss-Brookes model for methane flame is given (Brookes and Moss, 1999) as: $C_\alpha = 54 \text{ s}^{-1}$ (soot inception rate constant), $C_\beta = 1.0$ (coagulation rate constant), $C_\gamma = 11700 \text{ kg} \cdot \text{m} \cdot \text{kmol}^{-1} \cdot \text{s}^{-1}$ (scaling factor of surface growth rate), $C_\omega = 105.8125 \text{ kg} \cdot \text{m} \cdot \text{kmol}^{-1} \cdot \text{K}^{-1/2} \cdot \text{s}^{-1}$, $C_{\text{oxid}} = 0.015$ (scaling parameter of oxidation rate), $T_\gamma = 12100 \text{ K}$ (activation temperature of surface growth reaction) and $\eta_{\text{coll}} = 0.04$ (collision efficiency). The closure of the source terms in the above equations (A-20) to (A-23) can be found in Brookes and Moss (1999).

A.4.4 The Moss-Brookes-Hall Model

The Moss-Brookes model proposed for methane flames has been extended to Moss-Brookes-Hall model for higher hydrocarbon fuels by Hall et al., (1997) and Wen et al., (2003) based on the work of Lee et al., (1962). The soot inception mechanism developed by Hall et al., (1997) is as follows:



Based on the laminar methane flame data (Hall et al., 1997), the inception rate of soot particles is expressed as the generation rate of species C_{10}H_7 and $\text{C}_{14}\text{H}_{10}$ multiplied by eight as follows:

$$\begin{aligned} \left(\frac{dN}{dt}\right)_{\text{inception}} = & 8C_{\alpha,1}[\rho^2 \left(\frac{Y_{\text{C}_2\text{H}_2}}{W_{\text{C}_2\text{H}_2}}\right)^2 \frac{Y_{\text{C}_6\text{H}_5}W_{\text{H}_2}}{W_{\text{C}_6\text{H}_5}Y_{\text{H}_2}}] \exp\left(-\frac{T_{\alpha,1}}{T}\right) \\ & + 8C_{\alpha,2}[\rho^2 \frac{Y_{\text{C}_2\text{H}_2}}{W_{\text{C}_2\text{H}_2}} \frac{Y_{\text{C}_6\text{H}_6}}{W_{\text{C}_6\text{H}_6}} \frac{Y_{\text{C}_6\text{H}_5}W_{\text{H}_2}}{W_{\text{C}_6\text{H}_5}Y_{\text{H}_2}}] \exp\left(-\frac{T_{\alpha,2}}{T}\right) \end{aligned} \quad (\text{A-25})$$

where $C_{\alpha,1}$, $C_{\alpha,2}$, $T_{\alpha,1}$, $T_{\alpha,2}$ are constants determined by Hall et al., (1997).

Compared with the oxidation term in Equation (A-23), oxidation due to O_2 based on the measurements of Lee et al., (1962) is added to the oxidation term in the Moss-Brookes-Hall model, which yields the following full soot oxidation term:

$$\begin{aligned} \frac{dM}{dt} = & -C_{\text{oxid}}C_{\omega,1}\eta_{\text{coll}} \left(\frac{X_{\text{OHP}}}{RT}\right) \sqrt{T}(\pi N)^{1/3}(6M/\rho_{\text{soot}})^{2/3} \\ & - C_{\text{oxid}}C_{\omega,2}\eta_{\text{coll}} \left(\frac{X_{\text{O}_2P}}{RT}\right) \exp\left(-\frac{T_{\omega,2}}{T}\right) \sqrt{T}(\pi N)^{1/3}(6M/\rho_{\text{soot}})^{2/3} \end{aligned} \quad (\text{A-26})$$

where the efficiency of inter-particle collisions, η_{coll} is set as 0.13 in this model (0.04 in Moss-Brookes model) and the scaling parameter of oxidation rate, C_{oxid} is assumed to be unity. $C_{\omega,1}=105.8125 \text{ kg} \cdot \text{m} \cdot \text{kmol}^{-1} \cdot \text{K}^{-1/2} \cdot \text{s}^{-1}$, $C_{\omega,2}= 8903.51 \text{ kg} \cdot \text{m} \cdot \text{kmol}^{-1} \cdot \text{K}^{-1/2} \cdot \text{s}^{-1}$, $T_{\omega,2}= 19778 \text{ K}$.

References

- Agarwal P., Girshick S.L., 2012. Sectional modeling of nanoparticle size and charge distributions in dusty plasmas. *Plasma Sources Science and Technology*, Vol. 21, pp. 055023.
- Akridis P., Rigopoulos S., 2015. Modelling of soot formation in a turbulent diffusion flame using a comprehensive CFD-PBE model with full chemistry. *Proceedings of the European Combustion Meeting 2015*, pp. 1-6.
- Akroyd J., Smith A. J., Shirley R., McGlashan L. R., Kraft M., 2011. A coupled CFD-population balance approach for nanoparticle synthesis in turbulent reacting flows. *Chemical Engineering Science*, Vol. 66, pp. 3792-3805.
- Alvarez R., Weilenmann M., Favez J.Y., 2008. Evidence of increased mass fraction of NO₂ within real-world NO_x emissions of modern light vehicles-derived from a reliable online measuring method. *Atmospheric Environment*, Vol. 42, pp. 4699-4707.
- Amani E., Nobari M.R.H., 2010. An efficient PDF calculation of flame temperature and major species in turbulent non-premixed flames. *Applied Mathematical Modelling*, Vol. 34, pp. 2223-2241.
- Amokrane A., Maass S., Lamadie F., Puel F., Charton S., 2016. On droplets size distribution in a pulsed column. Part I: In-situ measurements and corresponding CFD-PBE simulations. *Chemical Engineering Journal*, Vol. 296, pp. 366-376.
- Andrews M.J., O'rourke, P.J., 1996. The multiphase particle-in-cell (MP-PIC) method for dense particulate flows. *International Journal of Multiphase Flow*, Vol. 22, pp. 379-402.
- Asensio D.A., Zambon M.T., Mazza G.D., Barreto G.F., 2014. Heterogeneous two-region model for low-aspect-ratio fixed-bed catalytic reactors. Analysis of fluid-convective contributions. *Industrial & Engineering Chemistry Research*, Vol. 53, pp. 3587-3605.
- Balachandar S., Eaton J. K., 2010. Turbulent dispersed multiphase flow. *Annual Review of Fluid Mechanics*, Vol. 42, pp. 111-133.
- Balgis R., Ogi T., Wang W.N., Anilkumar G.M., Sago S., Okuyama K., 2014. Aerosol synthesis of self-organized nanostructured hollow and porous carbon particles using a dual polymer system. *Langmuir*, Vol. 30, pp. 11257-11262.
- Balthasar M., Frenklach M., 2005. Detailed kinetic modeling of soot aggregate formation in laminar premixed flames. *Combustion and Flame*, Vol. 140, pp. 130-145.
- Basavarajappa M., Miskovic S., 2016. Investigation of gas dispersion characteristics in stirred tank and flotation cell using a corrected CFD-PBM quadrature-based moment method approach. *Minerals Engineering*, Vol. 95, pp.161-184.

- Baxter G.W., Olafsen J.S., 2007. Experimental evidence for molecular chaos in granular gases. *Physical Review Letters*, Vol. 99, AN 028001.
- Bergdorf M., Koumoutsakos P., 2006. A Lagrangian particle-wavelet method. *Multiscale Modeling & Simulation*, Vol. 5, pp. 980-995.
- Bird G.A., 1994. Molecular gas dynamics. Clarendon Press, Oxford.
- Bird R.B., Stewart W.E., Lightfoot E.N., 2002. Transport phenomena (2nd edition). John Wiley & Sons, New York.
- Boivin M., Simonin O., Squires K.D., 2000. On the prediction of gas-solid flows with two-way coupling using large eddy simulation. *Physics of Fluids*, Vol. 12, pp. 2080-2090.
- Boushaki T., Merlo N., Chauveau C., Gökalp I., 2016. Study of emission pollutants and dynamics of non-premixed turbulent oxygen enriched flames from a swirl burner. *Proceedings of the Combustion Institute*. (In press).
- Bouvier Y., Mihešan C., Ziskind M., Therssen E., Focsa C., Pauwels J.F., Desgroux P., 2007. Molecular species adsorbed on soot particles issued from low sooting methane and acetylene laminar flames: a laser-based experiment. *Proceedings of the Combustion Institute*, Vol. 31, pp. 841-849.
- Boy M., Hellmuth O., Korhonen H., Nilsson E.D., Revelle D., Turnipseed A., Arnold F., Kulmala M., 2006. MALTE-model to predict new aerosol formation in the lower troposphere. *Atmospheric Chemistry and Physics*, Vol. 6, pp. 4499-4517.
- Brookes S.J., Moss J.B., 1999. Measurements of soot production and thermal radiation from confined turbulent jet diffusion flames of methane. *Combustion and Flame*, Vol. 116, pp. 49-61.
- Brumby P.E., Sato T., Nagao J., Tenma N., Narita H., 2015. Coupled LBM-DEM micro-scale simulations of cohesive particle erosion due to shear flows. *Transport in Porous Media*, Vol. 109, pp. 43-60.
- Buchmayr M., Gruber J., Hargassner M., Hochenauer C., 2016. A computationally inexpensive CFD approach for small-scale biomass burners equipped with enhanced air staging. *Energy Conversion and Management*, Vol. 115, pp. 32-42.
- Byun D., Schere K.L., 2006. Review of the governing equations, computational algorithms, and other components of the models-3 community multiscale air quality (CMAQ) modeling system. *Applied Mechanics Reviews*, Vol. 59, pp. 51-77.
- Calvo A. I., Alves C., Castro A., Pont V., Vicente A. M., Fraile R., 2013. Research on aerosol sources and chemical composition: past, current and emerging issues. *Atmospheric Research*, Vol. 120, pp. 1-28.
- Campbell S.A., Palsmeier J., Loyalka S.K., 2016. Mesh-free simulation of aerosol evolution. *Nuclear Science and Engineering*, Vol. 182, pp. 287-296.

References

- Center E., Bruneaux G., Pickett L., Schulz C., 2013. Study of soot formation and oxidation in the engine combustion network (ECN), spray a: effects of ambient temperature and oxygen concentration. *SAE International Journal of Engines*, Vol. 6, pp. 352-365.
- Celis C., da Silva L.F.F., 2015. Lagrangian mixing models for turbulent combustion: Review and prospects. *Flow, Turbulence and Combustion*, Vol. 94, pp. 643-689.
- Celnik M., Patterson R., Kraft M., Wagner W., 2007. Coupling a stochastic soot population balance to gas-phase chemistry using operator splitting. *Combustion and Flame*, Vol. 148, pp.158-176.
- Cercignani, C., 1988. The Boltzmann equation and its applications. Springer-Verlag, New York.
- Chacon R.V., Ornstein D.S., 1960. A general ergodic theorem. *Illinois Journal of Mathematics*, Vol. 4, pp. 153-160.
- Chamkha A. J., Rashad A.M., 2012, Natural convection from a vertical permeable cone in a nanofluid saturated porous media for uniform heat and nanoparticles volume fraction fluxes. *International Journal of Numerical Methods for Heat & Fluid Flow*, Vol. 22, pp. 1073-1085.
- Chan T.L., Liu Y.H., Chan C.K., 2010. Direct quadrature method of moments for the exhaust particle formation and evolution in the wake of the studied ground vehicle. *Journal of Aerosol Science*, Vol. 41, pp. 553-568.
- Chan T.L., Ning Z., Leung C.W., Cheung C.S., Hung W.T., Dong G., 2004. On-road remote sensing of petrol vehicle emissions measurement and emission factors estimation in Hong Kong. *Atmospheric Environment*, Vol. 38, pp. 2055-2066.
- Chan T.L., Xie M.L., Cheung C.S., 2009. An efficient Petrov-Galerkin Chebyshev spectral method coupled with the Taylor-series expansion method of moments for solving the coherent structures effect on particle coagulation in the exhaust pipe. *CMES-Computer Modeling In Engineering & Sciences*, Vol. 51, pp. 191-212.
- Chen D.R., Pui D.Y., Hummes D., Fissan H., Quant F.R., Sem G.J., 1998. Design and evaluation of a nanometer aerosol differential mobility analyzer (nano-DMA). *Journal of Aerosol Science*, Vol. 29, pp. 497-509.
- Chen Z.L, Lin J.Z., Yu M.Z, 2014. Direct expansion method of moments for nanoparticle Brownian coagulation in the entire size regime. *Journal of Aerosol Science*, Vol. 67, pp. 28-37.
- Chen X.Z., Luo Z.H., Yan W.C., Lu Y.H., Ng I.S., 2011. Three-dimensional CFD-PBM coupled model of the temperature fields in fluidized-bed polymerization reactors. *AIChE Journal*, Vol. 57, pp. 3351-3366.
- Consalvi J.L., Nmira F., 2016. Transported scalar PDF modeling of oxygen-enriched turbulent jet diffusion flames: Soot production and radiative heat transfer. *Fuel*, Vol. 178, pp. 37-48.

Crowe C.T., Sharma M.P., Stock D.E., 1977. The particle-source-in cell (PSI-CELL) model for gas-droplet flows. *Journal of Fluids Engineering*, Vol. 99, pp. 325-332.

Darbandi M., Karchani A., Akhlaghi H., Schneider G., 2010. Gas Properties Effects in Microchannel Studies Using Direct Simulation Monte Carlo. In *ASME 2010 8th International Conference on Nanochannels, Microchannels, and Minichannels collocated with 3rd Joint US-European Fluids Engineering Summer Meeting*. American Society of Mechanical Engineers. pp. 1021-1027

Debry E., Sportisse B., Jourdain B., 2003. A stochastic approach for the numerical simulation of the general dynamics equation for aerosols, *Journal of Computational Physics*, Vol.184, pp. 649-669.

Deen N.G., Kuipers J.A.M., 2014. Direct Numerical simulation of fluid flow accompanied by coupled mass and heat transfer in dense fluid-particle systems. *Chemical Engineering Science*, Vol. 116, pp. 645-656.

DeVile R.E.L., Riemer N., West M., 2011. Weighted flow algorithms (WFA) for stochastic particle coagulation. *Journal of Computational Physics*, Vol. 230, pp. 8427-8451.

Di Veroli G., Rigopoulos S., 2010. Modeling of turbulent precipitation: A transported population balance-PDF method. *AIChE journal*, Vol. 56, pp. 878-892.

Di Veroli G.Y., Rigopoulos S., 2011. Modeling of aerosol formation in a turbulent jet with the transported population balance equation-probability density function approach. *Physics of Fluids* (1994-present) Vol. 23, No. 043305.

Dreyer J.A., Riefler N., Pesch G.R., Karamehmedović M., Fritsching U., Teoh W.Y., Mädler L., 2014. Simulation of gas diffusion in highly porous nanostructures by direct simulation Monte Carlo. *Chemical Engineering Science*, Vol. 105, pp. 69-76.

Du M., Zhao C.S., Zhou B., Hao Y.L., 2013. DSMC prediction of particle behavior in gas-particle two-phase impinging streams. *Mathematical Problems in Engineering*, Vol. 2013, pp. 1-11.

Edge P., Gharebaghi M., Irons R., Porter R., Porter R.T.J., Pourkashanian M., Smith D., Stephenson P., William A., 2011. Combustion modelling opportunities and challenges for oxy-coal carbon capture technology. *Chemical Engineering Research and Design*, Vol. 89, pp. 1470-1493.

Efendiev Y., 2004. Modeling and simulation of multi-component aerosol dynamics. *Computational & Applied Mathematics*, Vol. 23, pp. 401-423.

Efendiev Y., Zachariah M.R., 2002. Hybrid Monte Carlo method for simulation of two-component aerosol coagulation and phase segregation. *Journal of Colloid and Interface Science*, Vol. 249, pp. 30-43.

Eibeck A., Wagner W., 2001. Stochastic particle approximations for Smoluchowski's coagulation equation. *Annals of Applied Probability*, Vol. 11, pp. 1137-1165.

References

- Epstein M., Ellison P.G., 1987. A principle of similarity for describing aerosol particle size distributions. *Journal of colloid and interface science*, Vol. 119, pp. 168-173.
- Erickson W.D., Williams G.C., Hottel H.C., 1964. Light scattering measurements on soot in a benzene-air flame. *Combustion and Flame*, Vol. 8, pp. 127-132.
- Fede P., Simonin O., Villedieu P., 2015. Monte-Carlo simulation of colliding particles or coalescing droplets transported by a turbulent flow in the framework of a joint fluid-particle pdf approach. *International Journal of Multiphase Flow*, Vol. 74, pp. 165-183.
- Feng Y., Kleinstreuer C., Castro N., Rostami A., 2016. Computational transport, phase change and deposition analysis of inhaled multicomponent droplet–vapor mixtures in an idealized human upper lung model. *Journal of Aerosol Science*, Vol. 96, pp. 96-123.
- Fox R.O., 2003. Computational models for turbulent reacting flows. Cambridge University Press, Cambridge.
- Frenklach M., Harris S.J., 1987, Aerosol dynamics modelling using the method of moments. *Journal of colloid and interface science*, Vol. 118, pp. 252-261.
- Frenklach M., Wang H., 1991, Detailed modeling of soot particle nucleation and growth. *Symposium (International) on Combustion*, Vol. 23, pp. 1559-1566.
- Frenklach M., Wang H., 1994, Detailed mechanism and modeling of soot particle formation. In *Soot formation in combustion* (pp.165-192). Springer Berlin Heidelberg.
- Frenklach M., Wang H., Goldenberg M., Smith G.P., Golden D.M., 1995. GRI-MECH: An optimized detailed chemical reaction mechanism for methane combustion. Topical report, September 1992-August 1995 (No. PB-96-137054/XAB). SRI International, Menlo Park, CA (United States).
- Friedlander S., 2000. Smoke, dust and haze: fundamentals of aerosol dynamics. Second ed. Oxford University Press, Oxford.
- Friedlander S.K., Wang C.S., 1966. The self-preserving particle size distribution for coagulation by Brownian motion. *Journal of Colloid and interface Science*, Vol. 22, pp. 126-132.
- Fu K., Liang D., Wang W.Q., Cheng Y., Gong S.L., 2012. Multi-component atmospheric aerosols prediction by a multi-functional MC-HDMR approach. *Atmospheric Research*, Vol.113, pp. 43-56.
- Gac J.M., Gradoń L., 2013. A distributed parameter model for the drying of multicomponent aerosol and sessile droplets. *Chemical Engineering*, Vol. 32, pp. 1927-1932.
- Garrick S. C., 2015. Growth mechanisms of nanostructured Titania in turbulent reacting flows. *Journal of Nanotechnology 2015*, Article ID 642014, pp. 1-11.

- Ge H.W., Gutheil E., 2008. Simulation of a turbulent spray flame using coupled PDF gas phase and spray flamelet modeling. *Combustion and Flame*, Vol. 153, pp. 173-185.
- Gelbard F., Seinfeld J.H., 1980. Simulation of multicomponent aerosol dynamics. *Colloid and Interface Science*, Vol. 78, pp. 485-501.
- Geng J., Park H., Sajo E., 2013. Simulation of aerosol coagulation and deposition under multiple flow regimes with arbitrary computational precision. *Aerosol Science and Technology*, Vol. 47, pp. 530-542.
- Ghahramani E., Abouali O., Emdad H., Ahmadi G., 2014. Numerical analysis of stochastic dispersion of micro-particles in turbulent flows in a realistic model of human nasal/upper airway. *Journal of Aerosol Science*, Vol. 67, pp. 188-206.
- Giannakopoulos A.E., Sofos F., Karakasidis T.E., Liakopoulos A., 2014. A quasi-continuum multi-scale theory for self-diffusion and fluid ordering in nanochannel flows. *Microfluidics and Nanofluidics*, Vol. 17, pp. 1011-1023.
- Gillespie D.T., 1972. Stochastic coalescence model for cloud droplet growth. *Journal of the Atmospheric Sciences*, Vol. 29, pp. 1496-1510.
- Guan Q., Urness K.N., Ormond T.K., David D.E., Barney Ellison G., Daily J.W., 2014. The properties of a micro-reactor for the study of the unimolecular decomposition of large molecules. *International Reviews in Physical Chemistry*, Vol. 33, pp. 447-487.
- Gunawan R., Fusman I., Braatz R.D., 2004. High resolution algorithms for multidimensional population balance equations. *AIChE Journal*, Vol. 50, pp. 2738-2749.
- Hall R.J., Smooke M.D., Colket M.B., 1997. Physical and chemical aspects of combustion. *Gordon and Breach*.
- Hao X.M., Zhao H.B., Xu Z.W., Zheng C.G., 2013. Population balance-Monte Carlo simulation for gas-to-particle synthesis of nanoparticles. *Aerosol Science and Technology*, Vol. 47, pp. 1125-1133.
- Hastings W.K., 1970. Monte Carlo sampling methods using Markov chains and their applications. *Biometrika*, Vol. 57, pp. 97-109.
- Haworth D.C., 2010. Progress in probability density function methods for turbulent reacting flows. *Progress in Energy and Combustion Science*, Vol. 36, pp.168-259.
- Haworth D.C., Pope S.B., 2011. Transported probability density function methods for Reynolds-averaged and large-eddy simulations. *Fluid Mechanics and its Applications*, Vol. 95 (*Turbulent Combustion Modeling*), pp.119-142.
- He K., Retterer S.T., Srijanto B.R., Conrad J.C., Krishnamoorti R., 2014. Transport and dispersion of nanoparticles in periodic nanopost arrays. *ACS Nano*, Vol. 8, pp. 4221-4227.

References

- He Y., Zhao H., Wang H., Zheng C., 2015. Differentially weighted direct simulation Monte Carlo method for particle collision in gas-solid flows. *Particuology*, Vol. 21, pp. 135-145.
- He Y., Zhao H., 2016. Conservative particle weighting scheme for particle collision in gas-solid flows. *International Journal of Multiphase Flow*, Vol. 83, pp.12-26.
- Heravi D.F., Heravi H.M., Bashirnezhad K., Sanaei H., Samiee A., 2010. Experimental and Numerical Analysis of Carbon Black Formation in Hydrocarbon/Air Diffusion Flames. In *ASME 2010 10th Biennial Conference on Engineering Systems Design and Analysis*, Vol. 2, pp. 591-599.
- Hesamzadeh M.R., Rahman A.M.Z.U., Amelin M., 2011. The probabilistic TC-PSI for studying market power. In *Innovative Smart Grid Technologies Asia (ISGT), 2011 IEEE PES*, pp. 1-7.
- Hess A., Tarik M., Foppiano D., Edinger P., Ludwig C., 2016. Online size and element analysis of aerosol particles released from thermal treatment of wood samples impregnated with different salts. *Energy & Fuels*, Vol. 30, pp. 4072-4084.
- Holden H., Karlsen K.H., Lie K.A., Risebro N.H., 2010. Splitting methods for partial differential equations with rough solutions: analysis and MATLAB programs. *EMS Series of Lectures in Mathematics*. European Mathematical Society (EMS), Zürich.
- Hounslow M. J., Ryall R. L., Marshall V. R., 1988. A discretized population balance for nucleation, growth, and aggregation. *AIChE Journal*, Vol. 34, pp. 1821-1832.
- Intra P., Yawootti A., Rattanadecho P., 2014. Numerical and experimental studies of collection efficiency of an ion electrostatic collector for a mini-volume electrical pm detector. *Journal of Electrostatics*, Vol. 72, pp. 477-486.
- Jaishree J., Haworth D. C., 2012. Comparisons of Lagrangian and Eulerian PDF methods in simulations of non-premixed turbulent jet flames with moderate-to-strong turbulence-chemistry interactions. *Combustion Theory and Modelling*, Vol. 16, pp. 435-463.
- Jangi M., Zhao X., Haworth D.C., Bai X.S., 2015. Stabilization and liftoff length of a non-premixed methane/air jet flame discharging into a high-temperature environment: An accelerated transported PDF method. *Combustion and Flame*, Vol. 162, pp. 408-419.
- Jenny P., Pope S.B., Muradoglu M., Caughey D.A., 2001. A hybrid algorithm for the joint PDF equation of turbulent reactive flows. *Journal of Computational Physics*, Vol. 166, pp. 218-252.
- Jeong J.I., Choi M., 2001. A sectional method for the analysis of growth of polydisperse non-spherical particles undergoing coagulation and coalescence. *Journal of Aerosol Science*, Vol. 32, pp. 565-582.
- Jeong J.I., Choi M., 2003. Analysis of non-spherical polydisperse particle growth in a two-dimensional tubular reactor. *Journal of Aerosol Science*, Vol. 34, pp. 713-32.

- Ježek I., Katrašnik T., Westerdahl D., Močnik G., 2015. Black carbon, particle number concentration and nitrogen oxide emission factors of random in-use vehicles measured with the on-road chasing method. *Atmospheric Chemistry and Physics*, Vol. 15, pp.11011-11026.
- Jiménez S., Ballester J., 2005. A comparative study of different methods for the sampling of high temperature combustion aerosols. *Aerosol science and technology*, Vol. 39, pp. 811-821.
- Kazakov A., Frenklach M., 1998. Dynamic modeling of soot particle coagulation and aggregation: Implementation with the method of moments and application to high-pressure laminar premixed flames. *Combustion and Flame*, Vol. 114, pp. 484-501.
- Khan I.M., Greeves G., 1974. A method for calculating the formation and combustion of soot in diesel engines. *Heat transfer in flames*, Chapter 25, Washington DC.
- Klimanek A., Adamczyk W., Katelbach-Woźniak A., Węcel G., Szlęk A., 2015. Towards a hybrid Eulerian–Lagrangian CFD modeling of coal gasification in a circulating fluidized bed reactor. *Fuel*, Vol. 152, pp. 131-137.
- Koumoutsakos P., 2005. Multiscale flow simulations using particles. *Annual Reviews of Fluid Mechancis*, Vol. 37, pp. 457-487.
- Kruggel-Emden H., Kravets B., Suryanarayana M.K., Jasevicius R., 2016. Direct numerical simulation of coupled fluid flow and heat transfer for single particles and particle packings by a LBM-approach. *Powder Technology*, Vol. 294, pp. 236-251.
- Kruis F.E., Maisels A., Fissan H., 2000. Direct simulation Monte Carlo method for particle coagulation and aggregation. *AIChE Journal*, Vol. 46, pp. 1735-1742.
- Kruis F.E., Wei J.M., van der Zwaag T., Haep S., 2012. Computational fluid dynamics based stochastic aerosol modelling: combination of a cell-based weighted random walk method and a constant-number Monte-Carlo method for aerosol dynamics. *Chemical Engineering Science*, Vol. 70, pp. 109-120.
- Kulmala M., Asmi A., Lappalainen H., Baltensperger U., Brengner M.C., 2009. Introduction: European integrated project on aerosol cloud climate and air quality interactions (EUCAARI)–integrating aerosol research from nano to global scales. *Atmospheric Chemistry and Physics*, Vol. 9, pp. 2825-2841.
- Kumar P., Ketzler M., Vardoulakis S., Pirjola L., Britter R., 2011. Dynamics and dispersion modelling of nanoparticles from road traffic in the urban atmospheric environment-a review. *Journal of Aerosol Science*, Vol. 42, pp. 580-603.
- Kumar S., Ramkrishna D., 1997. On the solution of population balance equations by discretization-iii. Nucleation, growth and aggregation of particles. *Chemical Engineering Science*, Vol. 52, pp. 4659-4679.

- Kuo K.K.Y., Acharya R., 2012. Fundamentals of turbulent and multi-phase combustion. John Wiley & Sons, New Jersey.
- Laitinen T., Martín S.H., Parshintsev J., Hyötyläinen T., Hartonen K., Riekkola M.L., Kulmala M., Pavón J.L.P., 2010. Determination of organic compounds from wood combustion aerosol nanoparticles by different gas chromatographic systems and by aerosol mass spectrometry. *Journal of chromatography A*, Vol. 1217, pp.151-159.
- Laskin J., Laskin A., Roach P.J., Slysz G.W., Anderson G.A., Nizkorodov S. A., Bones D.L., Nguyen L.Q., 2010. High-resolution desorption electrospray ionization mass spectrometry for chemical characterization of organic aerosols. *Analytical chemistry*, Vol. 82, pp. 2048-2058.
- Lee K.B., Thring M.W., Beer J.M., 1962. On the rate of combustion of soot in a laminar soot flame. *Combustion and Flame*, Vol. 6, pp. 137-145.
- Lee Y., Engquist B., 2016. Multiscale numerical methods for passive advection–diffusion in incompressible turbulent flow fields. *Journal of Computational Physics*, Vol. 317, pp. 33-46.
- Leonard A.D., Dai F., 1994. Applications of a coupled Monte Carlo PDF/finite volume CFD method for turbulent combustion. AIAA Paper No. 94-2904
- Lesniewski T., Friedlander S. K., 1995. The effect of turbulence on rates of particle formation by homogeneous nucleation. *Aerosol Science and Technology*, Vol. 23, pp. 174-182.
- Li Y., Jiang Y., Zhao J., Liu C., Zhang L., 2015. Extended finite element method for analysis of multi-scale flow in fractured shale gas reservoirs. *Environmental Earth Sciences*, Vol. 73, pp. 6035-6045.
- Liffman K., 1992. A direct simulation Monte-Carlo method for cluster coagulation. *Journal of Computational Physics*, Vol. 100, pp. 116-127.
- Lin J.Z., Chen Z.L., 2013. A modified TEMOM model for Brownian coagulation of nanoparticles based on the asymptotic solution of the sectional method. *Science China Technological Sciences*, Vol. 56, pp. 1-12.
- Lindstedt R.P., Louloudi S.A., 2005. Joint-scalar transported PDF modelling of soot formation and oxidation. *Proceedings of the Combustion Institute*, Vol. 30, pp. 775-783.
- Liu S.Y., Chan T.L., 2016. A coupled CFD-Monte Carlo method for aerosol dynamics in turbulent flows. In Press. (DOI: 10.1080/02786826.2016.1260087).
- Liu S.Y., Chan T.L., 2017. A stochastically weighted operator splitting Monte Carlo (SWOSMC) method for the numerical simulation of complex aerosol dynamic processes. *International Journal of Numerical Methods for Heat and Fluid Flow*, Vol. 27, pp. 263-278.

References

- Liu S.Y., Chan T.L., Zhou K., 2015. A new stochastically weighted operator splitting Monte Carlo method for particle-fluid systems. *ASME-ATI-UIT 2015 Conference on Thermal Energy Systems: Production, Storage, Utilization and the Environment* (In Session: Computational Thermal-fluid Dynamics), May 17-20, Naples, Italy.
- Liu F., Guo H., Smallwood G.J., Gülder Ö.L., 2003. Numerical modelling of soot formation and oxidation in laminar coflow non-smoking and smoking ethylene diffusion flames. *Combustion Theory and Modelling*, Vol. 7, pp. 301-315.
- Lu B., Luo H., Li H., Wang W., Ye M., Liu Z., Li J., 2016. Speeding up CFD simulation of fluidized bed reactor for MTO by coupling CRE model. *Chemical Engineering Science*, Vol. 143, pp. 341-350.
- Lundgren T.S., 1967. Distribution functions in the statistical theory of turbulence. *Physics of Fluids*, Vol. 10, pp. 969-975.
- Luo H.Y., Liu Y., Yang X.L., 2007. Particle deposition in obstructed airways. *Journal of Biomechanics*, Vol. 40, pp. 3096-3104.
- Ma D.L., Tafti D.K., Braatz R.D., 2002. High-resolution simulation of multidimensional crystal growth. *Industrial Engineering Chemistry Research*, Vol. 41, pp. 6217-6223.
- Mahmoudi A.H., Hoffmann F., Peters B., 2014. Application of XDEM as a novel approach to predict drying of a packed bed. *International Journal of Thermal Sciences*, Vol. 75, pp. 65-75.
- Maisels A., Kruis F.E., Fissan H., 2004. Direct simulation Monte Carlo for simultaneous nucleation, coagulation, and surface growth in dispersed systems. *Chemical Engineering Science*, Vol. 59, pp. 2231-2239.
- Makinde O.D., Khan W.A., Chinyoka T., 2013. New Developments in Fluid Mechanics and Its Engineering Applications. *Mathematical Problems in Engineering*, AN 797390, pp. 1-3.
- Maricq M.M., Harris S.J., Sente J.J., 2003. Soot size distributions in rich premixed ethylene flames. *Combustion and flame*, Vol. 132, pp. 328-342.
- Maxwell J.C., 1867. On the dynamical theory of gases. *Philosophical transactions of the Royal Society of London*, Vol. 157, pp. 49-88.
- McLachlan R.I., Quispel G.R.W., 2002. Splitting methods. *Acta Numerica*, Vol. 11, pp. 341-434.
- Mehta R.S., 2008. Detailed modeling of soot formation and turbulence-radiation interactions in turbulent jet flames. The Pennsylvania State University, PhD thesis.
- Mehta R.S., Haworth D.C., Modest M.F., 2010. Composition PDF/photon Monte Carlo modeling of moderately sooting turbulent jet flames. *Combustion and Flame*, Vol. 157, pp. 982-994.

- Meyer D. W., 2010. A new particle interaction mixing model for turbulent dispersion and turbulent reactive flows. *Physics of Fluids* (1994-present), Vol. 22, pp. 035103.
- Minier J. P., 2015. On Lagrangian stochastic methods for turbulent polydisperse two-phase reactive flows. *Progress in Energy and Combustion Science*, Vol. 50, pp. 1-62.
- Mitrakos D., Hinis E., Housiadas C., 2007. Sectional modeling of aerosol dynamics in multi-dimensional flows. *Aerosol Science and Technology*, Vol. 41, pp. 1076-1088.
- Möbus H., Gerlinger P., Brüggemann D., 2001. Comparison of Eulerian and Lagrangian Monte Carlo PDF methods for turbulent diffusion flames. *Combustion and Flame*, Vol. 124, pp. 519-534.
- Modest M.F., 2003. *Radiative Heat Transfer* (second Edn), Academic Press, New York.
- Mohammadzadeh A., Roohi E., Niazmand H., 2013. A parallel DSMC investigation of monatomic/diatom gas flows in a micro/nano cavity. *Numerical Heat Transfer, Part A: Applications*, Vol. 63, pp. 305-325.
- Nere N.K., Ramkrishna D., 2006. Solution of population balance equation with pure aggregation in a fully developed turbulent pipe flow. *Chemical Engineering Science*, Vol. 61, pp. 96-103.
- Nie X.B., Chen S.Y., Robbins M.O., 2004. A Continuum and molecular dynamics hybrid method for micro-and nano-fluid flow. *Fluid Mechanics*, Vol. 500, pp. 55-64.
- Novozhilov V., Harvie D.J.E., Green A.R., Kent J.H., 1997. A computational fluid dynamic model of fire burning rate and extinction by water sprinkler. *Combustion Science and Technology*, Vol. 123, pp. 227-245.
- Öktem B., Tolocka M.P., Zhao B., Wang H., Johnston M.V., 2005. Chemical species associated with the early stage of soot growth in a laminar premixed ethylene–oxygen–argon flame. *Combustion and Flame*, Vol. 142, pp. 364-373.
- Oñate E., Celigueta M.A., Latorre S., Casas G., Rossi R., Rojek J., 2014. Lagrangian analysis of multiscale particulate flows with the particle finite element method. *Computational Particle Mechanics*, Vol. 1, pp. 85-102.
- Oran E.S., Oh C.K., Cybyk B.Z., 1998. Direct simulation Monte Carlo: recent advances and applications. *Annual Review of Fluid Mechanics*, Vol. 30, pp. 403-441.
- Ozawa Y., Takeda N., Miyakawa T., Takei M., Hirayama N., Takegawa N., 2016. Evaluation of a particle trap laser desorption mass spectrometer (PT-LDMS) for the quantification of sulfate aerosols. *Aerosol Science and Technology*, Vol. 50, pp. 173-186.

- Palaniswaamy G., Loyalka S.K., 2008. Direct simulation Monte Carlo, aerosol dynamics: coagulation and condensation. *Annals of Nuclear Energy*, Vol. 35, pp. 485-494.
- Pang K.M., Karvounis N., Walther J. H., Schramm J., 2016. Numerical investigation of soot formation and oxidation processes under large two-stroke marine diesel engine-like conditions using integrated CFD-chemical kinetics. *Applied Energy*, Vol. 169, pp. 874-887.
- Pant T., Huang C., Han C., Sardeshmukh S. V., Anderson W. E., Wang H., 2016. Flamelet modeling studies of a continuously variable resonance combustor. In *54th AIAA Aerospace Sciences Meeting*, pp. 1941.
- Patankar N.A., Joseph D.D., 2001. Modeling and numerical simulation of particulate flows by the Eulerian-Lagrangian approach. *International Journal of Multiphase Flow*, Vol. 27, pp. 1659-1684.
- Park Y.K., Jung S.C., Park S.H., 2013. Development of a moment model for condensational obliteration of nanoparticle aggregates. *Journal of Nanoscience and Nanotechnology*, Vol. 13, pp. 2008-2011.
- Patki A., Li X., Chen D., Lou H., Richmond P., Damodara V. Liu L., Rasel K., Alphones A., Zhou J., 2014. On Numerical Simulation of Black Carbon (Soot) Emissions from Non-Premixed Flames. *Journal of Geoscience and Environment Protection*, Vol. 2, pp. 15-24.
- Patterson R.I.A., Singh, J., Balthasar, M., Kraft, M., Norris, J.R., 2006. The linear process deferment algorithm: a new technique for solving population balance equations. *SIAM Journal of Scientific Computing*, Vol. 28, pp. 303-320.
- Patterson R.I.A., 2007. Numerical modelling of soot formation. University of Cambridge, PhD thesis.
- Patterson R. I., Wagner W., Kraft M., 2011. Stochastic weighted particle methods for population balance equations. *Journal of Computational Physics*, Vol. 230, pp. 7456-7472.
- Peglow M., Kumar J., Warnecke G., Heinrich S., Mörl L., 2006. A new technique to determine rate constants for growth and agglomeration with size-and time-dependent nuclei formation. *Chemical Engineering Science*, Vol. 61, pp. 282-292.
- Pesmazoglou I., Kempf A.M., Navarro-Martinez S., 2014. Aerosol nucleation in a turbulent jet using large eddy simulations. *Chemical Engineering Science*, Vol.116, pp. 383-397.
- Pesmazoglou I., Kempf A.M., Navarro-Martinez S., 2016. Stochastic modelling of particle aggregation. *International Journal of Multiphase Flow*, Vol. 80, pp. 118-130.

- Pialat X., Simonin O., Villedieu P., 2006. Direct coupling between Eulerian and Lagrangian approaches in turbulent gas-solid flows. *In ASME 2006 2nd Joint US-European Fluids Engineering Summer Meeting Collocated With the 14th International Conference on Nuclear Engineering*, pp. 527-536. American Society of Mechanical Engineers.
- Pollack M., Salenbauch S., Marchisio D.L., Hasse C., 2016. Bivariate extensions of the extended quadrature method of moments (EQMOM) to describe coupled droplet evaporation and heat-up. *Journal of Aerosol Science*, Vol. 92, pp. 53-69.
- Pope S.B., 1981. A Monte Carlo method for the PDF equations of turbulent reactive flow. *Combustion Science and Technology*, Vol. 25, pp. 159-174.
- Pope S.B., 1985. PDF methods for turbulent reactive flows. *Progress in Energy and Combustion Science*, Vol. 11, pp. 119-192.
- Pope, S.B., 1994. Lagrangian PDF methods for turbulent flows. *Annual Review of Fluid Mechanics*, Vol. 26, pp. 23-63.
- Pope S.B., Tirunagari, R., 2014. Advances in probability density function methods for turbulent reactive flows. *In Proceedings of the Nineteenth Australasian Fluid Mechanics Conference*, RMIT University, Melbourne.
- Prakash A., Bapat A.P., Zachariah M.R., 2003. A simple numerical algorithm and software for solution of nucleation, condensation, and coagulation problems. *Aerosol Science and Technology*, Vol. 37, pp. 892-898.
- Pratsinis S.E., 1988. Simultaneous nucleation, condensation, and coagulation in aerosol reactors. *Colloid and Interface Science*, Vol. 124, pp. 416-427.
- Ramabhadran T.E., Peterson T.W., Seinfeld, J.H., 1976, Dynamics of aerosol coagulation and condensation. *AIChE Journal*, Vol. 22, pp. 840-851.
- Ramkrishna D., 2000. Population balances: theory and applications to particulate systems in engineering. Academic press, San Diego.
- Reade W. C., Collins L. R., 2000. A numerical study of the particle size distribution of an aerosol undergoing turbulent coagulation. *Journal of Fluid Mechanics*, Vol. 415, pp. 45-64.
- Rieffel M.A., 1999. A method for estimating the computational requirements of DSMC simulations. *Journal of Computational Physics*, Vol. 149, pp. 95-113.
- Rigopoulos S., 2007. PDF method for population balance in turbulent reactive flow. *Chemical Engineering Science*, Vol. 62, pp. 6865-6878.
- Rigopoulos S., Jones A.G., 2003. Finite-element scheme for solution of the dynamic population balance equation. *AIChE Journal*, Vol. 49, pp. 1127.
- Rjasanow S., Wagner W., 1996. Stochastic weighted particle method for the Boltzmann equation. *Journal of Computational Physics*, Vol. 124, pp. 243-253.

References

- Robertson L., Langner J., Engardt M., 1999. An Eulerian limited-area atmospheric transport model. *Applied Meteorology*, Vol. 38, pp. 190-210.
- Roldin P., Swietlicki E., Schurgers G., Arneth A., Lehtinen K.E.J. Boy M., Kulmala M., 2011. Development and evaluation of the aerosol dynamics and gas phase chemistry model ADCHEM. *Atmospheric Chemistry and Physics*, Vol. 11, pp. 5867-5896.
- Rong L.W., Dong K.J., Yu A.B., 2014. Lattice-Boltzmann simulation of fluid flow through packed beds of spheres: effect of particle size distribution. *Chemical Engineering Science*, Vol. 116, pp. 508-523.
- Roohi E., Darbandi M., 2012. Recommendations on performance of parallel DSMC algorithm in solving subsonic nano-flows. *Applied Mathematical Modelling*, Vol. 36, pp. 2314-2321.
- Sabel'nikov V., Soulard O., 2005. Rapidly decorrelating velocity-field model as a tool for solving one-point Fokker-Planck equations for probability density functions of turbulent reactive scalars. *Physical Review E*, Vol. 72, pp. 016301.
- Saffman P.G., Turner J.S., 1956. On the collision of drops in turbulent clouds. *Journal of Fluid Mechanics*, Vol. 1, pp. 16-30.
- Seinfeld J.H., Pandis S.N., 1998. *Atmospheric Chemistry and Physics*, Wiley-Interscience, New York, NY.
- Settumba N., Garrick S.C., 2004. A comparison of diffusive transport in a moment method for nanoparticle coagulation. *Journal of Aerosol Science*, Vol. 35, pp. 93-101.
- Smith T.N., Phillips C.R., 1975. Inertial collection of aerosol particles at circular aperture. *Environmental Science & Technology*, Vol. 9, pp. 564-568.
- Snider D.M., 2001. An incompressible three-dimensional multiphase particle-in-cell model for dense particle flows. *Journal of Computational Physics*, Vol. 170, pp. 523-549.
- Subramaniam S., 2013. Lagrangian-Eulerian methods for multiphase flows. *Progress in Energy and Combustion Science*, Vol. 39, pp. 215-245.
- Subramaniam S., Haworth D.C., 2000. A probability density function method for turbulent mixing and combustion on three-dimensional unstructured deforming meshes. *International Journal of Engine Research*, Vol. 1, pp. 171-190.
- Subramaniam S., Pope S.B., 1998. A mixing model for turbulent reactive flows based on Euclidean minimum spanning trees. *Combustion and Flame*, Vol. 115, pp. 487-514.
- Swift D.L., Friedlander S.K., 1964. The coagulation of hydrolysis by Brownian motion and laminar shear flow. *Journal of Colloid Science*, Vol 19, pp. 621-647.

References

- Sznitman A.S., Zerner M., 1999. A law of large numbers for random walks in random environment. *Annals of probability*, Vol. 27, pp. 1851-1869.
- Tesner P.A., Smegiriova T.D., Knorre V.G., 1971. Kinetics of dispersed carbon formation. *Combustion and Flame*, Vol. 17, pp. 253-260.
- Trump E.R., Fountoukis C., Donahue N.M., Pandis S.N., 2015. Improvement of simulation of fine inorganic PM levels through better descriptions of coarse particle chemistry. *Atmospheric Environment*, Vol. 102, pp. 274-281.
- Tu C., Zhang J., 2014. Nanoparticle-laden gas flow around a circular cylinder at high Reynolds number. *International Journal of Numerical Methods for Heat & Fluid Flow*, Vol. 24, pp. 1782-1794.
- Turns S.R., 2011. An introduction to combustion: concepts and applications. 3rd edition, McGraw Hill Higher Education.
- Valiño L., 1998. Field Monte Carlo formulation for calculating the probability density function of a single scalar in turbulent flows. *Flow Turbulence and Combustion*, Vol. 60, pp. 157.
- Valsaraj K.T., Kommalapati R.R., 2009. Atmospheric aerosols: characterization, chemistry, modeling, and climate. *American Chemical Society Symposium Series*, Vol. 1005, Oxford University Press, USA.
- Vancassel X., Mirabel P., Garnier F., 2014. Numerical simulation of aerosols in an aircraft wake using a 3D LES solver and a detailed microphysical model. *International Journal of Sustainable Aviation*, Vol. 1, pp. 139-159.
- Vela I., 2009. CFD prediction of thermal radiation of large, sooty, hydrocarbon pool fires. Universität Duisburg-Essen, PhD thesis.
- Wang H., Du D.X., Sung C.J., Law C.K., 1996. Experiments and numerical simulation on soot formation in opposed-jet ethylene diffusion flames. In *Symposium (International) on Combustion*, Vol. 26, pp. 2359-2368.
- Wang S., Lu H.L., Hao Z.H., Lu H.L., Liu G.D., Li D., Zhao F.X., 2014. Numerical modeling of a bubbling fluidized bed coal gasifier by kinetic theory of rough spheres. *Fuel*, Vol. 130, pp. 197-202.
- Wang Y., Wang M., Zhang R., Ghan S.J., Lin Y., Hu, J., Pan B., Levy M., Jiang J. H., Molina M.J., 2014. Assessing the effects of anthropogenic aerosols on pacific storm track using a multiscale global climate model. *Proceedings of the National Academy of Sciences*, Vol.111, pp. 6894-6899.
- Wei J.M., 2013. A Monte Carlo method for coagulation of charged particles. *Journal of Aerosol Science*, Vol. 65, pp. 21-25.
- Wei J.M., Kruis F.E., 2013. A GPU-based parallelized Monte-Carlo method for particle coagulation using an acceptance-rejection strategy. *Chemical Engineering Science*, Vol.104, pp. 451-459.

References

- Wen J.Z., Thomson M.J., Park S.H., Rogak S.N., Lightstone M.F., 2005. Study of soot growth in a plug flow reactor using a moving sectional model. *Proceedings of the Combustion Institute*, Vol. 30, pp. 1477-84.
- Wen Z., Yun S., Thomson M.J., Lightstone M.F., 2003. Modeling soot formation in turbulent kerosene/air jet diffusion flames. *Combustion and Flame*, Vol. 135, pp. 323-340.
- Wu J.S., Lian Y.Y., 2003. Parallel three-dimensional direct simulation Monte Carlo method and its applications. *Computers & Fluids*, Vol. 32, pp. 1133-1160.
- Xu Z.W., Zhao, H.B., Zheng C.G., 2015. Accelerating population balance-Monte Carlo simulation for coagulation dynamics from the Markov jump model, stochastic algorithm and GPU parallel computing. *Journal of Computational Physics*, Vol. 281, pp. 844-863.
- Yin Z.Q., Liu H.J., 2014. Numerical simulation of nanoparticles diffusion and coagulation in a twin-jet via a TEMOM method. *International Journal of Numerical Methods for Heat & Fluid Flow*, Vol. 24, pp. 1312-1320.
- Yu M.Z., Chan T.L., 2015. A bimodal moment method model for submicron fractal-like agglomerates undergoing Brownian coagulation. *Journal of Aerosol Science*, Vol. 88, pp. 19-34.
- Yu M.Z., Lin J.Z., Chan T.L., 2008. A new moment method for solving the coagulation equation for particles in Brownian motion. *Aerosol Science and Technology*, Vol. 42, pp. 705-713.
- Yu M.Z., Lin J.Z., Chan T.L., 2009. Numerical simulation for nucleated vehicle exhaust particulate matters via the TEMOM/LES method. *International Journal of Modern Physics C*, Vol. 20, pp. 399-421.
- Zhang M.H., Chu K.W., Wei F., Yu A.B., 2008. A CFD-DEM study of the cluster behavior in riser and downer reactors. *Powder Technology*, Vol. 184, pp. 151-165.
- Zhang P., Gao C., Zhang N., Slepian M.J., Deng Y., Bluestein D., 2014. Multiscale particle-based modeling of flowing platelets in blood plasma using dissipative particle dynamics and coarse grained molecular dynamics. *Cellular and molecular bioengineering*, Vol. 7, pp. 552-574.
- Zhang W., You C., 2015. Numerical approach to predict particle breakage in dense flows by coupling multiphase particle-in-cell and Monte Carlo based methods. *Powder Technology*, Vol. 283, pp. 128-136.
- Zhang Y., Seigneur C., Seinfeld J.H., Jacobson M.Z., Binkowski, F.S., 1999. Simulation of aerosol dynamics: a comparative review of algorithms used in air quality models. *Aerosol Science and Technology*, Vol. 31, pp. 487-514.
- Zhang Z., Chen Q., 2007. Comparison of the Eulerian and Lagrangian methods for predicting particle transport in enclosed spaces. *Atmospheric Environment*, Vol. 41, pp. 5236-5248.

References

- Zhao B., Yang Z., Wang J., Johnston M.V., Wang H., 2003. Analysis of soot nanoparticles in a laminar premixed ethylene flame by scanning mobility particle sizer. *Aerosol Science & Technology*, Vol. 37, pp. 611-620.
- Zhao H.B., Zheng C.G., Xu M.H., 2005. Multi-Monte Carlo approach for general dynamic equation considering simultaneous particle coagulation and breakage. *Powder Technology*, Vol. 154, pp. 164-178.
- Zhao H.B., Kruis F.E., Zheng C.G., 2009. Reducing statistical noise and extending the size spectrum by applying weighted numerical particles in Monte Carlo simulation of coagulation. *Aerosol Science and Technology*, Vol. 43, pp. 781-793.
- Zhao H., Kruis F. E., Zheng C., 2010. A differentially weighted Monte Carlo method for two-component coagulation. *Journal of Computational Physics*, Vol. 229, pp. 6931-6945.
- Zhao H.B., Zheng C.G., 2012. A population balance-Monte Carlo method for particle coagulation in spatially inhomogeneous systems. *Computers & Fluids*, Vol. 71, pp. 196-207.
- Zhao H.B., Zheng C., 2013. A population balance-Monte Carlo method for particle coagulation in spatially inhomogeneous systems. *Computers & Fluids*, Vol. 71, pp. 196-207.
- Zhou K., Chan T.L., 2011. Simulation of homogeneous particle nucleation in a free turbulent jet. *Aerosol Science and Technology*, Vol. 45, pp. 973-987.
- Zhou K., Chan T.L., 2014. Analytical approximation schemes for mean nucleation rate in turbulent flows. *Aerosol Science and Technology*, Vol. 48, pp. 459-466.
- Zhou K., He Z., 2014. Monte Carlo simulation of aerosol evolution in a planar mixing layer. *International Journal of Numerical Methods for Heat & Fluid Flow*, Vol. 24, pp. 1769-1781.
- Zhou K., He Z., Xiao M., Zhang Z., 2014. Parallel Monte Carlo simulation of aerosol dynamics. *Advances in Mechanical Engineering*, AN 435936 pp. 1-11.
- Zhuang Y.Q., Chen X.M., Luo Z.H., Xiao J., 2014. CFD-DEM modeling of gas-solid flow and catalytic MTO reaction in a fluidized bed reactor. *Computers & Chemical Engineering*, Vol. 60, pp. 1-16.
- Zucca A., Marchisio D.L., Vanni M., Barresi, A.A., 2007. Validation of bivariate DQMOM for nanoparticle processes simulation. *AIChE Journal*, Vol. 53, pp. 918-931.
- Zucca A., Marchisio D.L., Barresi A.A., Fox R.O., 2006. Implementation of the population balance equation in CFD codes for modelling soot formation in turbulent flames. *Chemical Engineering Science*, Vol. 61, pp. 87-95.